OTTO-VON-GUERICKE-UNIVERSITÄT MAGDEBURG
Institute for Electronics, Signal Processing and Communication

Correction of Non-Periodic Motion in Computed Tomography

DISSERTATION

zur Erlangung des akademischen Grades
Doktor-Ingenieur (Dr.-Ing.)
von M.Sc. Colas Schretter
geb. am 21 Januar 1979 in Braine L'Alleud, Belgien
genehmigt durch
die Fakultät für Elektrotechnik und Informationstechnik
der Otto-von-Guericke Universität Magdeburg

Gutachter: Prof. Dr. rer. nat. Georg Rose
Prof. Dr. rer. nat. habil. Oliver Speck
Prof. Dr.-Ing. Til Aach

Promotionskolloquium am 28 April 2010

Correction of Non-Periodic Motion in Computed Tomography

Colas Schretter

Colophon

This book was typeset using the LyX editor. The generated LaTeXcode was compiled to produce a document in the Adobe PDF format. The bibliography has been generated using BibTeX. The electronic version of this document contains hyperlinks. A click on any reference jumps in the appropriate location in the document such as equations, footnotes, and literature references. For each entry in the bibliography, a list of page numbers is mentioned as well with links pointing back to citations.

Credits

The pictures (a), (b), and (d) in the first figure of the first chapter are courtesy of Royal Philips Electronics Inc. The picture (c) is courtesy of Elekta AB (publ). The other images have been generated with various algorithms written by the author in the C++ programming language. Results have been converted to grayscale images in the lossless PNG format with the ImageJ software. Plots and histograms have been generated using the Gnuplot graphing utility. Other figures have been drawn with the Omnigraffle software at the exception of figure 7.2 in chapter 7 that is courtesy of Fabian Pilatus (made with the Inkscape software).

First printed in Magdeburg, Germany, March 1st, 2010

Abstract

Medical imaging with computed tomography (CT) aims at reconstructing a volumetric image of the patient's anatomy from a sequence of planar X-ray projections. The quality of reconstructed images is often degraded by residual patient motion, especially when using slowly rotating C-arm robots or X-ray systems integrated with linear accelerators for radiotherapy. The data acquisition might take from several seconds up to one minute on those equipments. In particular, if the patient does not manage to hold his or her movements during measurements, image resolution can be impaired by strong motion blur artifacts.

This work was dedicated to the development of original techniques aiming at improving the quality of CT images when X-ray projections contain non-periodic patient motion. Since the developed methods do not assume any periodicity of the motion model, they can correct artifacts due to unstructured patient motion, such as breath-hold failure, abdominal contractions, and nervous movements. The proposed solutions tackle for the first time the problem of motion correction in CT by using solely the acquired data.

A first approach is to iteratively correct the reconstructed image by first decomposing the perceived motion in projection space into positive and negative parts, then reconstructing the motion artifacts in image space, and finally, subtracting the artifacts from an initial image of the anatomy. The initial image is reconstructed from the acquired data without motion compensation but is nevertheless considered as a reference for estimating the reconstruction artifacts.

An alternative approach consists of an iterative workflow to progressively estimate a dynamic displacement vector field representing the position of image elements over time. The motion information is then used within a motion-compensated variant of the analytical reconstruction algorithm to improve the image quality locally. An elastic image registration step computes the displacement in projection space, minimizing the difference between measured projections and reference projections sampled from the image reconstructed in previous iterations. In addition, a motion segmentation procedure detects in image space the regions which are subject to motion during acquisition.

Promising experimental results are summarized in qualitative figures and quantitative analyses. Experiments are based on numerically simulated projections from a mathematical phantom and from a sequence of clinical images obtained from a

respiratory-gated acquisition on a fast helical CT scanner. Several elastic image registration methods are also evaluated for motion estimation purpose. In supplement, a study comparing various image interpolation and approximation techniques and their impact on reconstructed image fidelity is presented.

Keywords: computed tomography, iterative methods, motion segmentation, motion estimation, motion compensation.

Kurzfassung

Bei der medizinischen Bildgebung mittels Computertomographie (CT) wird aus einer Serie planarer Röntgenprojektionen ein dreidimensionales Bild der Anatomie eines Patienten rekonstruiert. Die Qualität des rekonstruierten Bildes wird bei Einsatz langsam rotierender Systeme, wie insbesondere Röntgen-C-Bögen oder an strahlentherapeutische Linearbeschleuniger gekoppelte Röntgensysteme, aufgrund der langen Aufnahmedauer von einigen Sekunden bis Minuten oft durch Bewegungen des Patienten beeinträchtigt. Dabei führt insbesondere die Atmung sowie willkürliche und auch unwillkürliche Bewegungen des Patienten zu starken Bildartefakten.

Diese Arbeit beschäftigt sich mit der Entwicklung zweier neuartiger Methoden zur Korrektur derartiger Bewegungsartefakte. Dabei werden keine Forderungen an die Periodizität des Bewegungsmodells gestellt, so dass auch Artefakte, welche durch unregelmäßige Patientenbewegungen verursacht werden, wie zum Beispiel unwillkürliche Bewegungen beim Anhalten der Atmung, abdominelle Kontraktionen oder unkontrollierte Bewegungen korrigiert werden können. Die entwickelten Methoden lösen erstmalig das Problem der Korrektur von Bewegungsartefakten einzig unter Zuhilfenahme der gemessenen Daten.

Bei dem ersten iterativen Verfahren wird das rekonstruierte Bild dadurch korrigiert, dass zunächst die Bewegungen aus den Projektionsdaten extrahiert und anschließend im Bildraum rekonstruiert werden, um schließlich von dem ursprünglichen 3D-Bild abgezogen zu werden. Dabei wird das initiale 3D-Referenzbild aus den aufgenommenen Projektionsdaten rekonstruiert und enthält daher noch Bewegungsunschärfeartefakte, es wird dennoch als Referenz zur Schätzung der Rekonstruktionsartefakte betrachtet.

Die zweite Methode basiert auf einer iterativen Bestimmung des dynamischen Verschiebungsvektorfeldes, welches die zeitlich variierenden Positionen von Bildelementen beschreibt. In der folgenden Rekonstruktion wird die Rückprojektion nicht entlang gerader, sondern durch die Verschiebungsvektoren definierter gekrümmter Strahlen durchgeführt. Ein elastischer Registrierungalgorithmus berechnet die Verschiebung im Projektionsraum durch Minimierung der Differenz aus gemessenen Projektionen und Referenzprojektionen, welche aus dem in einer vorhergegangenen Iteration rekonstruierten Bild berechnet werden. Zudem ermittelt ein Bewegungssegmentierungsverfahren im Bildraum die Teile der Anatomie, welche sich tatsächlich während der Aufnahme bewegt haben.

Die entwickelten Methoden werden innerhalb zahlreicher Experimente sowohl auf simulierten Daten eines mathematischen Phantoms als auch auf klinischen Daten, welche auf einer schnellen atmungsgesteuerten Aufnahme mittels eines Spiral-CT basieren, analysiert und evaluiert. Mehrere elastische Bildregistrierungsmethoden werden auch zwecks Bewegungsschätzung bewertet. Durch den Einsatz verschiedener Methoden zur Bewegungsschätzung sowie unterschiedlicher Bildinterpolation und Bildapproximation während der Rekonstruktion konnten die entwickelten Verfahren weiter verbessert werden.

Schlüsselworte: Computertomographie, iterative Methoden, Bewegungssegmentierung, Bewegungsschätzung, Bewegungskompensierung.

Preface

The present dissertation is summarizing the new knowledge that I gathered during the past three years working in the field of image reconstruction with computed tomography (CT). This work has been kindly sponsored by the Marie Curie early stage training (EST) programme of the European Commission. The European guidelines are encouraging mobility of young researchers and the Comission provides financial support for making this a reality.

I received a position as a doctoral researcher beginning on the first February 2007 and decided to seize the opportunity. I moved from Brussels, Belgium to the little and charming town of Aachen in Germany. This was the first time in my life I lived abroad and this experience brought much more discoveries than the results presented in this volume.

In Aachen, I joined the labs of Philips Research, a private research organization holding a network of research labs around the world, especially in The Netherlands, Germany, France, Israel, and the USA. I worked there as a regular employee and my task was to explore new techniques for the correction of motion blur artifacts in the field of tomographic image reconstruction. The problem was very open. The research was exploratory, hence, very exiting.

In parallel, the results developed during three years had to fulfill the requirements for obtaining a doctoral degree from the Otto-von-Guericke University of Magdeburg, Germany. The university was partner of the Marie Curie programme. I strived to give the best of myself to reach the double-target of producing practically relevant results for Philips while meeting academic requirements.

Balancing the objectives from the industrial world and the scientific community was not easy and this certainly required much more dedication and time than working as the other employees. As a corollary, I spent very few days for vacation because of urgent matters in the "todo list." The pressure was sometimes too high and stressful for me but it also contributed to meet expectations.

In summer 2008, I had the chance to be selected for the prestigious *IEEE EMBS International Summer School on Biomedical Imaging* organized in the Berder Island, Bretagne, France. I travelled often to international conferences to present the current state of my work and I always learned a lot from interactions with experienced scientists and students.

The topic of this thesis is the correction of motion artifacts that might arise in volumetric images acquired by X-ray transmission scanners. The underlying problems to solve are identified as motion estimation, motion detection, and motion compensation within existing analytical image reconstruction algorithms.

Image reconstruction with analytical methods was a firm requirement for backward compatibility with the existing imaging chains. The direction of my research aimed at demonstrating original techniques that would be readily applicable on existing scanners. Often, experiments have taken more importance over theoretical justifications and it can be said that this work is fairly practical, even pragmatic.

Publications

Most of the content of the present thesis has been presented to international conferences and published in peer-reviewed scientific journals. The list of my personal publications directly related to this work follows.

Journal Papers

1. Colas Schretter, Georg Rose and Matthias Bertram, "Image-Based Iterative Compensation of Motion Artifacts in Computed Tomography," *Medical Physics*, Volume 36, Number 11, Pages 5323–5330, 2009.

2. Colas Schretter, "A Fast Tube of Response Ray-Tracer," *Medical Physics*, Volume 33, Number 12, Pages 4744–4748, 2006.

Conference Lectures

1. Colas Schretter, Fabian Pilatus, Georg Rose, Til Aach and Matthias Bertram, "Optical Flow Motion Estimation for Approximate Motion Compensation in Cone-Beam CT," 10$^{\text{th}}$ *International Meeting on Fully Three-Dimensional Image Reconstruction in Radiology and Nuclear Medicine (Fully3D)*, Beijing, China, September 6–12, Pages 327–330, 2009.

2. Colas Schretter, Christoph Neukirchen, Georg Rose and Matthias Bertram, "Optimal Pre-Filtering for Linear Interpolation in Computed Tomography," 2$^{\text{nd}}$ *Workshop on High Performance Image Reconstruction (HPIR)*, Beijing, China, September 6, Pages 29–32, 2009.

3. Colas Schretter, Christoph Neukirchen, Georg Rose and Matthias Bertram, "Image-Based Iterative Compensation of Motion Artifacts in Computed Tomography," *SPIE Medical Imaging*, Lake Buena Vista, USA, 7–12 February, Volume 7258, Pages 72581W–8, 2009.

4. Colas Schretter, Christoph Neukirchen, Matthias Bertram and Georg Rose, "Correction of Some Time-Dependent Deformations in Parallel-Beam Computed Tomography," 5$^{\text{th}}$ *IEEE International Symposium on Biomedical Imaging (ISBI)*, Paris, France, May 14–17, Pages 764–767, 2008.

Poster Presentations

1. Colas Schretter, Christoph Neukirchen, Georg Rose and Matthias Bertram, "Local Correction of Non-Periodic Motion in Computed Tomography," *SPIE Medical Imaging*, Lake Buena Vista, USA, February 7–12, Volume 7258, Pages 72582M–12, 2009.

2. Alfonso A. Isola, Colas Schretter, Michael Grass, Matthias Bertram, Georg Rose and Wiro J. Niessen, "Compensation of Periodic Cardiac Motion and Non-Periodic Abdominal Motion in Cone-Beam CT," *Marie Curie Monitoring Mission*, Alexander von Humboldt Foundation, Bonn, Germany, January 29–30, 2009.

3. Colas Schretter, "Improving Image Quality in Computed Tomography by Motion Estimation and Compensation," 8^{th} *IEEE EMBS International Summer School on Biomedical Imaging*, Berder, France, June 20–28, 2008.

Patent Applications

1. Colas Schretter, Matthias Bertram and Christoph Neukirchen, "Method and Apparatus For Large Field of View Imaging and Detection and Compensation of Motion Artifacts," US 30961/04024, January, 2009.

2. Peter Forthmann, Thomas Köhler, Udo Van Stevendaal, Matthias Bertram, Stephen Hohmann and Colas Schretter, "Method and Apparatus to Improve CT Image Acquisition Using Displaced Geometry," US 30961/04021, September, 2008.

Acknowledgments

After three years of learning from numerous readings, developing ideas from intense reflections and experimenting new techniques, the redaction of the present thesis is not only a personal achievement. For this project, I moved to a foreign country, I met new people and made new friends. In return, I benefited from multiple influences and I would like to acknowledge sincerely all the persons that steered my work in their own way.

First of all I would like to thank my daily supervisors Matthias Bertram and Georg Rose. Matthias is the manager of a small group known as the volumetric imaging project (VIP) cluster within Philips Research, in Aachen. I appreciated the way I was integrated naturally among the experienced scientists at Philips. Matthias was always welcoming ideas. He gave the freedom which was necessary for developing personal solutions and was easily convinced, with enthusiasm.

I received wonderful help from Georg Rose, my academic supervisor at the Otto-von-Guericke University, Magdeburg. Over six hours of train are needed to reach Magdeburg from Aachen. Georg was geographically distant, but I experienced his natural friendship and felt him closer with time. I benefited so much from his honest advices and I can not express better my gratitude.

Philips Research Aachen is one of the biggest private research labs in Germany, counting about three hundreds scientists. I was introduced there with the recommendations of Ralph Brinks, Carsten Meyer, and others. I'm sincerely thankful for your great support and your thorough revisions of my journal articles. At lunch time, I always enjoyed involved discussions with Christoph Neukirchen, Jens Wiegert, Jerôme Durant, Marco Giordano, Steffen Wiesner, and our visiting students. The hints and support of Brian O'Neill and Helko Lehmann were essential for launching all the image reconstruction experiments on the Linux cluster of computers and for volume rendering vizualisation.

During the last year, I supervised the Master's thesis of Fabian Pilatus, student in engineering at The RWTH Aachen University. This was a wonderful experience and Fabian contributed to the present work as well by making experiments with various elastic registration algorithms. He produced the images from the result section in chapter 7. A conference paper was also created together with his professor Til Aach. I especially appreciated the experience, ideas, and careful reviews from Prof. Aach. He also accepted to assess the present thesis. For the future, I hope we will have more occasions to collaborate further!

I always learned much from discussions with colleagues from Philips Research from Hamburg. The initial help from Dirk Schäfer was essential for pointing out some key references. To my numerous questions, I appreciated the kind answers from Thomas Köhler. Thomas also shared his respiratory-gated image sequences. This dataset was a key for demonstrating convincing results from realistic clinical images. At conferences, I met Hermann Schomberg and learned so much from our discussions about theoretical and technical aspects of analytic image reconstruction.

Discussions with external collaborators contributed a lot for acquiring new knowledge. In particular, I would like to thank Henrik Turbell for sharing his implementation of the FDK algorithm. I thank Laurent Condat, Marco Dalai and Thierry Blu for their feedback about image interpolation and approximation. I appreciated very much the help of Se Young Chun and Jeffrey Fessler from The University of Michigan for sharing their elastic image registration implementation and for our collaboration on the respiratory motion estimation problem. David Barber and Rod Hose from The University of Sheffield have provided the ShIRT image registration toolkit and a great assistance for the experiments.

After moving to Aachen, my daily life was mostly devoted to work. It's true, but not sad! I met natural friends from the very first working year at Philips. Claudia Stahl, now in London. Jerôme Durant, now in Paris. Olivier Ecabert, still in Aachen. Almost every Tuesday evening, I visited INCAS, the association for foreign students in Aachen. There I met Sylvia Devaux, Irina Pescarasu, Olivier Laurent, Lea Sheer, and so many enthusiastic and wonderful people from all over the world. Sylvia ought to be credited for translating in German the abstract of this thesis.

Even if I'm not so often present in Belgium, I do not forget my friends that I met at The University of Brussels (ULB): Eythan Levy, Utku Salihoglu, Michel Lequim, Matthias Jacot, Laurent Gatto, Patrick Meyer. I'm also grateful to Prof. Michel Defrise. He introduced to me the problem of image reconstruction in tomography and I learned so much from our weekly meetings during my Master of advanced studies (DEA) at the ULB. The integrality of my DEA thesis has been published into two papers in peer-reviewed journals and two others papers that were presented

at international conferences. This initial work was important because it brought to me more confidence and triggered positive changes. I realized that independent thinking is a requirement for innovative research investigations.

Last but not least, I would like to thank my parents for always supporting my choices. I'm grateful to my girlfriend Maria Kashlyaeva for her support, kindness and love. This is in Germany that I discovered the most of Russia: in Cologne where her parents Valery and Svetlana are living. I thank you sincerely for adopting me, for all the weekends we spend together, the good food, the summer activities, and our memorable travels to Moscow.

For this research, I was granted with financial support from the Marie Curie early stage training (EST) fellowships from the 6^{th} Framework Programme of the European Commission under contract MEST-CT-2005-020424.

Colas Schretter
January 2010, Aachen, Germany

Contents

List of Acronyms

ART	Algebraic Reconstruction Technique
CB	Cone-Beam
CG	Conjugate Gradients
CT	Computer Tomography
EM	Expectation-Maximization
ET	Emission Tomography
FBP	Filtered BackProjection
FDK	Fedlkamp-Davis-Kress
FFD	Free-Form Deformation
FFT	Fast Fourier Transform
FIR	Finite Impulse Response
FOV	Field Of View
FOM	Field Of Measurements
GPU	Graphics Processing Unit
HU	Hounsfield Unit
IIR	Infinite Impulse Response
LINAC	Linear Accelerator
LUT	Look-Up Table
MAE	Mean Absolute Error
MLEM	Maximum Likelihood Expectation-Maximization
MSE	Mean Squared Error
OSEM	Ordered Subsets Expectation-Maximization
Pixel	Picture Element
PSF	Point Spread Function
RAMLA	Row-Action Maximum Likelihood Algorithm
ROI	Region Of Interest
SAD	Sum of Absolute Differences
SART	Simultaneous Algebraic Reconstruction Technique
ShIRT	Sheffield Image Registration Toolkit
SIRT	Simultaneous Iterative Reconstruction Technique
SNR	Signal to Noise Ratio
SPECT	Single Photon Emission Tomography
SSD	Sum of Squared Differences
TPS	Thin Plate Spline
Voxel	Volume Element

1 Introduction

X-ray transmission has been an ubiquitous technique for visualizing the human's anatomy since its discovery attributed to Wilhelm Conrad Röntgen in 1895[1]. By using *computed tomography* (CT) techniques, the inner structures of convex objects can be revealed from external X-ray measurements. This work emphasizes on the applications of tomographic imaging during surgical interventions and radiotherapy.

The ever increasing precision of digital detectors generated a current need for the correction of general patient motion that often corrupts reconstructed images with *motion blur* artifacts. Today, motion correction in CT is a crucial problem and recent releases in literature indicate that this research topic becomes also increasingly popular. Surprisingly, the correction of non-periodic residual motion for *static volumetric imaging* is a problem that has not been tackled yet.

The theory behind image formation in CT assumes that the reconstructed object remains static during data acquisition. Improving image quality of low-contrast volumetric imaging when data contains non-periodic motion has been the major problem tackled in this work. This introductory chapter overviews various applications of CT for medical imaging. Moreover, an experiment illustrates the general problem of image degradation by unwanted breathing motion.

1.1 Volumetric Medical Imaging

Closed gantry computed tomography (CT) systems are often the modality of choice for diagnostic volumetric imaging (Kalender, 2006). However, such systems are only rarely used during *minimally invasive* interventional treatments due to the ring structure which restricts the access to the patient during surgery. C-arm devices on the other hand have an open structure which allows the examiner to fully access the patient, making them the modality of choice for catheter guidance (Jaffray and Siewerdsen, 2000; Rose *et al.*, 2003).

[1] History has its peculiarities and it is seldom in science that inventions are attributed to inventors. First discovered by Nikola Tesla in April 1887, the X-rays had a name before: the *Bremsstrahlung* (braking radiation).

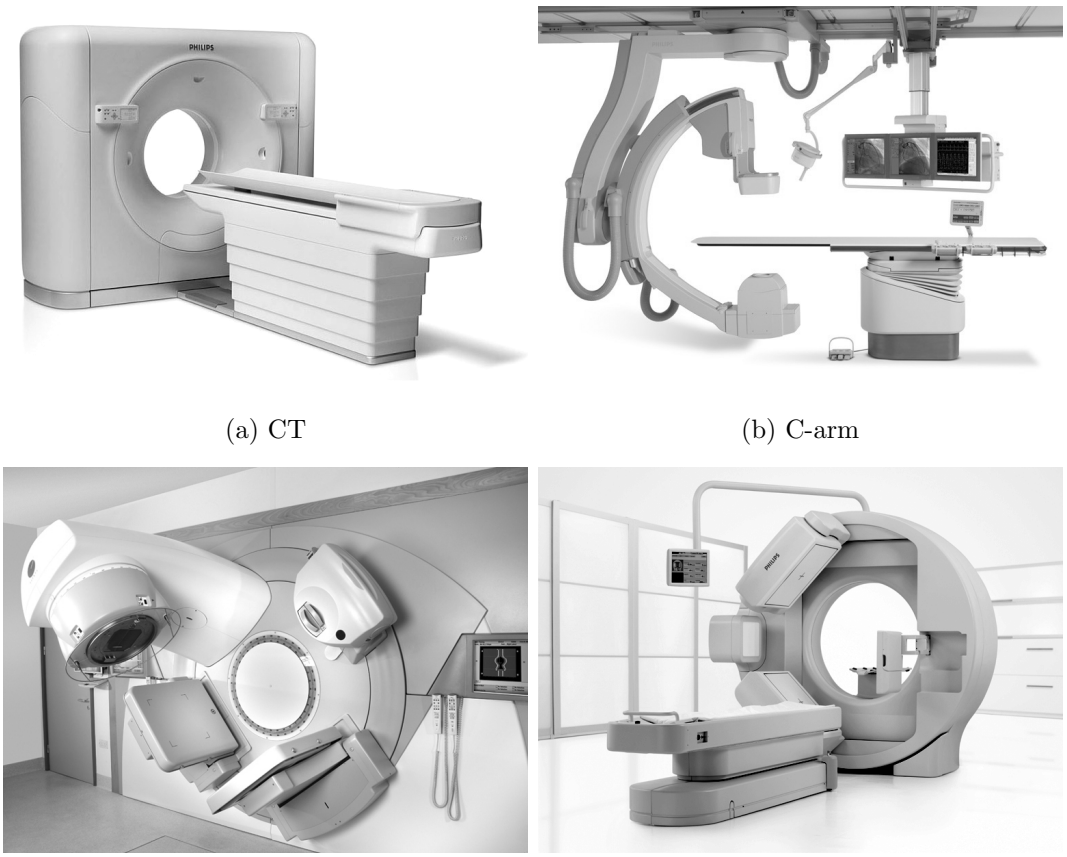

(a) CT (b) C-arm

(c) LINAC (d) SPECT

Figure 1.1: Comparison of various CT scanners using the cone-beam geometry for volumetric anatomical imaging. The classical slipping ring CT (a) is a very fast closed-gantry scanner used for diagnostic. The geometry of the X-ray focus source and the planar detector is well visible in the open-gantry C-arm system (b). C-arm robots are mainly used for conventional fluoroscopy during interventions but CT acquisitions are possible with a slow rotation speed. The LINAC systems (c) are used for radiotherapy and combines a focused high-energy beam for treatment with a cone-beam CT setup used for patient positioning and outcome control. Cone-beam CT systems are very versatile and are also combined with SPECT scanners (d).

Nowadays CT devices are also embedded on linear accelerators (LINAC) for radiotherapy (Cho *et al.*, 1995; Jaffray *et al.*, 2002; Dietrich *et al.*, 2006) or on single photon emission tomography (SPECT) scanners (Buck *et al.*, 2008). For example, figure 1.1 displays photographs of a fast slipping ring CT system used for diagnostic imaging, a C-arm system used for interventional treatments with catheters, a radiotherapy LINAC machine and a SPECT scanner combined with a cone-beam setup. A well visible external X-ray tube and a *flat panel detector* are mounted on the rotating gantry of those hybrid devices.

Only an X-ray point source and a detector are needed for CT imaging with divergent ray geometries, also known as cone-beam geometries. An *image reconstruction* method is then used to generate two-dimensional transversal slices of a three-dimensional volumetric image from a corpus of X-ray projections (Grangeat,

1991; Defrise and Clack, 1994; Katsevich, 2003). Projection data is taken while the system is rotating around the object usually using either a circular or helical trajectory. It is required that the object stays static during data acquisition for an exact reconstruction from consistent projections.

In particular, C-arm systems were primarily developed for acquiring planar (2D) views for real-time fluoroscopy. By programming an appropriate trajectory of the robotic arm, it has been made possible to use C-arms for the acquisition of volumetric (3D) images as well. With volumetric imaging capabilities, it is not necessary anymore to move the patient to a dedicated CT room when requiring tomographic images during a treatment procedure. A drawback of CT on such slow cone-beam systems is the evidence of *image artifacts* that are generated implicitly by the moving organs.

Hounsfield Units (HU)

In CT imaging, the values of the attenuation coefficients are conventionally expressed in *Hounsfield units* (HU), which represent the attenuation of an object relative to the attenuation of water. The unit is named after the designer of the very first CT scanner, Sir Godfrey Newbold Hounsfield (1973). The conversion of the original linear attenuation coefficient measurement values f to an image in Hounsfield units μ is given by

$$\mu(x, y, z) = \frac{f(x, y, z) - \mu(H_2O)}{\mu(H_2O)} \cdot 1000, \tag{1.1}$$

where the attenuation of water (H_2O) is by definition equals to 0 HU.

The typical scale reaches from -1,000 HU for air to 3,000 HU for materials with very high attenuation such as metal. The density of bone structures is patient-specific and should range from around 400 HU to 800 HU. Due to the restricted dynamic range of displays and humans's perception only a limited window of attenuation values is displayed to enhance the contrast for a certain type of material. The mapping from the high dynamic range of CT numbers to grayscales is called windowing.

When presenting results from experiments, all slices are extracted from volumetric images represented by a Cartesian grid of 256×256×198 isotropic voxels of size equal to 1.36 mm. Black is set to the attenuation of air and gray corresponds to the attenuation of water. Highly attenuating materials such as bones yield to brighter voxels.

1.2 Motion Blur Artifacts

Motion blur image artifacts are an ubiquitous and general problem in medical applications of CT (Chen *et al.*, 2004). X-ray transmission and detection is very fast and each acquired projection is a sharp snapshot of the anatomy. However, the whole acquired dataset might be inconsistent if organ motion occurred during the acquisition of all the projections that are necessary for image reconstruction. Data inconsistencies introduce artifacts such as streaks, distortions and general blurring in the reconstructed image.

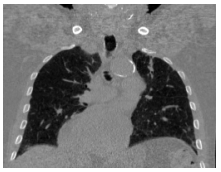

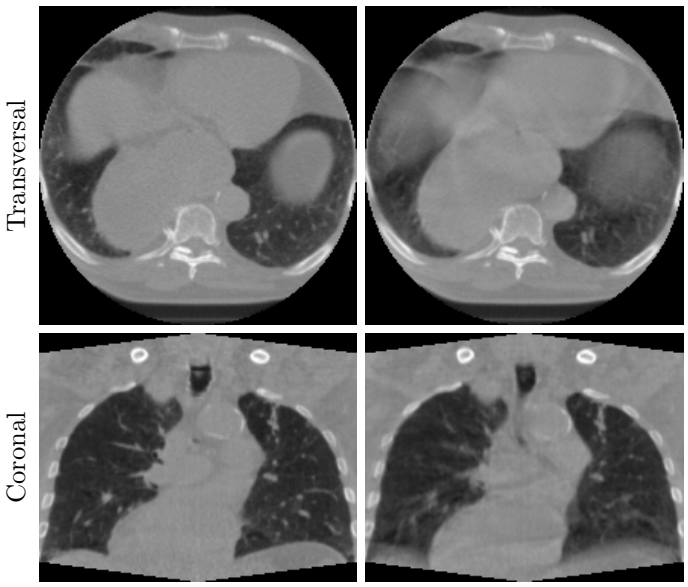

(a) Without motion (b) With breathing

Figure 1.2: Illustration of typical motion blur image artifacts that result when the patient is breathing during an acquisition on a C-arm cone-beam CT device. The images are selected slices from volumetric images reconstructed from simulated projections and allow the side-by-side comparison of both reconstructions from consistent projections (a) and inconsistent projections (b).

Since C-arm systems were not originally intended to be used for the purpose of tomographic imaging, there is a major issue regarding the amount of time required for an acquisition. A C-arm requires about five to twenty seconds for a single rotation and some patients might not be able to hold still without breathing during the entire acquisition time. This problem holds especially for older persons, patients under sedatives, and young children.

Motion blur artifacts are even more problematic when using very slowly rotating gantry CT scanners such as LINAC systems for radiotherapy (Fung *et al.*, 2007). On these heavy machines, a complete acquisition lasts for about one minute and the patient will not able to hold his breath. Furthermore, other uncontrolled movements such as heartbeat, nervous shaking or intestinal contractions can corrupt the data. Data inconsistencies leads to severe motion blur artifacts in the reconstructed images.

Experiment

In order to grasp better the effect of patient motion in cone-beam CT, an experiment has been conducted to analyse the image artifacts induced by simulated respiratory motion during a simulated data acquisition on a C-arm system. The geometry of an existing C-arm has been considered for sampling X-ray projections from a clinical dynamic CT image of the respiration. The constrains of the perspective geometry and the finite detector size induces truncations of the reconstructed image because the region of possible reconstruction is smaller than the patient's body.

For the experiment, projections in C-arm geometry were simulated using a phantom consisting of a clinical image sequence. A slow acquisition of 12 seconds was

modeled so that at least 3 breathing cycles are included in this acquisition. To simulate X-ray projections, a number of line integrals were taken from a specific frame that was chosen according to the current breathing state. It results, that every 0.09 seconds, a new frame is taken. For the complete data acquisition, projections from 360 different angles has been generated which correspond to one projection every 0.03 seconds.

Results

Results of two reconstructed images are compared in figure 1.2. The first image is computed from consistent data sampled from only one motion state. The second image is reconstructed from inconsistent data and demonstrates severe artifacts. The stomach and the liver are well visible in the transversal slice of the first image; however, they appear as semitransparent organs in the motion-corrupted image. The ghosting effect is the result of moving voxels that are estimated as a mixture of water and air. In coronal slice, the border of the respiratory diaphragm is strongly blurred as well.

To better visualize the dynamics of the respiratory movement, a flipbook animation has been inserted in the right margin of odd-numbered pages for browsing among a selected slice crossing the chest. By flipping the pages very rapidly, starting from page 95, an animation of the full breathing cycle will appear. The animation shows some selected frames from a dynamic volumetric image that will be systematically used for experiments and evaluations of the various motion correction methods presented in this work. The frames consist of central coronal slices extracted from the 40 volumetric images of the dynamic sequence.

1.3 Previous Work

Motion correction is a ubiquitous problem for almost every tomographic imaging modality. Indeed, the data acquisition process always take times and therefore the problem of reconstructing a unique image become often ill-posed. This section reviews alternative motion avoidance or motion compensation methods that have been developed previously in medical tomography.

Emission Tomography

One of the first tomographic modality for which the crucial importance of motion correction was raised is emission tomography (ET). Emission tomography scanners such as positron emission tomographs (PET) or single photon emission tomographs (SPECT) can produce low-resolution functional images of the metabolic uptake or the cardiac activity.

Prior to the examination, a radioactive tracer is injected intravenously and diffuses progressively into the organism. In PET, the radiolabelled tracer emits positrons during its radioactive decay. After a short random walk, the positron annihilates with an electron and two collinear high-energy photons are generated.

The PET scanner records the detection of coincident photon pairs that are emitted in random direction from inside the body. With the list mode of all detected

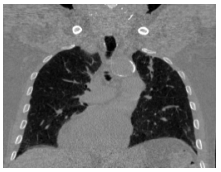

Frame 39/40

events, the spatial distribution of the radioactive tracer can be reconstructed to produce three-dimensional images. The detection of emission events by SPECT systems is based on the detection of photons that are directly emitted from the radiological decay of the injected gamma-emitting radioisotope.

A typical acquisition lasts for about 30 to 60 minutes in order to measure a sufficient volume of data for image reconstruction. The scanning process is slow by nature since the emission of high-energy photons is driven by the nuclear decay process. In SPECT, early work by Fulton *et al.* (1994) tracks the rigid movement of the head for brain studies for prospective compensation.

One representative alternative solution is currently developed in the group of Gilland *et al.* (2008). Gilland is using an image based optical flow method to estimate cardiac contractions for SPECT. In positron emission tomography (PET), either the electrocardiogram (ECG) or the respiratory signal is extracted from the data to produce motion-compensated 4D images (Livieratos *et al.*, 2005; Qiao *et al.*, 2007; Blume *et al.*, 2008).

Magnetic Resonance Imaging

Magnetic resonance imaging (MRI) is another kind of tomographic modality that was developed for imaging the soft-tissue structures with an exceptional image resolution as demonstrated by Weiskopf *et al.* (2007), for example. MR scanners are sensitive to water molecules and the recovery of contrast between different soft tissues densities is much better when compared to X-ray imaging, for example.

However, parts of the anatomy that contains little amount of liquids, such as bone structures, appear to be invisible on the image. Magnetic resonance is a field of continuous and exiting expansion and new applications such as real-time tracking of particles or recording of the brain activity can be acquired today.

A major drawback of imaging modalities based on the physical principle of magnetic resonance is directly linked to the high cost of the scanners multiplied by the relatively long acquisition time. Because MR can not capture the metabolic activity, the combination of MR and PET imaging modalities is natural. This project is one of the next challenges in medical engineering.

For brain imaging, motion tracking using external cameras and computer vision techniques has been applied in MRI as well (Dold *et al.*, 2006). This solution demonstrated very high accuracy and is relatively straightforward to implement. Unfortunately, difficulties arise for the calibration of external cameras and the additional cost of such an optical tracking system is affecting the adoption of motion correction based on explicit external measurements.

For functional acquisitions in real-time, only a slice can be measured with current MR scanners. However motion tracking systems have demonstrated superior results (Speck *et al.*, 2006) when compared to image-based correction of motion artifacts such as the technique developed in the work of Manduca *et al.* (2004).

Dynamic Transmission Tomography

In medical applications of X-ray transmission tomography (CT), general patient motion has not been considered as an important problem until relatively recently. The specific case of cardiac imaging has been a predominant application of diagnostic

CT. In cardiac imaging, either a static or a dynamic image of the myocardium is reconstructed.

Early approaches to avoid data inconsistencies that are resulting from organ's motion have been to use a fast rotation speed of the gantry (Ritchie *et al.*, 1992) or to adapt the rotation speed (Willis and Bresler, 1995a,b) for each patient, for example, according to the rate of the ECG signal. However, the acquisition time on radiotherapy and interventional C-arm systems is slower than that on diagnostic closed-gantry CT scanners and the inconsistency of the acquired data is an unavoidable problem.

Free breathing acquisition protocols are often used with slow gantry rotation. While each projection is a sharp snapshot of the body at a certain motion state, the back-and-forth movement of the respiratory diaphragm is contained in the sequence of projections. For breath-hold acquisition protocols, the unstructured patient motion can be breath-hold failures, intestinal contractions, or nervous movements. For cardiac or respiratory gated dynamic imaging, each reconstructed frame might exhibit residual motion artifacts too, since a temporal window of a certain fixed width is associated with each gate.

Predictive respiratory gating schemes have been suggested to acquire only projections that correspond to a given motion state (Ritchie *et al.*, 1994; Vedam *et al.*, 2003), while retrospective gating allows the reconstruction of an image for each motion state of the breathing cycle (Sonke *et al.*, 2005). As a drawback, methods based on gating make the strong assumption that the patient motion is periodic (Lauritsch *et al.*, 2006; Hansis *et al.*, 2008b,a). Recent publications demonstrate that the periodicity hypothesis is valid only in few studies and alternatives are proposed for dynamic angiographic imaging (Rohkohl *et al.*, 2009a,b).

Static Transmission Tomography

If motion can not be avoided, some efforts were spent to detect where local motion occurs in image space. Motion detection from complementary rays has been investigated by Lin (1994), Linney and Gregson (2001), and Bruder *et al.* (2003). However, those techniques require datasets containing redundant measurements. Fourier space motion extractions (Chiu and Yau, 1994; Srinivas and Costa, 1994) are techniques aiming at removing the motion signal from projection data but results have not been very convincing in comparison to more modern methods exploiting data consistency conditions (Chen and Leng, 2005).

Solutions based on pre-correction of input projection data exist to handle non-periodic motion in CT. The correction is applied prior to reconstruction by resampling the data after estimating the motion in projection space (Lu and Mackie, 2002) or by modifying the values of line integrals to ensure data consistency conditions (Leng *et al.*, 2007, 2008). Those methods allow using standard image reconstruction algorithms; however, they are dedicated to capture only smooth motion or a limited class of deformations such as global translations (Yu *et al.*, 2006) or rigid body motion (Yu and Wang, 2007). Furthermore, the resampling step introduces some additional blurring and aliasing artifacts in the projection data.

A wealth of publications concerns the development of motion-compensated reconstruction algorithms. Exact motion compensation within analytical reconstruction methods (Kak and Slaney, 1988) of increasing complexity (Pack and Noo, 2004;

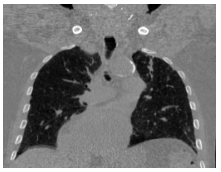

Roux *et al.*, 2004; Desbat *et al.*, 2007b; Taguchi and Kudo, 2008a; Katsevich, 2008) have been compared to modified algebraic reconstruction methods (Desbat *et al.*, 2007a; Rit *et al.*, 2009). It should be noticed that motion compensation is solving only half of the problem.

Unfortunately, all of those motion-compensated algorithms assume that the movement is known *a priori*. A remaining challenge is to estimate the motion from the available line integral data. Some recent applications of the compressed sensing theory (Donoho, 2006) aim at avoiding explicit motion estimation by reconstructing image frames using only few projections (Chen *et al.*, 2008).

A prior image from a diagnostic CT scan is often assumed to be available in order to reconstruct a motion-compensated image using further input data in addition to the acquired projections. For instance, the supplemental data can be a gated 4D dynamic image (Li *et al.*, 2006a,b) or a 3D static image (Zeng *et al.*, 2007; Brandt and Kolehmainen, 2007) from which the relative motion can be estimated by image registration (Maintz and Viergever, 1998; Hill *et al.*, 2001).

Those techniques can be applied to reconstruct a static volumetric image, even if projections are not gated according to a motion signal. However, a motion correction method that would estimate the patient motion from solely the acquired data is preferable for standalone applications.

1.4 Outline

The present work aims at improving image quality of static soft-tissue volumetric imaging on slow CT systems. A major technical restriction for the development of solutions was that the image should ultimately be reconstructed using analytical image reconstruction methods. While this limitative requirement is motivated by traditions and backward compatibility, this document shows new and encouraging image reconstruction results. The remainder of the thesis is organized as follows.

Chapter 2

In the next chapter, the inverse problem of image reconstruction from line integrals is defined and analytical, algebraic and statistical solutions are explained. A derivation of closed form analytical expressions for the reconstruction of images from line integrals will be given. In addition, alternative iterative approaches are discussed as well. Analytical algorithms are of special interest since their performances is typically faster than other approaches and their results are representative of the current gold standard in the field of CT reconstruction.

Chapter 3

In chapter 3, the impact of the traditional bilinear interpolation model on image quality of CT reconstruction is experimented. This additional work proposes to improve sharpness with simple prefiltering technique based on modern approximation theory. A naive implementation provides images that might be corrupted by aliasing, ringing, or blurring artifacts. This study is not directly related to motion but raises the importance of interpolation models in CT.

Chapter 4

Chapter 4 presents an iterative solution for removing motion blur artifacts from volumetric CT images. The technique is based on a combination of tomographic reconstruction and some standard image processing techniques. Starting from a standard reconstruction that is possibly corrupted by blurring artifacts, this image is progressively sharpened with time. Iteratively, the image quality is improved by estimating image artifacts and removing them from the corrupted initial image.

Chapter 5

Chapter 5 presents an alternative technique where the motion information is explicitly extracted from acquired data and used in an exact motion-compensated reconstruction algorithm that was already available. The experiments are conducted in 2D only, using a mathematical phantom object.

Chapter 6

Encouraged by the results from chapter 5, the technique has been extended to the 3D parallel-beam geometry in chapter 6. Results of first experiments using motion sampled from a real patient has been assessed on the clinical respiratory phantom that is first introducted in chapter 4. Moreover, the image regions subject to motion are detected and the new concept of local motion compensation is presented.

Chapter 7

In chapter 7, the local motion correction technique has been applied to the cone-beam geometry of an existing simulated C-arm system. The finite size of the digital detector induces truncation of the data in both the axial and transversal directions. Therefore, the method has been modified to accommodate this important additional constraint. As a solution, a scout reconstruction is created using an iterative reconstruction technique for a more accurate motion detection and motion estimation.

Chapter 8

The success of any motion compensated image reconstruction depends ultimately on the accuracy of the estimated motion information. Chapter 8 focuses on this sub-problem and compares two alternative elastic image registration methods for the purpose of motion estimation in cone-beam CT. An iterative method based on the optical flow theory is compared to a simpler and faster block-matching algorithm. Extensive experimentations have been conducted and key results are reported.

Summary and Future Work

Finally, this dissertation is finalized with a summary of the contributions and some propositions for future work. While supressing the influence of arbitrary patient motion on image quality has been the central problem tackled in this thesis, several pending problems and limitations of current solutions are still not solved yet. Therefore, many different tracks for future investigations are discussed in details.

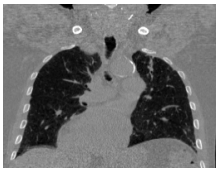

2

Image Reconstruction in Computed Tomography

Medical applications of computed tomography (CT) are nowadays a part of the daily clinical routine. This technique can produce very detailed volumetric *anatomical images*. The structures such as bones, the outer shape and inner details of organs can be visualized in three dimensions. With local injection of *contrast agent*, CT imaging can extract the shape of arteries and veins for imaging the cardiovascular network. Volumetric images ease the guidance of surgical interventions with catheters and are also used for outcome control.

Image reconstruction is the field of computational methods aiming at estimating a planar (2D) or volumetric (3D) image in function of the collection of X-ray projections from the image of interest. The dataset is often acquired for a limited field of view (FOV) by means of the transmission of X-ray through a physical object composed of various material's densities.

This chapter describes formally this data acquisition process and introduces the theoretical background necessary to justify the development of analytical solutions for solving the *inverse problem* of image reconstruction from line integrals. Additionally, the *algebraic* and *statistical* approaches to iterative image reconstruction are also introduced.

2.1 Acquisition of X-Ray Projections

X-ray transmission computed tomography (CT) reconstructs a volumetric attenuation image from several radiographies of a static object[1]. Digital radiographs are taken at different orientations during a sequential data acquisition phase. Image formation in CT transforms a collection of measured line integrals to an image of the spatial distribution of X-ray attenuation factors. The reconstructed image depicts the inside structures of the observed object.

To measure line integrals with X-ray transmission, high energy photons are generated by a X-ray tube and transmitted through the observed object. A certain

[1] In medical applications of CT, the observed object is alive and therefore never really static.

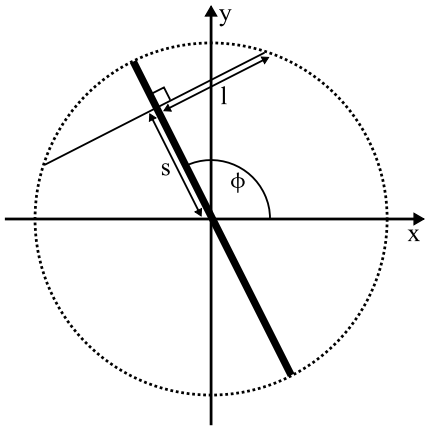

Figure 2.1: Parameterization of line integrals for the 2D parallel-beam geometry. Each line in the planar space of axis x and y is parameterized by the orientation of the detector ϕ and a signed distance to the origin s. The half-length of the line segment inside a limited field of view (FOV) is denoted by l. The thick line segment shows the virtual detector which passes through the origin and is orthogonal to the projection direction.

quantity of photons are *photo-absorbed* inside the body or scattered during their transport. The remaining light intensity is measured by a detector.

Raw data contains measured intensities, proportional to the number of photons that were not absorbed during their passage through the object lying in between the focus point of the X-ray tube and the detector's pixel. Knowing the initial emitted intensity, the input data are converted to digital tomographic projections that sample line integrals through the object that shall be reconstructed.

2.1.1 Beer's Law and Log Transform

Let $f(x, y) \to \mathbb{R}$ be a continuous two-dimensional function where $(x, y) \in \mathbb{R}^2$ are Cartesian spatial coordinates. One wants to acquire from f the line integrals $g(s, \phi) \to \mathbb{R}$, where $s \in \mathbb{R}$ and $\phi \in [0, \pi)$ are the signed distance from the origin and the angular coefficient of a line, respectively. The geometrical interpretation of the line integral parameters s and ϕ in the coordinate system of the function f is illustrated in figure 2.1.

Given $I_0 > 0$, the initial emitted intensity of the X-ray tube, the Beer's law says that the remaining intensity after attenuation along the line parameterized by the pair (s, ϕ) will be equal to

$$I(s, \phi) = I_0 \exp\left(- \int_{-\infty}^{\infty} f(s\cos\phi - t\sin\phi, s\sin\phi + t\cos\phi)\, dt \right), \tag{2.1}$$

where the function f represents the spatial distribution of linear X-ray attenuation factors.

In the above expression, the exponential's argument is the negative of the line integral through f. By posing

$$g(s, \phi) = \int_{-\infty}^{\infty} f(s\cos\phi - t\sin\phi, s\sin\phi + t\cos\phi)\, dt, \tag{2.2}$$

one can write the Beer's law in a more compact form as

$$I(s,\phi) = I_0\, e^{-g(s,\phi)}. \tag{2.3}$$

The relation between measured intensities and line integrals is made evident when isolating $g(s,\phi)$. The negative natural logarithm of the ratio between initial and measured intensities yields

$$g(s,\phi) = -\ln \frac{I(s,\phi)}{I_0}. \tag{2.4}$$

This conversion from relative intensities to line integrals process is commonly known as the "log transform". The collection of all line integrals $g(s,\phi)$ is called the Radon transform of f.

2.1.2 Practical Considerations

While reasoning from the Beer's law is theoretically sound, some practical considerations are important to point out. In practice, measured data are corrupted by secondary physical effects such as occlusion (Robertson *et al.*, 1988) (metalic objects), beam hardening (Hsieh *et al.*, 2000) (low energy photons are more likely to be photo-absorbed), Compton and Rayleigh scattering (Ning *et al.*, 2004; Rinkel *et al.*, 2007) (photons do not follow exactly linear paths). Furthermore, the limited dose and the photon count performances of the detector (Jaffray and Siewerdsen, 2000) limit the accuracy of measurements (the number of detected photons follows Poisson statistics).

Additional higher-order physical effects introduce optical blurring such as scattering inside the scintilator crystals of the detector. Electronic noise (approximately Gaussian) equally corrupts the raw measures of the detector. The capacity to deal with innacurate line integrals is the first challenge to overcome for the development of practical image reconstuction methods. Therefore, the two following sections focus on how to solve the image reconstruction problem with direct inversion and iterative approximation methods.

2.2 Analytical Image Reconstruction

The inverse problem of defining $f(x,y) \rightarrow \mathbb{R}$ from its lines integrals $g(s,\phi) \rightarrow \mathbb{R}$ has been tackled by Radon in 1917. His original article was written in German and has been translated to English and re-published in Transactions on Medical Imaging (Radon, 1986). The seminal work of Radon has provided the necessary mathematical background for the development of tomographic reconstruction algorithms.

Analytical image reconstruction methods compute images with closed-form solutions based on a fundamental mathematical relation shown by Radon: the *central-slice theorem*. This theorem shows that one can uniquely reconstruct the original attenuation image from a simple combination of the information from each projection in Fourier space. However, analytical methods assume that an infinite number of measures are available. In practice, the size of the dataset is limited, and a lot of noise is present in the measures.

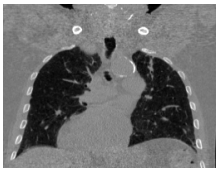

This section defines the central-slice theorem that relates the two-dimensional Fourier transform of the attenuation distribution to the one-dimensional Fourier transform of a parallel projection. A parallel projection is defined as a set of integrals along a family of parallel lines. Based on the theory of the Radon transform, the direct Fourier reconstruction and the filtered backprojection (FBP) algorithms are derived. Furthermore, the FDK algorithm for cone-beam geometry is presented.

2.2.1 Fourier Transform

Consider a function $f(x, y)$ representing a planar image defined in the spatial domain. The two-dimensional Fourier transform $F(v_x, v_y)$ maps the function $f(x, y)$ from spatial to frequency domain:

$$F(v_x, v_y) = \int_{-\infty}^{\infty} \int_{-\infty}^{\infty} f(x, y)\, e^{-2\pi i(xv_x + yv_y)} dx dy. \tag{2.5}$$

The inverse Fourier transform is defined in a very similar way, only the sign of the argument of the exponential is changed and the integration holds in the frequency domain:

$$f(x, y) = \int_{-\infty}^{\infty} \int_{-\infty}^{\infty} F(v_x, v_y)\, e^{2\pi i(xv_x + yv_y)} dv_x dv_y. \tag{2.6}$$

In the same way, consider a function $g(s, \phi)$, representing a one-dimensional projection, defined in the spatial domain. The associated one-dimensional Fourier transform $G(v, \phi)$ is defined by

$$G(v, \phi) = \int_{-\infty}^{\infty} g(s, \phi)\, e^{-2\pi isv} ds, \tag{2.7}$$

while the one-dimensional inverse Fourier transform of $G(v, \phi)$ recovers the original projection data, hence

$$g(s, \phi) = \int_{-\infty}^{\infty} G(v, \phi)\, e^{2\pi isv} dv. \tag{2.8}$$

2.2.2 Central-Slice Theorem

The central-slice theorem states that the one-dimensional Fourier transform of the Radon transform with respect to the signed distance s is related to the two-dimensional Fourier transform of the function f:

$$G(v, \phi) = F(v \cos\phi, v \sin\phi).$$

This relation holds for any projection angle ϕ and is a direct consequence of the invariance for translation of the Radon transform. This theorem is proven by first writing explicitly the Fourier transform $G(v, \phi)$ and by replacing the Radon transform $g(s, \phi)$ by its definition as line integral of f:

$$G(v, \phi) \quad = \quad \int_{-\infty}^{\infty} g(s, \phi)\, e^{-2\pi isv} ds$$

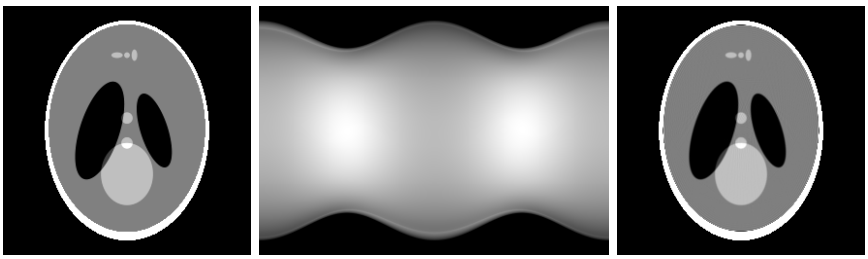

(a) Phantom (b) Sinogram (c) Reconstruction

Figure 2.2: Analytical reconstructions of the 2D Shepp-Logan head phantom (a) from its Radon transform (b). Each column of the dataset contains the 1D signal corresponding to one specific projection angle. Since the trajectory of projected points follows sinusoidal curves. The FBP reconstruction (c) uses a limited amount of data and therefore is always an approximation of the original image.

$$\begin{aligned} &= \int_{-\infty}^{\infty}\int_{-\infty}^{\infty} f\left(s\cos\phi - t\sin\phi, s\sin\phi + t\cos\phi\right) e^{-2\pi isv} dtds \\ &= \int_{-\infty}^{\infty}\int_{-\infty}^{\infty} f\left(x,y\right) e^{-2\pi iv(x\cos\phi + y\sin\phi)} dxdy \\ &= F\left(v\cos\phi, v\sin\phi\right) \end{aligned} \tag{2.9}$$

In the above derivation, the polar parameter s was related to the Cartesian coordinates x and y with the following changes of variables:

$$\begin{cases} x &= s\cos\phi - t\sin\phi \\ y &= s\sin\phi + t\cos\phi \end{cases} \tag{2.10}$$

Then, by multiplying the first and second equations by respectively $\cos\phi$ and $\sin\phi$, we get

$$\begin{cases} x\cos\phi &= s\cos^2\phi - t\sin\phi\cos\phi \\ y\sin\phi &= s\sin^2\phi + t\cos\phi\sin\phi \end{cases} \tag{2.11}$$

and finally, summing these two equations yields an expression for s:

$$x\cos\phi + y\sin\phi = s\left(\cos^2\phi + \sin^2\phi\right) = s. \tag{2.12}$$

2.2.3 Direct Fourier Reconstruction

A direct application of the central-slice theorem is that the whole Fourier transform F of an image $f\left(x,y\right) \to \mathbb{R}$ where $(x,y) \in \mathbb{R}^2$ can be recovered if the projections $g_\phi\left(s\right) \to \mathbb{R}$ are measured for all orientations $\phi \in [0,\pi)$. This leads to an algorithm known as "direct Fourier reconstruction".

The direct Fourier reconstruction algorithm processes each measured projection angle ϕ and sets $F\left(v\cos\phi, v\sin\phi\right) = G\left(v,\phi\right)$ where F and G are the two- and one-dimensional Fourier transform of f and g, respectively. The two-dimensional inverse Fourier transform of F is the reconstructed image f in the spatial domain. The implementation of a discrete version of this algorithm can be made efficient by relying on a standard implementation of the fast Fourier transform (FFT).

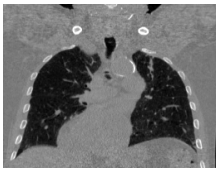

Center	Radii	Rotation	Density
(0,0,-0.25)	(0.69,0.92,0.9)	0	2
(0,-0.0184,-0.25)	(0.6624,0.874,0.88)	0	-0.98
(-0.22,0,0)	(0.41,0.16,0.21)	-72	-0.02
(0.22,0,0)	(0.31,0.11,0.22)	72	-0.02
(0,0.35,0)	(0.21,0.25,0.35)	0	0.01
(0,0.1,0)	(0.046,0.046,0.046)	0	0.01
(0,-0.1,0)	(0.046,0.046,0.046)	0	0.01
(-0.08,-0.605,0)	(0.046,0.023,0.02)	0	0.01
(0.06,-0.605,0)	(0.046,0.023,0.02)	-90	0.01
(0.06,-0.105,-0.875)	(0.056,0.04,0.1)	-90	0.02
(0,0.625,0.1)	(0.056,0.056,0.1)	0	-0.02
(0,-0.605,0)	(0.023,0.023,0.023)	0	0.01

Table 2.1: Geometrical definition of the mathematical low-contrast 3D Shepp-Logan phantom. The object is defined by twelve ellipsoids whose centers and elliptic radii are indicated in the two first columns. The ellipsoids are oriented by the rotation around the depth axis. The rotation angles in degree and the associated densities are indicated in the two last columns. Note that the 2D Shepp-Logan phantom is defined by the ten ellipses in intersection with the plane $z = 0$.

A drawback of the direct Fourier reconstruction technique is that interpolations are required to transform line integrals from polar coordinates (v, ϕ) to Cartesian coordinates (v_x, v_y). An alternative application of the central-slice theorem is the filtered backprojection (FBP) algorithm.

2.2.4 Filtered Backprojection (FBP)

The FBP inversion implicitly avoids the conversion from Cartesian to polar coordinates. The algorithm can be derived by first expressing the reconstructed image $f(x, y)$ as a two-dimensional inverse transformation of its Fourier transform $F(v_x, v_y)$:

$$f(x, y) = \int_{-\infty}^{\infty} \int_{-\infty}^{\infty} F(v_x, v_y)\, e^{2\pi i (x v_x + y v_y)} dv_x dv_y. \tag{2.13}$$

The straightforward change from Cartesian (v_x, v_y) to polar (v, ϕ) coordinate systems yields the following expression:

$$f(x, y) = \int_{0}^{2\pi} \int_{0}^{\infty} v\, F(v\cos\phi, v\sin\phi)\, e^{2\pi i v (x\cos\phi + y\sin\phi)} dv d\phi. \tag{2.14}$$

By the central-slice theorem, $F(v\cos\phi, v\sin\phi)$ is rewritten as $G(v, \phi)$ and the $(x\cos\phi + y\sin\phi)$ exponent is rewritten as s. The expression can be rewritten in the following shorten form:

$$f(x, y) = \int_{0}^{2\pi} \int_{0}^{\infty} v\, G(v, \phi)\, e^{2\pi i v s} dv d\phi. \tag{2.15}$$

Finally, by symmetry of trigonometric functions and symmetry of the Radon transform, i.e. $g(s, \phi) = g(-s, \phi + \pi)$, the integration can be limited to half of the

angular domain:

$$f(x,y) = \int_0^{\pi} \int_{-\infty}^{\infty} |v| \, G(v,\phi) \, e^{2\pi i v s} dv d\phi. \tag{2.16}$$

The first integral over all possible orientations $0 \leq \phi < \pi$ is the backprojection operator. In this case, the backprojection is applied to the inverse Fourier transform of $|v| \, G(v,\phi)$.

The weighting function $|v|$ is linearly increasing. Therefore, high-frequencies contributions are emphasized and the reconstruction will be very sensitive to high-frequency noise in the data. For this reason, and unfortunately, tomographic reconstruction is an ill-conditioned problem and often a low-pass smoothing filter is used to attenuate high frequencies in the data. This appodization introduces some blurring in the reconstructed image. Blurring alleviates noise artifacts, but also limits the intrinsic image resolution.

FBP Algorithm

Implementation of FBP usually splits the reconstruction in two successive steps. In the first step, each projection $g(s,\phi)$ is filtered:

$$\begin{aligned} g^*(s,\phi) &= \int_{-\infty}^{\infty} |v| \, G(v,\phi) \, e^{2\pi i v s} dv \\ &= \int_{-\infty}^{\infty} h\left(s - s'\right) g\left(s', \phi\right) ds' \\ &= [g * h](s,\phi) \end{aligned} \tag{2.17}$$

As seen by the last expression, this operation is a simple one-dimensional convolution of the projection with the following *ramp filter*:

$$h(s) = \int_{-\infty}^{\infty} |v| \, e^{2\pi i v s} dv. \tag{2.18}$$

In the second step, all filtered projections are backprojected to image space to reconstruct the original image:

$$\begin{aligned} f(x,y) &= \int_0^{\pi} g^*(s,\phi) \, d\phi \\ &= \int_0^{\pi} g^*(x\cos\phi + y\sin\phi, \phi) \, d\phi \end{aligned} \tag{2.19}$$

The two-step filtering and backprojection formulation allows the reconstruction of an image function f from its line integrals without requiring back and forth Fourier transformations and without explicit interpolation between polar and Cartesian grids. The former theory is derived for two-dimensional images only. However, the volumetric reconstruction problem can be reduced to reconstructing independent two-dimensional slices for each row of the detector.

Figure 2.2 shows the result of a FBP reconstruction from 1024 projections of the mathematical 2D Shepp-Logan phantom (Shepp and Logan, 1974). The phantom is defined by twelve ellipsoids of various size, position, orientation and density. The geometric parameters of the 3D Shepp-Logan phantom are presented in Table 2.1.

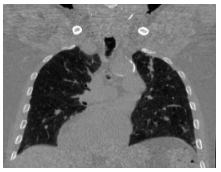

Windowing the Ramp Filter

As motivated above, since the integral $h(s)$ is not convergent, one could choose to attenuate high-frequencies in the reconstructed image. For example, one could limit the lower and upper bounds of the integration variable to a finite range. However, it is more common to apodize progressively the ramp kernel with a low-pass window $w(v)$:

$$h_w(s) = \int_{-\infty}^{\infty} w(v) |v| e^{2\pi i v s} dv, \tag{2.20}$$

where the Hanning window with cut-off frequency v_{cut} defined below has been used to "bend" the ramp function $|v|$:

$$w(v) = \begin{cases} \frac{1+\cos(\pi v / v_{cut})}{2} & |v| \leq v_{cut} \\ 0 & |v| > v_{cut} \end{cases} \tag{2.21}$$

The value of the window function smoothly decreases with increasing absolute values of the frequency parameter v. Therefore, high-frequency contributions smoothly vanish instead of being hardly clamped when using the apodized ramp kernel filter $h_w(s)$.

2.2.5 Feldkamp-Davis-Kress (FDK)

In 1984, Feldkamp, Davis and Kress published the so-called FDK method (Feldkamp *et al.*, 1984), a practical FBP algorithm for cone-beam geometry. In comparison to a regular FBP implementation, their technique requires only slight modifications of the filtering and backprojection steps. Namely, the line integrals projections must be weighted prior to ramp filtering and an additional weighting is incorporated in the backprojection.

It is important to mention that for circular acquisitions, it is theoretically impossible to reconstruct the object exactly. Indeed, Tuy (1983) proved a sufficiency condition for exact reconstruction in cone-beam geometry. This simple condition state that an exact reconstruction is possible for slices crossed by the the trajectory of the X-ray source. Smith (1985) proved that this simple condition is not only sufficient, but necessary. Therefore, the literature mentions often jointly the necessary and sufficient conditions of Tuy-Smith (Schomberg *et al.*, 2009).

Although many variants and alternatives to the original FDK method have been suggested, the success of FDK is tremendeous. Its simplicity and its very fast execution speed are certainly the two key factors for its widespread adoption. In the central slice, the FDK algorithm reduces to FBP for the fan-beam geometry and therefore FDK produces exact reconstruction in this transversal section.

Perspective Projection and Backprojection

Data acquisition in divergent rays geometries and a circular trajectory can be parameterized by the time-varying position of the X-ray source, its distance to the rotation axis R, and the distance from the rotation axis to the detector D. When

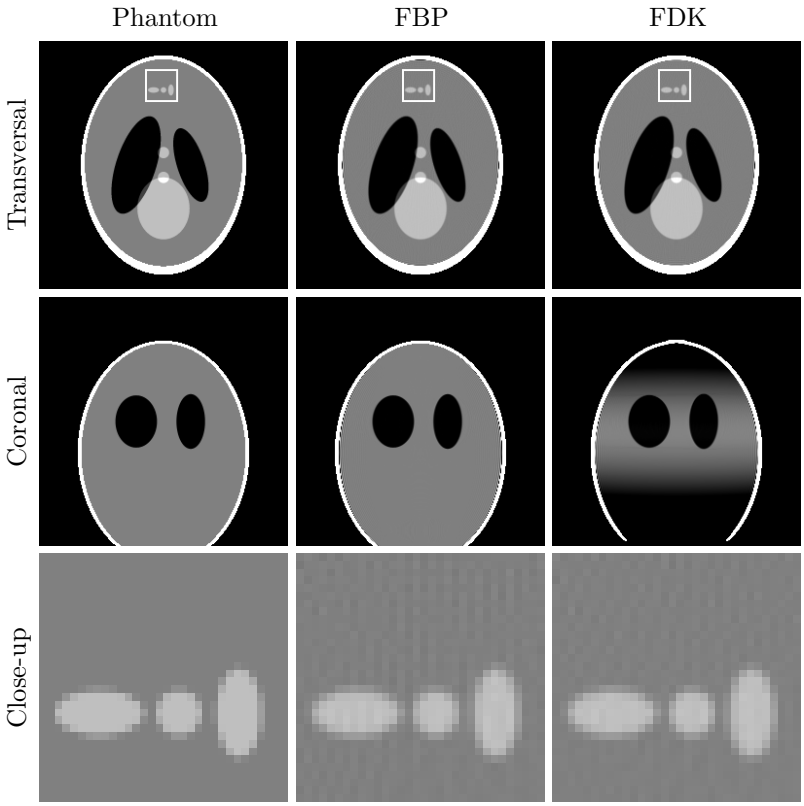

Figure 2.3: Analytical reconstructions of the 3D Shepp-Logan phantom with the FBP and FDK methods. The reconstruction is exact in the central transversal slice for both methods. However, a characteristic intensity drop is observed in coronal slices with FDK. The corresponding slices from the voxelized reference phantom image are shown as well for comparison purpose. The white square shows the boundaries of close-up views.

the gantry is oriented at angle $\phi \in [0, 2\pi)$, the perspective projection operator

$$P_\phi(x, y, z) = (y\cos\phi - x\sin\phi, z)\,\frac{(R+D)}{U} \tag{2.22}$$

maps a point $(x, y, z) \in \mathbb{R}^3$ defined in object space to a point $(u, v) \in \mathbb{R}^2$ defined in projection space.

The denominator in (2.22) is the *perspective factor*

$$U = U_\phi(x, y) = R + x\cos\phi + y\sin\phi \tag{2.23}$$

which is equal to the distance between the source and the orthogonal projection of the voxel position on the central plane. The central plane contains the source point and is orthogonal to the rotation axis.

The adjoint of the perspective projection operator

$$P'_\phi(u, v) = (-u\sin\phi, u\cos\phi, v)\,\frac{R}{(R+D)} \tag{2.24}$$

maps a point $(u, v) \in \mathbb{R}^2$ defined in projection space to a point on a *virtual detector*

defined in object space. The constant ratio $M = R\,/\,(R+D)$ is also called the *magnification factor*. The virtual detector shares the same orientation with the real one but is smaller, proportionally to M, and centered on the origin of the FOV.

Divergent Ray Integrals

Let $f(x,y,z) \rightarrow \mathbb{R}$ be a volumetric image where $(x,y,z) \in \mathbb{R}^3$ are Cartesian coordinates in image space. The function f is compactly supported in the cylindrical FOV such that $f(x,y,z) = 0$ when $\sqrt{x^2+y^2} > D$. Let $g_\phi(u,v) \rightarrow \mathbb{R}$ be the line integrals of f where $(u,v) \in \mathbb{R}^2$ are Cartesian coordinates in projection space and $\phi \in [0, 2\pi)$ is the orientation of the detector.

When the gantry is oriented at angle $\phi \in [0, 2\pi)$, the position of the point source is equal to $R\,\vec{d}_\phi$ where the vector $\vec{d}_\phi = (\cos\phi, \sin\phi, 0)$ is normal to the detector plane. Therefore, the values of acquired line integrals are equal to

$$g_\phi(u,v) = \int_{-1}^{1} f\left(t\,P'_\phi(u,v) + (1-t)\,R\,\vec{d}_\phi\right) dt. \tag{2.25}$$

In this expression, the points on the integrated line segment connecting the X-ray source to a pixel of the detector are selected by varying the integration parameter t.

FDK Algorithm

The FDK reconstruction proceeds in three successive steps. First, the projection data are pre-weighted such that

$$g'_\phi(u,v) = g_\phi(u,v)\,\frac{R+D}{\sqrt{R^2+S}}, \tag{2.26}$$

where $S = M^2\left(u^2+v^2\right)$ is the squared distance between the detector pixel (u,v) and the central transversal plane.

Second, pre-weighted line integrals are convolved with a ramp filter h. The derivation of the filter is identical to the parallel-beam case. The pre-weighted filtered projections are noted

$$g^*_\phi(u,v) = \left[g'_\phi * h\right](u,v). \tag{2.27}$$

Finally, a perspective backprojection is applied independently for each voxel of the reconstructed volume:

$$f(x,y,z) = \int_0^{2\pi} \frac{R^2}{U^2} g^*_\phi\left(P_\phi(x,y,z)\right) d\phi, \tag{2.28}$$

where R^2/U^2 is the weighting factor for backprojection.

Figure 2.3 presents a visual comparison of the reconstruction of the conventional 3D Shepp-Logan phantom defined by Table 2.1. The exact reconstruction of FBP in parallel-beam is compared to the approximate result from FDK in cone-beam geometry.

While the reconstruction is exact in the central slice with FDK, some inaccuracies appear for slices that are shifted along the axial direction. The typical intensity drop

	Iteration per **dataset**	Iteration per **projection**	Iteration per **ray**
Algebraic	SIRT	SART	ART
Statistical	MLEM	RAMLA	-

Table 2.2: A classification of some key algebraic and statistical iterative image reconstruction methods. The granularity of methods can be sorted according to the frequency of image updates (iteration or sub-iteration). It seems that no statistical algorithm has been implemented yet for tomographic image reconstruction with ray-by-ray image updates.

is symptomatic of the so-called cone-beam artifacts that are unavoidable with the plain FDK method. Some modifications of the backprojection weighting overcome partially the cone-beam artifacts (Hu, 1996; Zhu *et al.*, 2007). Another solution proposed by Hsieh (2000, 2003) is to reconstruct the artifacts for correcting the image in a second reconstruction pass.

2.3 Iterative Image Reconstruction

Iterative image reconstruction refers to the broad family of techniques that do not rely on closed-form analytical inversions but on progressive improvement of an image estimate. The computational performances of iterative reconstruction methods are not as attractive as analytical solutions; however, their intrinsic flexibility can account with ease practical issues such as Gaussian or Poisson noise modeling or an accurate simulation of the physics of photon transport including physical effects such as beam hardening and scattering.

Iterative methods are classified into two categories: *algebraic* and *statistical* reconstruction algorithms. Many alternative reconstruction techniques can be found in the literature and only four of them are compared in this section. Table 2.2 classifies the specific methods of interest: the algebraic SIRT and SART algorithms and the statistical MLEM and RAMLA algorithms.

While the MLEM and RAMLA have been derived for the Poisson noise model in emission tomography, those algorithms can be applied safely for the reconstruction from noise-free line integrals. Indeed, the experiments reconstruct a mathematical phantom object for which perfect line integral data can be generated. In this case, both algebraic and statistical methods should converge to the same unique image. However, small discrepancies appears in practice, due to specific numerical properties of the arithmetical operations and the unavoidable inacuracies of integration and interpolation methods.

2.3.1 Algebraic Algorithms

The very first image reconstruction method used by Hounsfield in 1971 was an implementation of the method of projections by Kaczmarz (1937), also known as the algebraic reconstruction technique (ART) that was developed by Gordon *et al.* (1970). Later, this technique was superseded by the faster FBP methods (Pan *et al.*, 2009). However, with the ever increasing computational power, algebraic methods have regained some popularity.

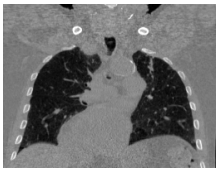

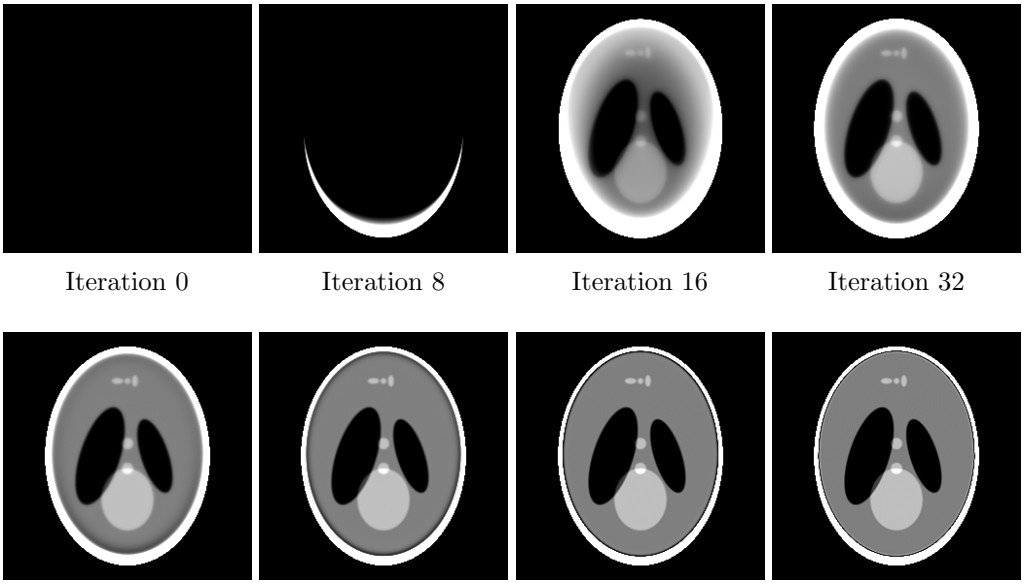

Figure 2.4: Iterative reconstruction of the Shepp-Logan phantom with the simultaneous iterative reconstruction technique (SIRT).

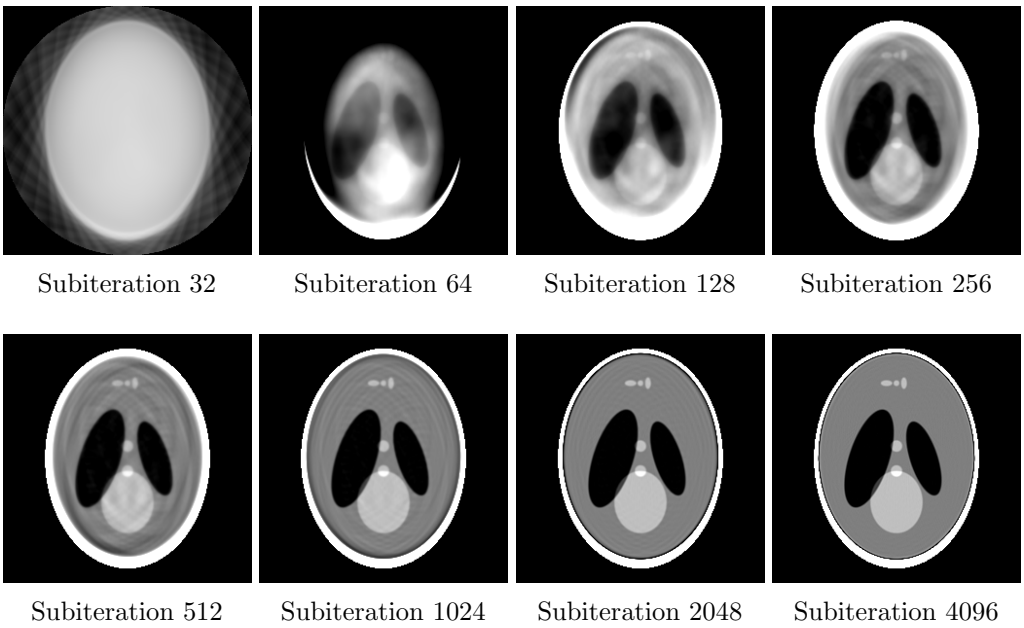

Figure 2.5: Iterative reconstruction of the Shepp-Logan phantom with the simultaneous algebraic reconstruction technique (SART). The relaxation parameter was set to $\lambda = 0.2$. For a better vizualization at the early stage of the reconstruction, the window level and width of the first image have been set to 0.6 and 0.8 respectively.

This section will present formally the simultaneous iterative reconstruction technique (SIRT) and the faster simultaneous algebraic reconstruction technique (SART) introduced as a superior implementation of ART[2] by Andersen and Kak (1984). The convergence speed of those more modern implementations is by nature slower than the ART method (Jiang and Wang, 2003). However, they demonstrated superior image quality (Andersen, 1989) and define the current state of the art of iterative algebraic reconstructions.

Algebraic methods model the image formation problem as the following system of linear equations

$$Af = g, \tag{2.29}$$

where g is a vector containing the line integrals measured from the original image f. A discrete-discrete problem is defined if both the set of measurements M is finite and the set of image elements N is finite as well. The elements A_{ij} of the system matrix A contains the (partial) contributions of measurements g_i, $i \in M$ to image elements f_j, $j \in N$.

Instead of storing explicitly the system matrix A, the value of its elements A_{ij} are usually computed on the fly by ray-tracing techniques. When processing a given line integral g_i, every element f_j along the path of the line integral are directly accessed by the ray-tracer. An approximation of f will be iteratively estimated from g. In practice, the number of measurements exceeds the number of unknown image elements and the system is said to be over-determined. Therefore, the solution is not unique if data are inconsistent.

SIRT

Starting from an empty image at iteration $n = 0$, the SIRT algorithm updates each image element f_j, $j \in N$ at iteration $n > 0$. The update is defined by

$$f_j^{n+1} = f_j^n + \frac{1}{S_j} \sum_{i \in M} \frac{A_{ij}}{\sum_{j \in N} A_{ij}} \left(g_i - \hat{g}_i^n \right), \tag{2.30}$$

where each update factor depends on the average difference between measured line integrals g_i, $i \in M$ and their corresponding forward projection from the current image $\hat{g}_i^n = \sum_{j \in N} A_{ij} \, {f_j}^n$. The sensitivity term $S_j = \sum_{i \in M} A_{ij}$ normalizes the correction term by the total of contributions from line integrals passing through the given image element f_j, $j \in M$.

The progressive image reconstruction of the Shepp-Logan phantom can be appreciated in figure 2.4. To model the finite size of detector bins, each projection contains 256 measures that are computed by averaging 16 parallel line integrals evaluated from the mathematical definition of the phantom. This process effectively computes strip integrals to attenuate the aliasing generated by sharp transitions between ellipsoids.

The dataset consists of a large number (1024) of non-truncated noise-free projections in parallel-beam geometry. This classical setup is the most favorable case for analytical reconstruction algorithms. Nevertheless, the final reconstructed im-

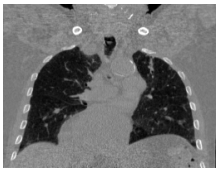

[2]It can be said that the implementation of every image reconstruction algorithm is more than a technical task, but also a kind of art.

age tends to be more regular and contains less streaks in comparison with the FBP reconstruction of figure 2.2 (c) in the preceding chapter.

SART

In contrast to the SIRT method, the SART algorithm updates the current image estimate for each batch of line integrals corresponding to a carefully chosen projection angle α. Since the image is updated before processing the whole corpus of data, the convergence speed is faster than SIRT. In addition, the running time does not depend anymore on the number of projections present in the dataset. In practice, a relaxation factor $0 < \lambda < 2$ is used to limit the convergence speed and stabilize the estimation process when inconsistent data are used.

The value of image element f_j, $j \in N$ at the subiteration $n > 0$ is defined by

$$f_j^{n+1} = f_j^n + \lambda \left[\frac{1}{S_j^\alpha} \sum_{i \in M^\alpha} \frac{A_{ij}}{\sum_{j \in N} A_{ij}} (g_i - \hat{g}_i^n) \right], \tag{2.31}$$

where each update factor depends on the difference between a subset of the measured line integrals g_i, $i \in M^\alpha$ when the detector is oriented at angle $0 \leq \alpha < 2\pi$ and the forward projection from the current image f^n. This update factor is multiplied by the relaxation parameter λ and normalized by sensitivity term $S_j^\alpha = \sum_{i \in M^\alpha} A_{ij}$.

The ordering or projections and the choice of the relaxation factor is critical for tuning the performances of the method (Herman and Meyer, 1993; Strohmer and Vershynin, 2009). For the experiments, the projections have been selected according to a golden search rule that was suggested by Köhler (2004). The relaxation factor has been set to the conservative constant $\lambda = 0.2$ (Trummer, 1984). The image formation, starting from an empty image, can be appreciated in figure 2.5.

2.3.2 Statistical Algorithms

Algebraic algorithms cast the image reconstruction problem as solving a system of linear equations. By slightly updating the current image estimate at each iteration, the solution that matches the data in the least square sense is iteratively approached. In constrast to algebraic methods, statistical algorithms maximize iteratively the probability of observing the input data from the current image estimate. This approach exploits the statistical nature of the data and tends to avoid artifacts in reconstructed images more efficiently.

Traditional statistical image reconstruction methods are based on the iterative expectation-maximization (EM) algorithm described in the seminal paper of Dempster, Laird and Rubin in 1977 (Dempster *et al.*, 1977). The EM optimization method is used to approach maximum likelihood estimates of classical machine learning problems such as the estimation of maximum likelihood Gaussian mixture models. Applying EM for tomographic image reconstruction was first proposed in the context of emission tomography by Shepp and Vardi (1982). The EM algorithm has been quickly adapted to transmission tomography by Lange and Carson (1984).

Since then, many successive improvements have been discussed in the literature. A lot of work was adopting the Bayesian approach of maximum *a-posteriori* (MAP)

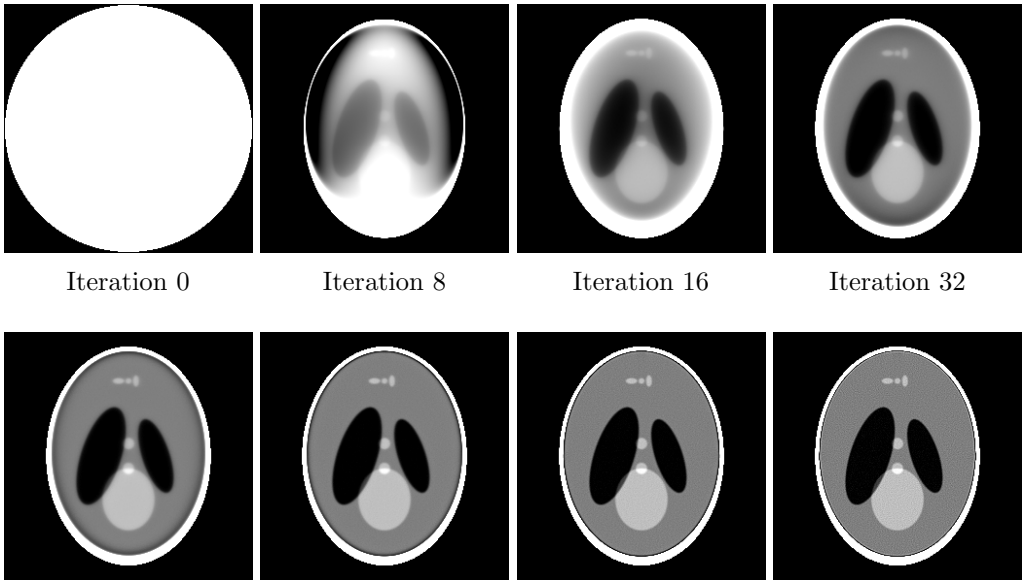

Figure 2.6: Iterative reconstruction of the Shepp-Logan phantom with maximum likelihood expectation-maximization (MLEM).

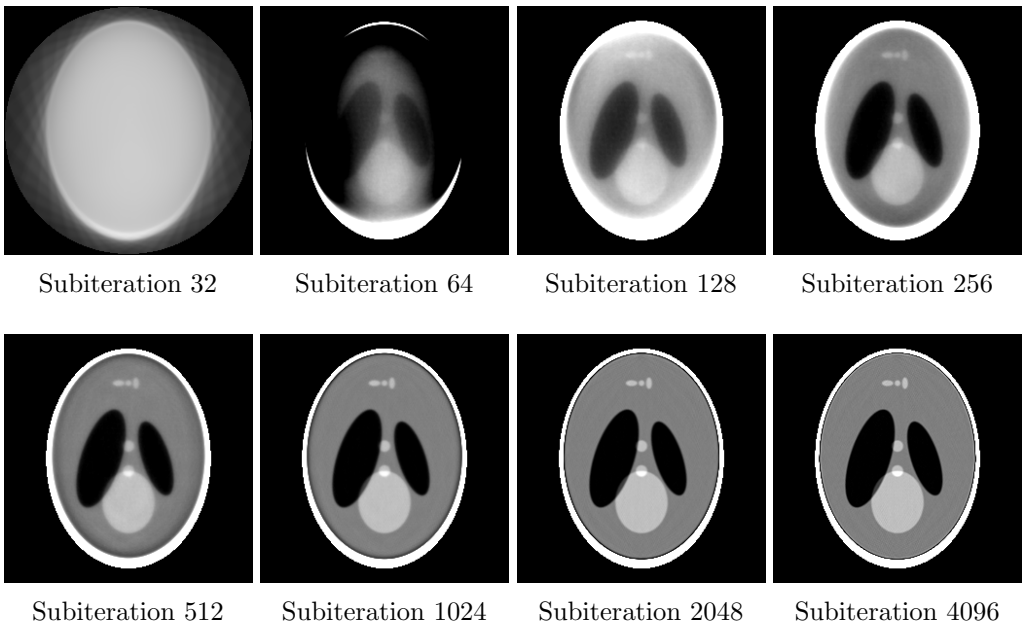

Figure 2.7: Iterative reconstruction of the Shepp-Logan phantom with the row-action maximum likelihood algorithm (RAMLA). The relaxation parameter was set to $\lambda = 0.1$. For a better vizualization at the early stage of the reconstruction, the window level and width of the first image have been set to 0.6 and 0.8 respectively.

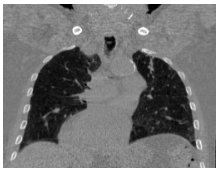

estimation to regularize the maximum likelihood objective (Lange and Fessler, 1995). Another branch of investigation is improving convergence speed by using subsets of the whole data. The paper of Hudson and Larkin (1994) introducing the faster, but non-convergent, ordered subset EM (OSEM) was a milestone.

Later, the use of subsets was extended to a convergent ordered subset algorithm using complete data (COSEM) in emission tomography by Hsiao *et al.* (2004). In transmission, methods such as the ordered subset convex algorithms proposed by Kamphuis and Beekman (1998) or the convergent incremental optimisation transfer algorithm of Ahn *et al.* (2006) are representatives of the state-of-the-art in tomographic iterative image reconstruction.

Among the wide collection of existing statistical reconstruction algorithms, this section will only present formally the very first maximum likelihood expectation-maximization (MLEM) method of Shepp and Vardi (1982) and the faster row-action maximum likelihood algorithm (RAMLA) by Browne and De Pierro (1996). Those two methods are older but nevertheless, their underlying principles influenced in a great part the direction of current research investigations.

MLEM

Starting from a positive-definite initial image at iteration $n = 0$, the MLEM algorithm updates each image element f_j, $j \in N$ at iteration $n > 0$. The update is defined by

$$f_j^{n+1} = f_j^n \frac{1}{S_j} \sum_{i \in M} A_{ij} \left(g_i / \hat{g}_i^n \right), \tag{2.32}$$

where each update factor depends on the average ratio between measured line integrals g_i, $i \in M$ and their corresponding forward projection from the current image $\hat{g}_i^n = \sum_{j \in N} A_{i,j} f_j^n$. The sensitivity term $S_j = \sum_{i \in M} A_{ij}$ normalizes the correction term by the total of contributions from line integrals passing through the given image element f_j, $j \in M$.

The MLEM equation shares a striking ressemblance with SIRT. A division instead of a difference is used to evaluate the discrepancy between acquired line integrals g_i and the forward projection from the current image. Accordingly, the value of each image element is corrected by multiplying the correction factor while SIRT relies on incremental image update. The current image at several selected iterations is shown in figure 2.6.

RAMLA

In contrast to the MLEM method, the RAMLA updates the current image estimate for each batch of line integrals corresponding to a carefully chosen projection angle α. This approach has striking similarities with SART, at the sole difference that the data discrepancy is evaluated by the ratio instead of the difference with the forward projected line integrals. A relaxation factor equal to $\lambda = 0.1$ has been used.

The value of image element f_j, $j \in N$ at the subiteration $n > 0$ is defined by

$$f_j^{n+1} = (1 - \lambda) f_j^n + \lambda \left[f_j^n \frac{1}{S_j^\alpha} \sum_{i \in M^\alpha} A_{ij} \left(g_i / \hat{g}_i^n \right) \right], \tag{2.33}$$

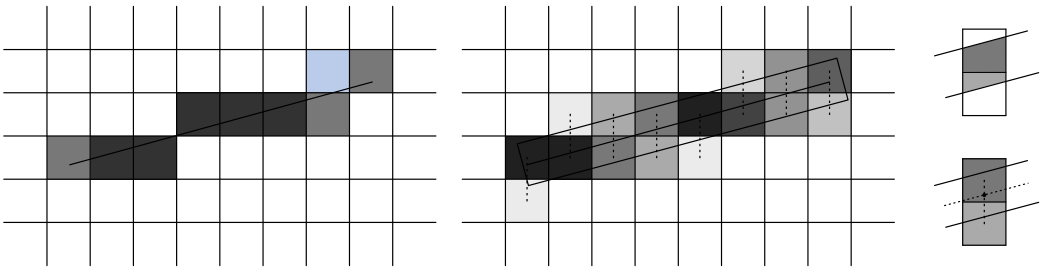

(a) Siddon ray-tracing (b) Joseph ray-tracing (c)

Figure 2.8: Siddon (a) and Joseph (b) ray-tracing results. The tones of black are proportional to the lengths of the intersection between the line and pixels for Siddon and are proportional to an approximation of the intersection areas between the strip and pixels for Joseph. The dotted segments link the centers of the two pixels, closest to the central line of the strip in (b). In (c), the ideal strip area (up) is approximated by the length of the vertical projection on the central line of the strip (down).

where each update factor depends on the difference between a subset of the measured line integrals g_i, $i \in M^\alpha$ when the detector is oriented at angle $0 \leq \alpha < 2\pi$ and the forward projection from the current image f^n. The projection ordering follows the same strategy as the one used for the SART method.

The relaxation factor λ is used to interpolate linearly between the current value of image elements and the updated estimate, using solely the line integrals of the projection measured at angle α. Note that if $\lambda = 1$ and if $M^\alpha = M$, then the RAMLA reduces to the MLEM algorithm.

The rationale of the RAMLA is to slightly update the image estimate more often, using the partial information of the line integrals measured at the current projection angle α. The image formation process can be seen in figure 2.7. One can remark that one iteration of MLEM processes the whole dataset and therefore the convergence speed depends on the number of acquired projections. With one image update per projection, the convergence speed of RAMLA becomes independent upon the number of acquired projection angles.

2.3.3 Forward Projection

Two projection operators are of main importance for iterative reconstruction since most of the running time is spent in these two routines. The *forward projection* from image space to projection space is defined as the integral of all image elements along a given line. The *backprojection* from projection space to image space is defined as the integral of all lines passing through a given image element.

Forward projections are usually implemented by a ray-tracing procedure. Xu and Mueller (2006) explained that ray-tracing algorithms can be seen as a composition of a line integration and an image interpolation method . Two classical methods are commonly used in the iterative image reconstruction community, namely, the Siddon's method published in 1985 and the alternative, more accurate, Joseph's method that was published earlier in 1982.

Siddon (1985) uses exact line integration but requires nearest neighbor interpolation that performs very poorly in practice. Joseph (1982) relies on approximate

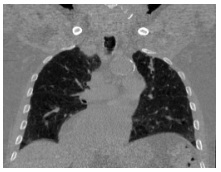

integration and linear interpolations and this method demonstrates higher accuracy than Siddon. In a previous work (Schretter, 2006), a fast ray-tracing implementation based on fixed step integration and linear interpolation is evaluated.

Figure 2.8 compares qualitatively the Siddon and Joseph methods. Previous experiments on the reconstruction of PET data have demonstrated an accuracy comparable to Joseph (Brinks *et al.*, 2006), while the running-time performances are improving over the fastest incremental implementation of the Siddon ray-tracer (Jacobs *et al.*, 1998; Christiaens *et al.*, 1999; Zhao and Reader, 2003).

Ray-tracing in CT is a sibbling of line drawing algorithms in computer graphics such as the Bresenham (1965) and Wu (1991) algorithms: two of the most representative solutions. In the image reconstruction community, the implementation of ray-tracing methods is a topic on itself and a multitude of alternative methods are developed today. It should be noted that the newest distance-based approach of De Man and Basu (2002, 2004) is increasingly popular and has been applied for reconstructing clinical images (Thibault *et al.*, 2007).

Many alternative forward projectors have been compared to the distance-driven implemementation. For example, Sunnegardh and Danielsson (2007) and Long *et al.* (2009) rely on a discrete integration model similar to Joseph but use integrated footprints of triangle and square kernels, respectively. In fact those implementations are equivalent to a convolution with the image element kernel and thus implicitly smoothen the image. Smoothing alleviates aliasing artifacts but also attenuates higher frequency content.

2.3.4 Antialiasing

The derivation of analytical image reconstruction algorithms often uses the continuous-continuous model for representing both the projection data and the image as continuous functions. In practice, data are binned into a digital signal representation and the image domain is covered by a finite amount of image elements. Therefore, the derivation of iterative methods assumes a discrete-discrete model, exactly the opposite of analytical approaches.

The discrete-discrete model traditionally assumes that image elements are square or cubic shaped (Blinn, 2005). It is well known that this choice leads to strong aliasing artifacts in general image processing (Blinn, 1989a,b). Alternative representations based on smooth basis functions have been used as well to represent images (Lewitt, 1992; Matej and Lewitt, 1995) and results show clear improvements in terms of noise to resolution trade-off. Unfortunately, computation of forward projections is more complex (Ziegler *et al.*, 2006) and the correction of remaining aliasing is not adressed by those works.

Aliasing artifacts arise also in the practice of image reconstruction in CT (Zbijewski and Beekman, 2004, 2006) because either the definition of the original acquired projection is insufficient or because of integration or interpolation artifacts when computing forward projections in digital images. Those two specific problems have been experimented and a simple solution is proposed, as shown in figure 2.9.

In the experiment, a simple forward projector based on a fixed step discrete integrator (the Euler method) was combined to a simple trilinear image interpolation model (Köhler *et al.*, 2000). While aliasing could be partially compensated by implementing image blurring within the forward and backprojections, the approach

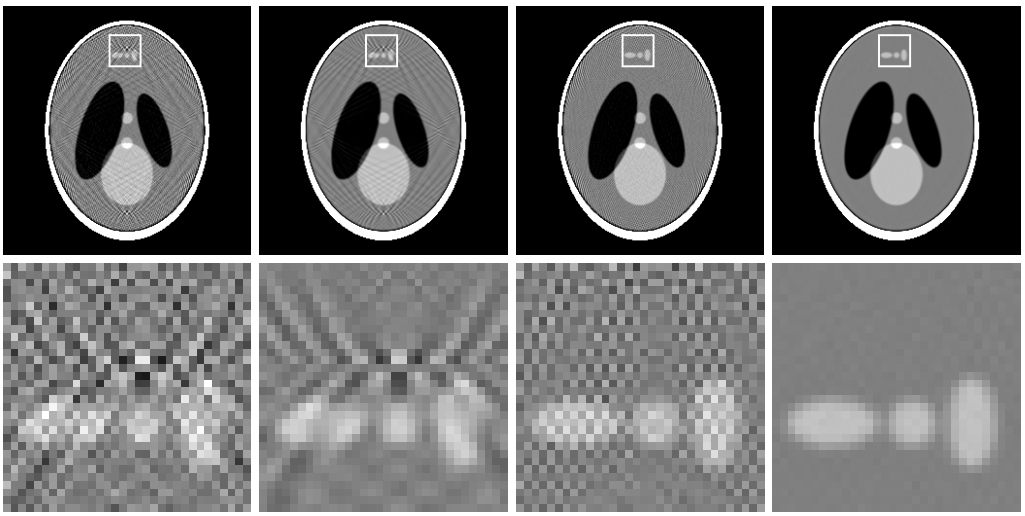

(a) (b) (c) (d)

Figure 2.9: Impact on accuracy of a simple supersampling technique parameterized by the number of ray per detector bin, in combination with a straightforward fixed-step line integration method parameterized by the number of integration steps per pixel. When no antialiasing technique is used, the image tend to be grainy (a). Those artifacts can be attenuated by tracing more (five) rays per detector bin (b). However, large streaks and checkerboard pattern artifacts remain because an inaccurate line integration method is used. Using more (five) integration steps per pixel for ray-tracing suppresses those artifacts (c). The reconstructed image can become exceptionally regular when those two key accuracy issues are tackled simultaneously, using both antialiasing and a finer integration step (d). The white square shows the boundaries of close-up views.

used here has been to use brute force supersampling and accurate interpolations. Supersampling appears to be quite effective at suppressing aliasing for iterative reconstruction in CT. This technique is also often used for image rendering as illustrated in the work of Cook (1986) on stochastic sampling in computer graphics.

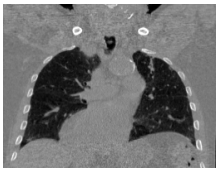

3

Linear Interpolation in Computed Tomography

Linear image interpolation is ubiquitous for image reconstruction in computed tomography (CT). For instance, the backprojection step of reconstruction algorithms is traditionally implemented with the simple *bilinear interpolation* model: a convolution with a pyramidal kernel. This model is approximate but offers a good trade-off between *speed* and *accuracy*. Furthermore the implementation is natural and available on hardware graphics processing units (GPU).

Approximation theory says that the image blurring induced by the triangular interpolation kernel can be compensated by enhancing the image with an all-pole recursive filter before resampling. This study shows that the experimentally optimal pole differs from the one derived by theoretical approaches and that *optimal prefiltering* leads to significant image quality improvement in term of signal to noise ratio (SNR). In fact, optimal pre-filtered linear interpolation outperforms the higher order cubic B-spline interpolation for image reconstruction in CT.

This work has been presented at the 2nd Workshop on High Performance Image Reconstruction (HPIR) onrganized on the September 5 of 2009 in Beijing, China (Schretter *et al.*, 2009c).

3.1 Introduction

Linear image interpolations are widely used in the field of computed tomography (CT). Bilinear interpolation is traditionally used during backprojections (Horbelt *et al.*, 2002) when fetching the value of filtered line integrals for filtered-backprojection (FBP) tomographic reconstruction algorithms. Trilinear interpolation is often used in conjunction with a numerical integrator for computing forward projections through digital volumetric images.

Linear interpolation from point samples relies on a compact triangle signal reconstruction kernel that is only a very crude approximation of the theoretically exact sinc kernel. Nevertheless, the computational performances, the ease of implementation, the implicit handling of image borders and the fair accuracy of the interpolated values made the uncontested popularity of linear interpolation schemes.

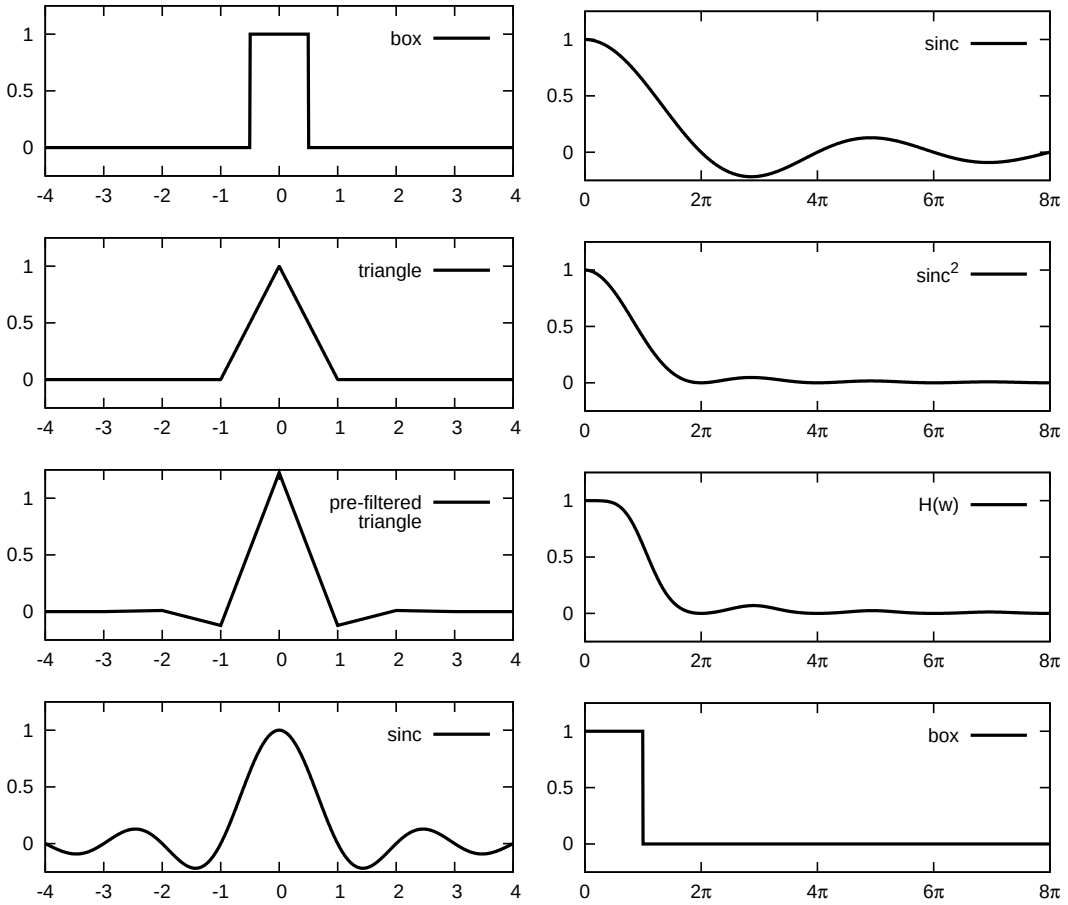

(a) Spatial domain (b) Frequency domain

Figure 3.1: Spatial (a) and frequency (b) responses of various interpolation kernels. The frequency response is expressed as a fraction of the sampling frequency. The goal of pre-filtered triangle interpolation is to compensate smoothing in the pass-band while ensuring simultaneously an effective suppression of aliasing. Note that the support of the sinc kernel is infinite.

Furthermore, linear interpolations are implemented in hardware in graphical processing units (GPU) that are used to accelerate the backprojection and forward projection operations (Zeng and Gullberg, 2000). Those two algorithms are ubiquitous in CT and are also the main bottleneck in both analytical and iterative tomographic image reconstruction algorithms. The impact of several image interpolation methods on the accuracy of forward projections has been evaluated by Xu and Mueller (2006).

Still today, the image interpolation problem for digital images motivates numerous research works, but a wide collection of techniques has been proposed in the literature. Traditional image interpolation approaches (Lehmann *et al.*, 1999) do not consider the possibility to filter the image before resampling. However it has been shown a long time ago that optimal accuracy can be obtained for signal reconstruction by using a pair of optimized pre-filter and reconstruction post-filter (Malvar and Staelin, 1988). A generalized sampling theory that does not assume

band-limited signals justifies this approach (Unser, 1999, 2000). Very accurate image interpolation methods have been reported for medical images (Thévenaz *et al.*, 2000; Blu *et al.*, 2004).

Recently, approximation instead of interpolation has been considered in the image processing community. In particular, quasi-interpolation with infinite impulse response (IIR) filter (Condat *et al.*, 2005) and least-square approximation with finite impulse response (FIR) filter (Price and Hayes, 1998; Dalai *et al.*, 2005) have been proposed independently. The aim of the present work is to demonstrate the potential of modern interpolation and approximation schemes for more accurate tomographic image reconstruction in CT.

The remainder of this chapter is structured as follows. Traditional image interpolation and modern image approximation methods are presented in section 3.2. Section 3.3 shows the benefit of a simple image approximation scheme implemented by a pre-filtering step before linear interpolation for tomographic image reconstruction. Finally, conclusions are drawn in section 3.4.

3.2 Interpolation and Approximation

This section introduces the classical interpolation and approximation problems of the reconstruction of a continuous time-varying signal from uniformly distributed point samples. For interpolation, the reconstructed continuous signal is required to match exactly the sampled values at the sampling point locations. For approximation, this constraint is not required and this unveils possible improvements over interpolation. In this section, the term "reconstruction" refers to the reconstruction of a continuous signal from point samples.

The spatial impulse and the frequency response of classical interpolation kernels are compared in figure 3.1 along with the pre-filtered linear interpolation model investigated in this work. One can remark that the frequency response of the box kernel is superior to the triangle kernel in the pass band $w \in [-\pi, \pi]$. This translates into sharper interpolated images. However, the large ripples outside the pass band translate in very strong aliasing artifacts.

The recovery of high frequency components in the pass band is always underestimated with the triangle kernel and this causes blurring artifacts. Unfortunately, interpolation with the theoretically optimal sinc kernel (last row in figure 3.1) is impractical since the support of the spatial impulse function is infinite. Pre-filtering the signal before linear interpolation (third row in figure 3.1) allows a trade-off between blurring and aliasing artifacts but does not ensure the interpolation property.

3.2.1 Interpolation

Let a sequence of $N \geq 2$ point samples $s(k)$, $k \in [1, N]$, being sampled from a continuous function $f(t)$, $t \in \mathbb{R}$. If f is band-limited to frequencies $w \in [-\pi, \pi]$ and sampled at the Nyquist rate 2π, then it is well known that an exact reconstruction of the original signal is possible between the first and last samples by using sinc

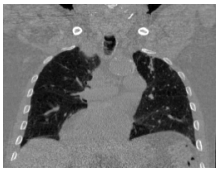

interpolation (Shannon, 1949; Cover and Thomas, 1991) such that

$$f(t) = \sum_{k=1}^{N} s(k) \operatorname{sinc}(t-k), \tag{3.1}$$

Since the sinc kernel has infinite support, exact interpolation requires to convolve each sample with the kernel. While feasible if the support of the image is finite, the very large computational cost of convolutions is often impractical. Furthermore, to prevent loss of information, interpolated values have to be computed and stored also for the infinity of samples lying outside the image boundaries.

Instead, the reconstruction of a continuous function $\tilde{f}$ close to the original signal f can be computed effectively by piecewise linear interpolation from s such that

$$\tilde{f}(t) = \sum_{k=1}^{N} s(k) \beta^1(t-k), \tag{3.2}$$

where the reconstruction function $\beta^1(t) = \max(0, 1-|t|)$ is the second order B-spline function also known as triangle kernel. Interpolation with the triangle kernel ensures that the reconstructed signal is continuous. This property is often preferred over the simplest interpolation with a box kernel, also called nearest neighbor interpolation. Unfortunately, the reconstructed image suffers from overall blurring artifacts when using linear interpolations during backprojections.

Modern developments have shown that very accurate interpolation can be implemented effectively by pre-filtering the image before resampling. Unser (2000) recommends to implement image interpolation by the application of a theoretically derived pre-filter followed by convolution with a third order B-spline basis function. The cubic B-spline interpolation model is very popular nowadays and has been evaluated in experiments for comparison purpose.

3.2.2 Approximation

Traditional interpolation ensures that the reconstructed signal $\tilde{f}(t)$ equals the original signal f at the sampling points, hence when $t = \lfloor t \rfloor$. When this constraint is not a requirement, approximation schemes instead of interpolation have the potential for better reconstructions. Approximation for image resampling has been initially proposed by Mitchell and Netravali (1988) and Blinn (1989a) to find a qualitatively good visual compromise between blurring, aliasing, and ringing artifacts.

Although the derivations are different, the independent works of Condat *et al.* (2005) and Dalai *et al.* (2005) have shown that a least-square approximation of the continuous function can be implemented by pre-filtering the signal prior to interpolation with the simple triangle kernel. Their derivations assume that the continuous function is the cubic B-spline interpolation from the known samples. However, it is likely that the true underlying function is not a linear combination of B-spline basis functions. In this case, better approximation can be obtained as demonstrated in experiments.

When considering the triangle kernel as reconstruction post-filter, a general for-

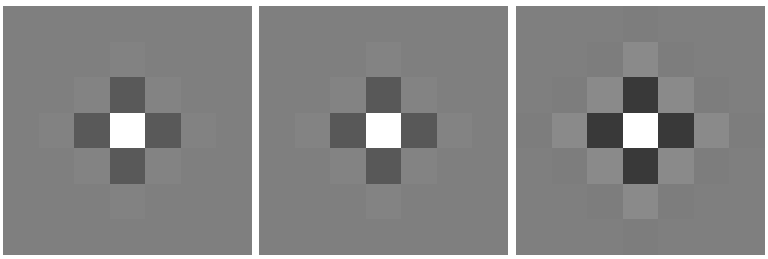

(a) Dalai (b) Condat (b) Optimal (-0.15)

Figure 3.2: Point spread function (PSF) of the FIR pre-filter of Marco Dalai (a), the IIR pre-filter of Laurent Condat (b) and the experimentally optimal pre-filter (c). Gray corresponds to zero, darker values are negative and brighter values are positive. The PSFs of (a) and (b) look very similar, however, the support of the FIR kernel (a) is compact.

mulation of approximate reconstruction can be written as

$$\hat{f}(t) = \sum_{k=1}^{N} \hat{s}(k)\, \beta^1(t-k), \tag{3.3}$$

where the coefficients $\hat{s}(k)$ have to be computed from the original point samples $s(k)$ by filtering them with a symmetric pre-filter kernel φ such that

$$\hat{s}(k) = [s * \varphi](k). \tag{3.4}$$

3.2.3 IIR and FIR Pre-Filters

Condat proposes an infinite impulse response (IIR) implementation with a simple all-pole recursive filter while Dalai proposes a finite impulse response (FIR) implementation of the pre-filter by discrete convolution. From the derivation of Condat, the negative pole for implementing the convolution with a simple IIR recursive filter is $2\sqrt{6}-5$. The Fourier transform of the pre-filter can be extracted from the pole:

$$W_{\mathrm{IIR}}(w) = \frac{6}{5+\cos(2\pi w)}. \tag{3.5}$$

The equivalent discrete convolution implemented by FIR filtering is computed by Dalai as follows:

$$\hat{s}(k) = \frac{49}{40}s_0 - \frac{11}{90}s_1 + \frac{7}{720}s_2, \tag{3.6}$$

with $s_0 = s(k)$, $s_1 = s(k-1)+s(k+1)$ and $s_2 = s(k-2)+s(k+2)$. The support is arbitrarily limited to five samples. However, a larger support of seven samples have not shown any significant improvement in terms of image quality. From the coefficients of the FIR kernel, the Fourier transform of the pre-filter can be extracted:

$$W_{\mathrm{FIR}}(w) = \frac{49}{40} - \frac{11}{45}\cos(2\pi w) + \frac{7}{360}\cos(4\pi w). \tag{3.7}$$

Despite very different expressions, W_{IIR} and W_{FIR} are surprisingly similar functions. Since convolutions in spatial domain are equivalent to multiplications in

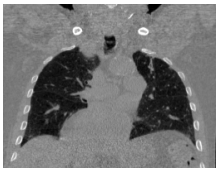

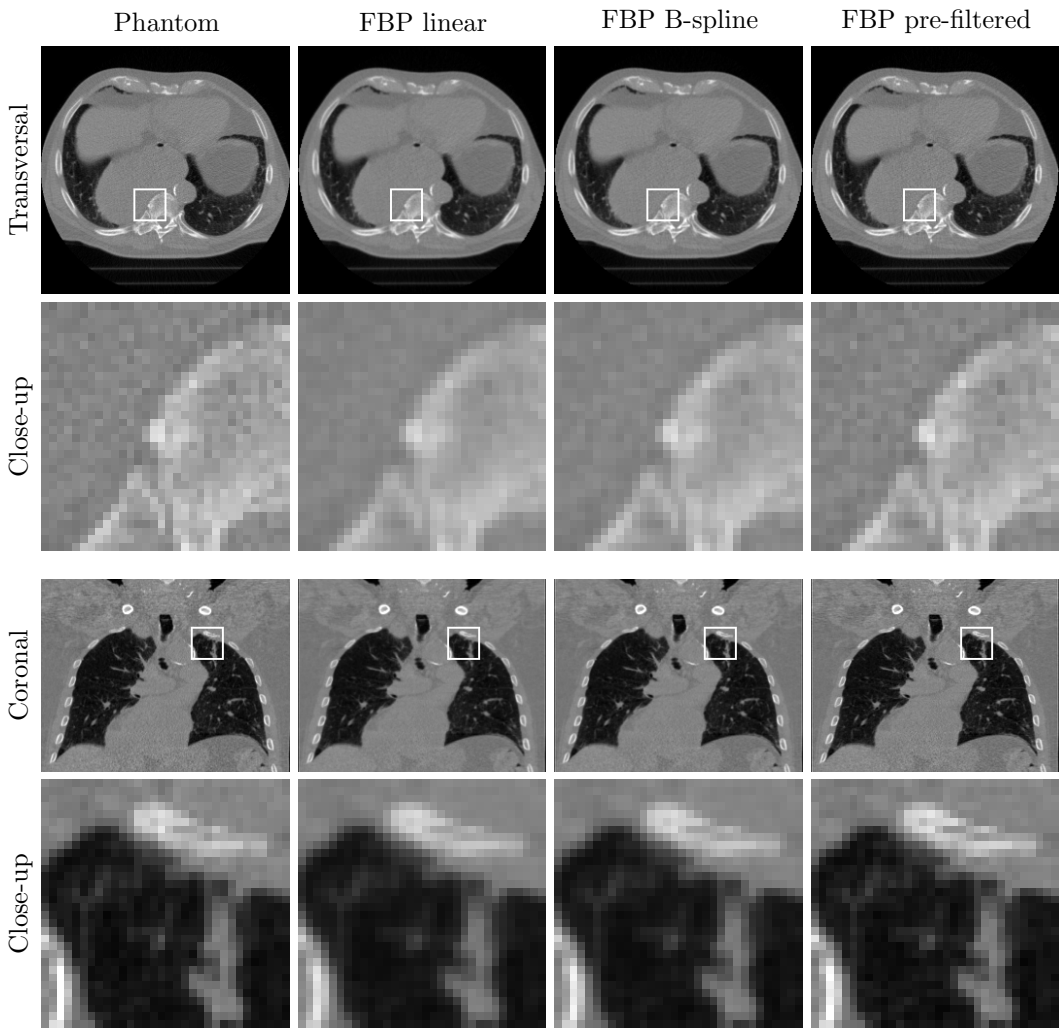

Figure 3.3: Tomographic image reconstructions from 1024 projections, sampled from a voxelized phantom. Results with cubic B-spline, linear and pre-filtered linear interpolations are compared. Linear interpolation during backprojections introduces some blurring in the reconstruction of the phantom image. The white frames mark the borders of close-up views.

frequency domain, the resulting Fourier transform of the pre-filtered linear reconstruction is just

$$H(w) = \operatorname{sinc}^2(w)\, W_{\mathrm{IIR}}(w) \approx \operatorname{sinc}^2(w)\, W_{\mathrm{FIR}}(w)\,. \tag{3.8}$$

This frequency response can be observed in comparison to linear interpolation in figure 3.1. The recovery of frequencies in the pass band is clearly improved at the cost of slight aliasing.

Recursive filtering takes constant time per image element and requires two passes for the causal and anti-causal filtering. While discrete convolutions require more operations per pixel, in practice, in-place convolution with small kernels can be implemented to run as fast as IIR filtering. The choice between IIR and FIR is left to subjective appreciation. For two-dimensional images, the filter is applied

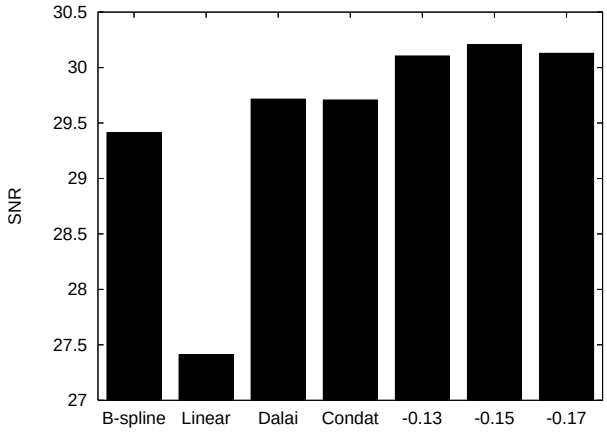

Figure 3.4: Quantitative analyses of image reconstruction in term of signal to noise ratio (SNR) from the original phantom image. Various values of the pole for the pre-filtering have been experimented. The experimentally optimum value of the pole (-0.15) unveils the potential improvement over the theoretical developments using current hypotheses and approximation theory. The FIR filter derived by Dalai gives a very similar result than the IIR filter derived by Condat that uses a pole equals to $2\sqrt{6} - 5 = -0.1010205...$

successively in the vertical and horizontal directions.

The point spread functions of the FIR and IIR implementation of the theoretically optimal pre-filter in least-square sense are compared to the experimentally optimized pre-filter in figure 3.2. Since the support of the IIR filter is infinite, the point spread function (PSF) extends to the whole image. Despite their different intrinsic properties, experiments demonstrate that FIR and IIR implementations yield nearly identical results.

3.3 Results

For experiments, a set of 1024 parallel-beam tomographic projections of 256×198 pixels have been computed from a phantom image of $256 \times 256 \times 198$ isotropic voxels of size equal to 1.36 mm. The goal is to reconstruct the original phantom image from the projection data with the best possible accuracy. The tomographic reconstruction algorithm is FBP and the ideal Ram-Lak ramp filter is used to preserve all frequency content. A large number of projections is used to alleviate possible issues with angular aliasing that typically translates into streak artifacts.

Several image reconstruction results have been compared using various interpolation methods for sampling filtered line integrals in projection space during back-projection. The traditional linear interpolation is compared to cubic B-spline interpolation and several pre-filtered linear interpolation models. The FIR and IIR implementations of the pre-filter for least-square optimal linear approximations give similar results.

A transversal and a coronal slice of reconstructed volumetric images and two selected close-up views are shown in figure 3.3. In those images, gray is set to the attenuation of water and the window width equals 1000 HU such that black corresponds to the attenuation of air. The resolution recovery is much better when

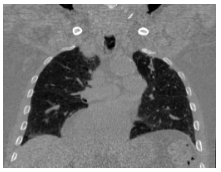

using the cubic B-spline interpolation model in comparison to first order linear interpolations. However, when a suitable pre-filtering is applied before interpolations, linear interpolation have the potential to outperform the more costly cubic B-spline interpolation.

Quantitative analyses conducted in terms of signal to noise ratio (SNR) are presented in figure 3.4. The SNR is a classical metric of the relative image similarity that is conventionally used for assessing the quality of image interpolation procedures. Given a reference image P and a reconstructed image Q defined by N image elements, the SNR is evaluated by

$$\mathrm{SNR}\left(P,Q\right) = -10\log\left(\frac{\sum_{i=1}^{N}\left(P_i - Q_i\right)^2}{\sum_{i=1}^{N} P_i^2}\right). \tag{3.9}$$

3.4 Conclusion

The supplemental work reported in this chapter studied a novel heuristic approach to compensate for the typical blurring that can be observed when reconstructing an image with FBP. In the backprojection step of FBP, linear interpolation is used to fetch filtered line integrals in projection space. This simple interpolation model is exact only if the interpolation points exactly match pixel centers. A simple pre-filtering is used to transform interpolations into approximations and it has been observed that a sharper tomographic reconstruction can be obtained this way.

Linear interpolations are ubiquitous when using GPU implementations for backprojection. Therefore, optimal pre-filtering can improve significantly the accuracy of current image reconstruction codes. For analytic FBP algorithms, the pre-filter is applied in projection space before the backprojection step. For more accurate high-performance computation of line integrals through volumetric images, the pre-filter could be applied in image space before sampling points along integration lines.

4

Image-Based Compensation of Motion Artifacts

Motion blur reconstruction artifacts often arise in computed tomography (CT) when patient's motion introduces *inconsistencies* among projections. Severe reconstruction artifacts have been observed for free-breathing acquisitions. Streaks and doubling of structures can appear and the resolution is limited by strong blurring. To improve image quality, this chapter presents an *iterative method* for compensation of motion artifacts for slowly rotating CT systems.

The rationale of the proposed motion compensation method is to iteratively correct the reconstructed image by first decomposing the perceived motion in *projection space*, then reconstructing the motion artifacts in *image space*, and finally subtracting the artifacts from an initial image. The initial image is reconstructed from the acquired data and might contain motion blur artifacts, but nevertheless, is considered as a reference for estimating the reconstruction artifacts. The originality of the technique stems from the fact that the patient motion is *not* explicitly estimated but the motion artifacts are reconstructed in image space.

This work has been first presented at the SPIE Medical Imaging Conference organized at Lake Buena Vista, USA, on the February 7–12 of 2009 (Schretter *et al.*, 2009a). An extended paper has also been published on this topic in the Medical Physics journal in 2009 (Schretter *et al.*, 2009e).

4.1 Introduction

In contrast to the existing approaches based on pre-correction of the acquired line integrals, this work proposes an iterative motion compensation technique that leaves the input data untouched but aims at correcting the output reconstructed image. The advantage is that the algorithm provides very quickly an early reconstructed image and the image quality of this initial reconstruction progressively improves with each iteration.

The iterative approach presented in this chapter was inspired by the two-pass algorithm for cone-beam reconstruction proposed by Hsieh (1996, 2000) while the principle of motion detection from the difference between line integrals was first proposed by Lin Lin (1994) and studied further by Linney and Gregson (2001).

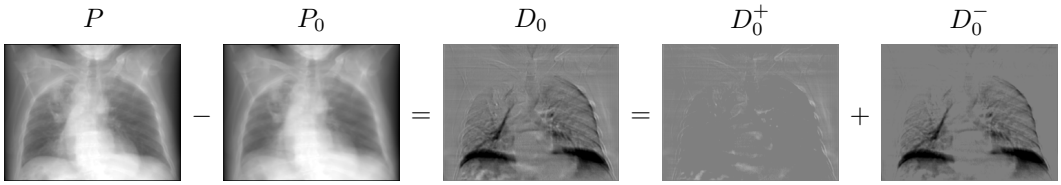

Figure 4.1: Example of decomposition of line integral differences (D_0) between an acquired projection (P) and a reference projection (P_0) computed for the first iteration. Either the positive (D_0^+) or negative (D_0^-) parts of differences (D_0) will be reconstructed to estimate the motion artifacts in image space. The consequences of motion are very apparent at the border of the diaphragm. In (D_0), (D_0^+) and (D_0^-), gray corresponds to zero, while brighter and darker values correspond to negative and positive differences, respectively.

The *instant feedback* feature is crucial for using CT protocols on C-arm systems (Rose *et al.*, 2003) during interventions and is helpful for patient positioning in radiotherapy (Jaffray *et al.*, 2002).

The remainder of this chapter is structured as follows. A novel method based on a pipeline of standard image processing algorithms is proposed in section 4.2 and specific implementation details are discussed in section 4.3. In section 4.4, both qualitative and quantitative figures are shown for experiments based on numerically simulated projections of a sequence of clinical images resulting from a respiratory-gated helical CT acquisition. The border of the diaphragm becomes progressively sharper and the contrast improves for small structures in the lungs. Finally, shortcomings and future work are nailed in section 4.5.

4.2 Method

The iterative nature of the technique exploits the fact that the forward projection is the inverse of the image reconstruction. Therefore, if one samples line integrals through the reconstructed image, then the resulting reference projections should match the acquired projections. However, if the acquired projections are inconsistent because of patient motion, then the reconstructed image will be corrupted by motion artifacts. In this case, sampled reference projections will not match the acquired projections.

The iterative image correction works as follows. First, difference projections are computed by subtracting reference projections from the acquired projections and the differences are decomposed into positive and negative parts. Then, the artifacts are reconstructed in image space from either the positive or the negative part of the decomposition[1]. Finally, the artifacts are subtracted from the initial image, improving its quality.

This work considers parallel-beam geometry for which exact analytical image reconstruction is possible for circular trajectories. The aim is to distinguish the reconstruction artifacts due to patient's motion from the possible cone-beam artifacts that are typically introduced by the approximate FDK reconstruction method

[1]Note that the decomposition of differences is a mandatory step that leads to convergence to a corrected image. If one simply reconstructs the difference projections, the negative errors counterbalance the positive errors and the result is an empty image, filled with zero values.

(Feldkamp *et al.*, 1984). For application in cone-beam geometry, the method can be combined naturally with the related approach of two-pass correction of cone-beam artifacts of Hsieh (2000).

Algorithm

Consider P, the set of projections acquired for a full circular trajectory. The reconstruction from P gives the initial image $I_0 = \text{fbp}(P)$, where $\text{fbp}(\cdot)$ is the filtered-backprojection (Kak and Slaney, 1988; Turbell, 2001) image reconstruction operator. If the projections P are inconsistent, then the reconstructed image I_0 is corrupted by artifacts and the forward projections $P_0 = \text{fp}(I_0)$ do not match the acquired data P. The forward projection operator $\text{fp}(\cdot)$ is the inverse of the image reconstruction operator $\text{fbp}(\cdot)$.

The set of difference projections $D_0 = P - P_0$ is computed and differences are decomposed into a positive part D_0^+ and a negative part D_0^- such that $D_0 = D_0^+ + D_0^-$ and two correction images $C_0^+ = \text{fbp}\left(D_0^+\right)$ and $C_0^- = \text{fbp}\left(D_0^-\right)$ are reconstructed from each part of the decomposition. Figure 4.1 shows the decomposition of the line integral differences for a typical pair of projections.

The images C_0^+ and C_0^- are approximations of the reconstruction artifacts due to, respectively, over- and underestimation of line integrals when reconstructing an image from the acquired data P. The reconstructed artifacts C_0^+ or C_0^- can be subtracted in image space from the initial image I_0, giving the corrected images $I_1^+ = I_0 - C_0^+$ and $I_1^- = I_0 - C_0^-$. Note that even if the decomposed parts of line integral differences are all positive or negative, the reconstructed correction images can contain both positive and negative values.

The correction scheme is iterated, while considering either I_1^+ or I_1^- as initial image and improving the correction by reconstructing and subtracting a new correction image C_1^+or C_1^-. A partially corrected initial image provides a more reliable reference of an artifact-free reconstruction and the estimation of the remaining artifacts will be improved. The two suites of corrected images are $I_{i+1}^+ = I_i - C_i^+$ and $I_{i+1}^- = I_i - C_i^-$, with $i \geq 0$. The method is a generalization of regular image reconstruction algorithms since the initial image is reconstructed from the acquired data without any compensation.

It is interesting to observe that $\text{fbp}(P) = \text{fbp}(P_0) = I_0$, so up to numerical inaccuracies, the two sets of projections P and P_0 reconstruct the very same image, although $P \neq P_0$. Furthermore, P_0 is always a consistent set of reference projections but the acquired projections P are consistent only if the inverse of the reconstruction exactly matches the acquired data, hence if $D_0 = 0$. If the acquired projections P are inconsistent, then $D_0 \neq 0$ but still $\text{fbp}(D_0) = 0$.

4.3 Accuracy Issues

The central idea of the method is that the perceived motion is isolated in projection space by computing the difference between the acquired data and the reference data, sampled from a previously reconstructed image. The differences are decomposed and reconstructed by a standard FBP method. The reconstruction uses the very same geometry as the acquired data to obtain an image that is perfectly registered with

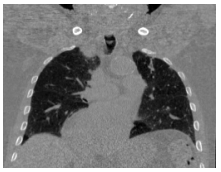

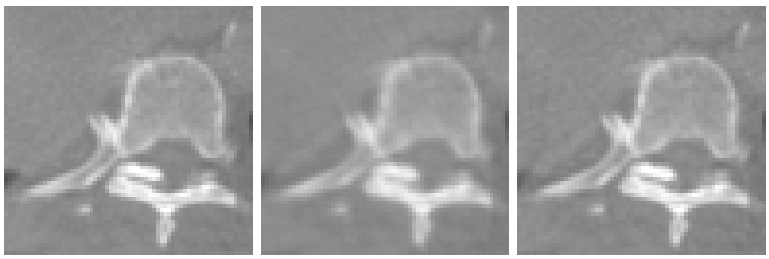

(a) I_0 (b) I_3^- (linear) (c) I_3^- (B-spline)

Figure 4.2: Close-up views showing the spine in a transversal slice of the initial FBP image and two corrected images when using the bilinear or cubic B-spline interpolation models. The spine is a mainly static region and is already sharply reconstructed in the initial FBP image (a). Strong blurring is introduced when using linear interpolation (b) while the sharpness is preserved with cubic B-spline interpolation (c). Image interpolation is used for sampling forward projections from volumetric digital images.

the initial reconstruction. Unfortunately, the accuracy of the reconstructed motion artifacts is limited by two main factors explained below.

First, the forward projection operation that inverses the image reconstruction operation is implemented by sampling line integrals through a digital image and so the accuracy of the line integral calculation depends on the image interpolation method. Inaccurate image interpolation will introduce aliasing and smoothing or ringing artifacts in the correction images (Xu and Mueller, 2006).

Second, the images are reconstructed from a finite number of projections and this inevitably introduces small numerical inaccuracies and streaks in image space. Moreover, the set of the acquired line integrals is not guaranteed to be consistent and so the differences can be inconsistent too. Therefore, large streaks might appear in the reconstruction of the correction image itself.

4.3.1 Cubic B-Spline Interpolation

To improve the accuracy of forward projections, the implementation of image interpolation relies on cubic B-spline interpolation, as suggested by Unser (1999); Thévenaz *et al.* (2000); Unser (2000). This method has been demonstrated to limit significantly both aliasing and smoothing, in comparison to the classical linear and cubic interpolation schemes. The impact on image sharpness when using the higher order cubic B-spline interpolation instead of the simpler linear interpolation during forward projections can be seen in figure 4.2.

Note that it is also possible to improve the accuracy and sharpness of the reconstructed image by using an approximation instead of an interpolation scheme, as explained in the previous chapter. However, the cubic B-spline interpolation model has been prrefered in this work for separation of concerns. Cubic B-splines are a *de facto* standard in the medical imaging community, while approximation schemes based on linear interpolation is a recent idea. Future work could evaluate the performances of the algorithm with an implementation using either interpolation or approximation.

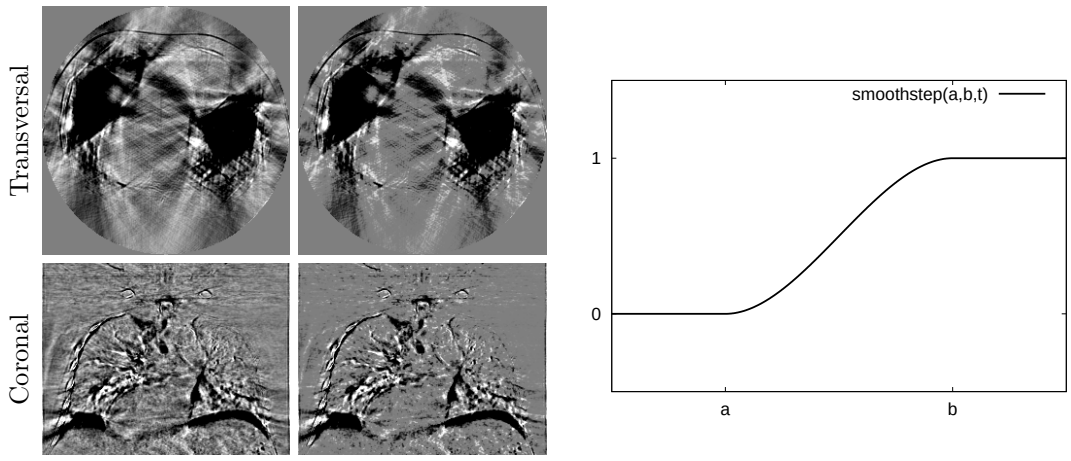

(a) C_0^- (raw) (b) C_0^- (apodized)

Figure 4.3: Impact of the apodization on the correction image C_0^-, computed from the negative part of line integral differences, at the third iteration. The noisy streaks present in the raw reconstructed correction image (a) are removed (b) by the smoothstep function plotted on the right. The smooth apodization prevents the accumulation of numerical errors in the corrected image. The window width of difference images is 100 HU.

4.3.2 Smooth Apodization

In addition, the residual numerical errors are eliminated by smoothly apodizing the reconstructed values that are close to zero in the correction images. This regularization leaves the sharp static parts of the initial image untouched, yielding local correction of reconstruction artifacts. The apodization is implemented by multiplying the values of the correction images with the *smoothstep* function:

$$\text{smoothstep}\,(a,b,t) = \begin{cases} 0 & \text{if } t < a \\ 1 & \text{if } t > b \\ 3x^2 - 2x^3,\ x = (t-a)\,/\,(b-a) & \text{otherwise} \end{cases} \tag{4.1}$$

where $a = 0$ Hounsfield units (HU) and $b = 30$ HU in the experiments and the parameter t is set to the absolute value of image elements.

In fact, the smoothstep function interpolates smoothly between 0 and 1 with a cubic Hermite polynomial. A demonstration of the benefit of the apodization on the quality of a reconstructed correction image can be seen in figure 4.3. The optimal choice for the threshold b can be evaluated experimentally. Indeed, if no motion occurs during acquisition, the forward projections of the reconstructed image should match the acquired projections, hence the differences should be equal to zero in an ideal case.

Unfortunately, the aforementioned differences are usually not equal to zero because in practice, the reconstruction uses a limited number of projections and various discretization as well as numerical errors are transferred to the sampled projections. By measuring the standard deviation of the error distribution, a suitable value for b can be chosen in a principled way (for example, two or three times the mean standard deviation).

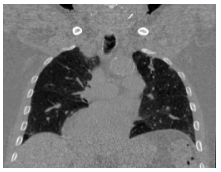

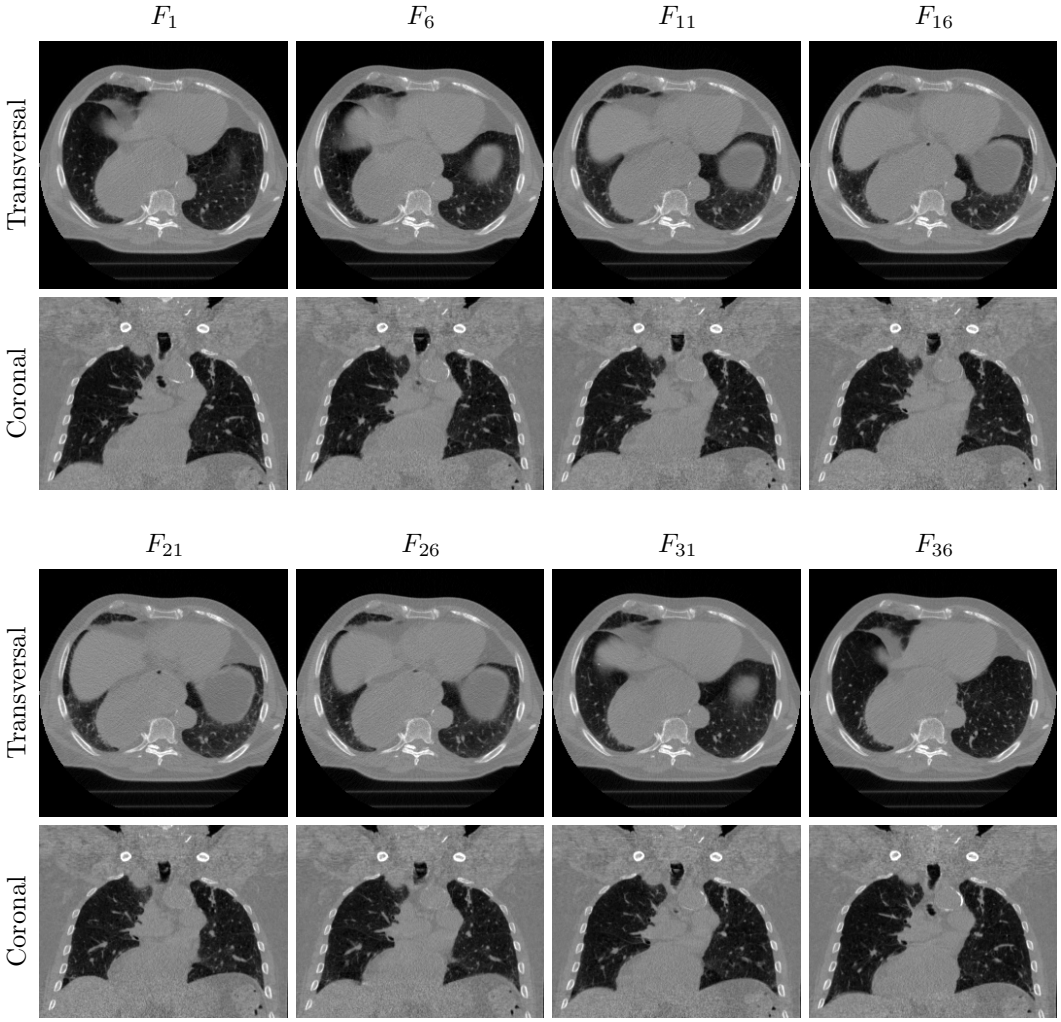

Figure 4.4: Transversal slices number 40 and central coronal views of the selected frames 1, 6, 11, 16, 21, 26, 31 and 36 of a respiratory-gated helical CT acquisition. The study covered an axial length of 27 cm with a FOV of 35 cm. The first four and last four pairs of frames correspond to inhalation and exhalation, respectively. Pulled by contraction of the thoracic diaphragm, organs move out of the selected transversal slice during the inhalation phase.

4.4 Results

To simulate a motion-corrupted acquisition, a set of 1024 parallel-beam projections was numerically simulated from the dynamic free-breathing phantom described in figure 4.4. Experiments consider parallel-beam geometry for which exact analytical image reconstruction is possible for half-circular trajectories but one full rotation with a circular trajectory was considered to simulate a realistic acquisition scenario.

The dataset was obtained from a free breathing patient and consists of a sequence of 40 frames reconstructed from a respiratory-gated helical CT acquisition. The speed of the CT gantry was 0.444 seconds per rotation. The acquisition time was 93.3 seconds during which 26 breathing cycles were observed. Hence, the duration of one breathing cycle was 3.6 seconds on average.

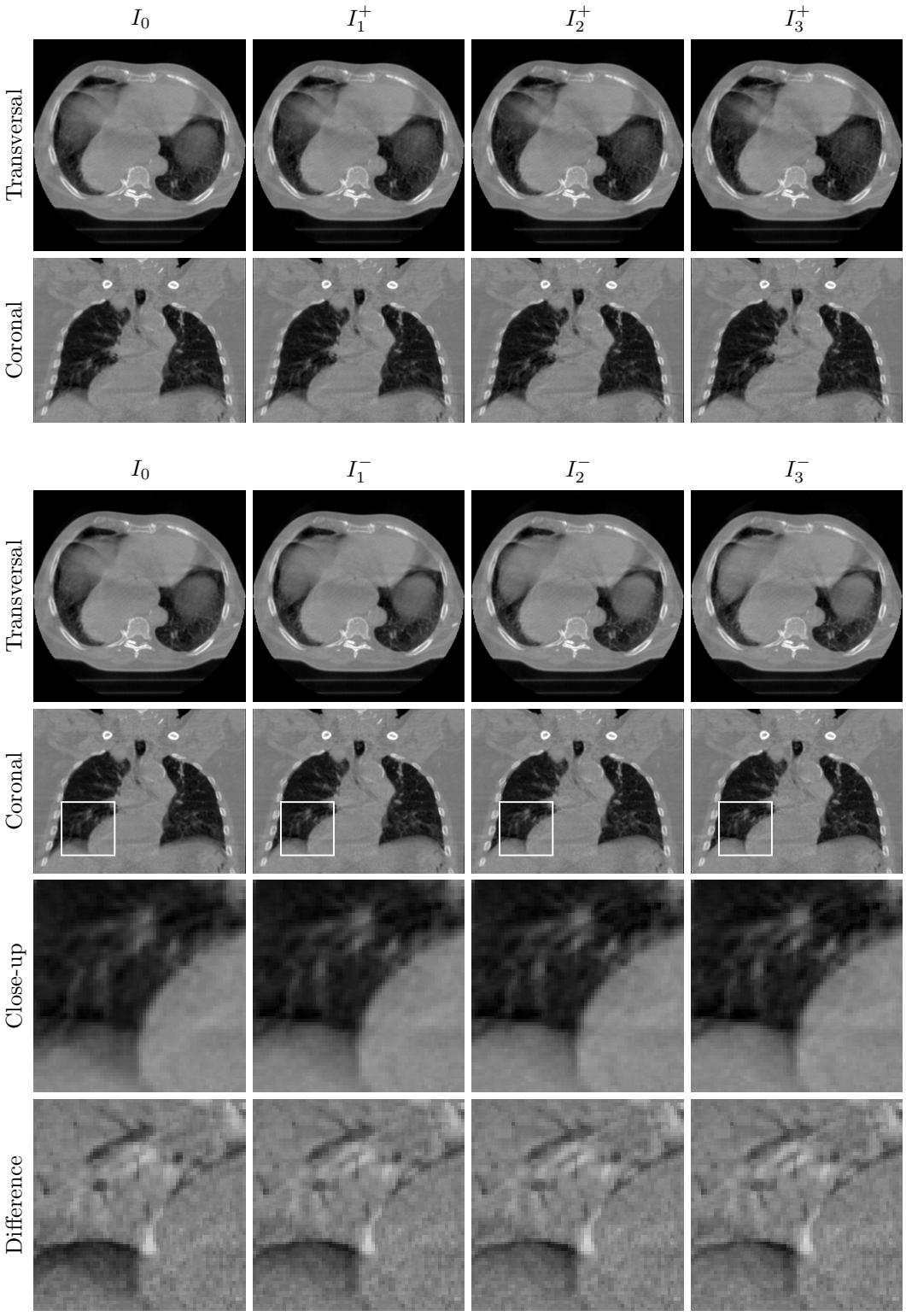

Figure 4.5: Transversal slices number 40 and coronal central views of the initial FBP reconstruction and the corrected images after one, two and three iterations. The white squares show the boundaries of close-up views. The last row emphasizes on the difference with the reference frame 21 from the dynamic phantom. This frame corresponds to the time point in the middle of the respiratory cycle.

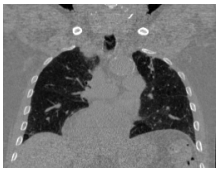

Frame 22/40

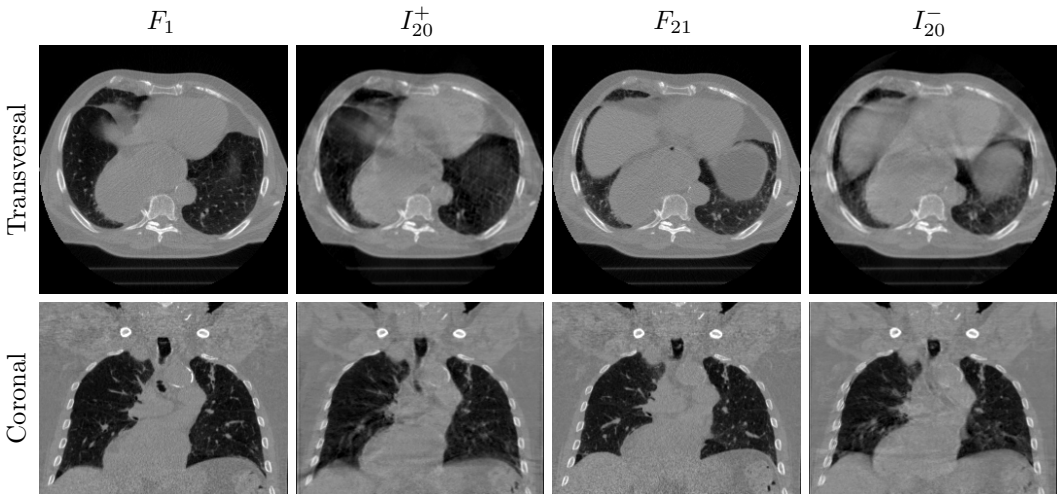

Figure 4.6: Side-by-side comparisons of the two possible image correction scenarios. The corrected images are shown after 20 iterations of the iterative motion compensation framework. As suggested by the analyses in figure 4.8, the images get closer to one of the two extreme motion states: The beginning of exhalation (F_1) when the position of the diaphragm is low or the beginning of inhalation (F_{21}) when the position of the diaphragm is high.

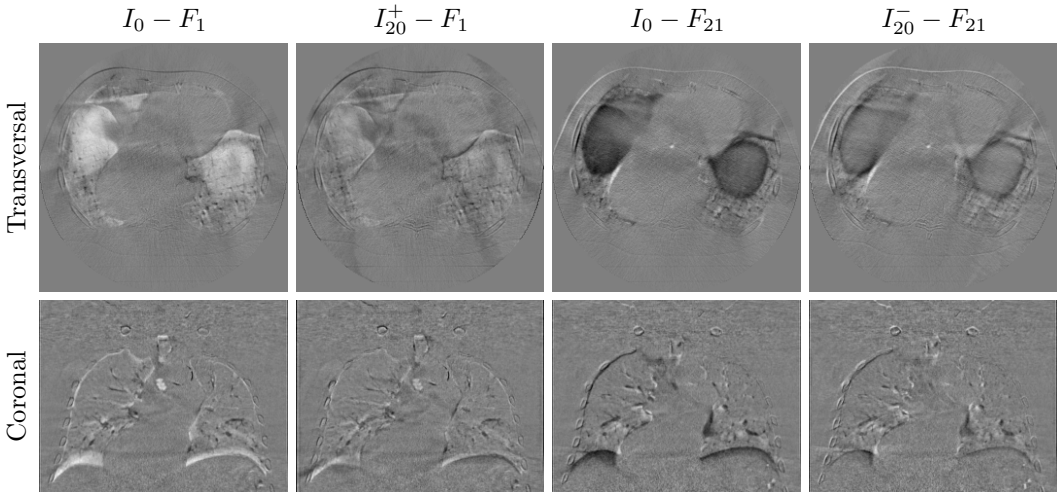

Figure 4.7: Transversal slices number 40 and coronal central views of the two selected frames F_1 and F_{21} of the dynamic phantom compared to the initial FBP image I_0 and the two corrected images I_{20}^{+} and I_{20}^{-} obtained after 20 iterations. F_1 corresponds to the start of exhalation (full inspiration) motion state. F_{21} corresponds to the other extreme start of inhalation (full exhalation) motion state. The differences are significantly reduced with motion compensation.

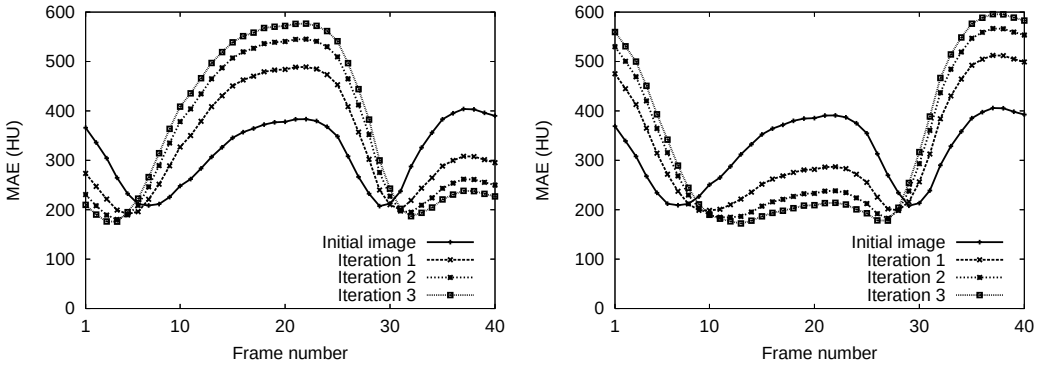

Figure 4.8: Quantitative analyses of images for the initial FBP reconstructed image and corrected images after 1, 2 and 3 iterations when the correction is applied from the positive (left) and negative (right) part of the decomposed differences. The plots show the mean average error (MAE) in Hounsfield units (HU) between the reconstructed image and each of the original 40 gates shown in figure 4.4. The analysis considers only voxels in regions significantly compensated after the first iteration.

At the first frame, the sequence starts at full exhalation, where the diaphragm is low. During the next 20 frames, the inspiration takes place. At frame 21, the maximum inhalation is reached and the expiration begins. One can remark that the images still contain some slight blurring due to helical reconstruction artifacts and residual motion within each gate of the breathing cycle.

The forward projection relies on the approximation of line integrals through the digital image using a fast ray-tracing algorithm (Schretter, 2006). The acquisition time was 12 seconds, matching the typical rotation speed of a C-arm system. This experiment validates the method on a worst case scenario when the patient moves during the whole acquisition instead of holding the breath. Although the simulated breathing motion is naturally periodic, only about 3 cycles can be observed for 12 seconds. Selected transversal and coronal slices from the dynamic phantom are shown in figure 4.4.

Interpretation

The initial FBP reconstruction and the corrected images after one, two, and three iterations are shown in figure 4.5. The strong reconstruction artifacts due to inconsistencies among projections can be seen in the initial FBP images of the first column. Image resolution is mainly limited by motion-blur artifacts. The liver and stomach appear to be semitransparent in the transversal view, as can be seen in the selected close-up views. When using motion correction, the image quality improves progressively with the number of iterations for some of the frames of the dynamic phantom.

It can be observed that in the first two rows of figure 4.5, the corrected image converges towards the motion state at begin-inhale (end-exhale) when correcting with the positive part of differences. In the last two rows, the corrected image converges toward the motion state at end-inhale (begin-exhale) when correcting with the negative part of differences. In all images, the window is centered to

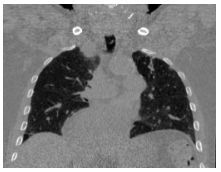

Frame 21/40

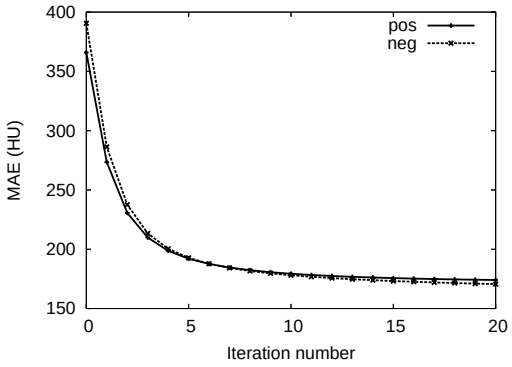

Figure 4.9: Analysis of the convergence toward one specific motion state. The "pos" curve plots the mean absolute error (MAE) in Hounsfield units (HU) between F_1 and the corrected image I_i^+ obtained after iteration $i \in [0, 20]$. The reference frame F_1 corresponds to the motion state at the beginning of exhalation. The "neg" curve plots the MAE between F_{21} and the corrected image I_i^- obtained after iteration $i \in [0, 20]$. The reference frame F_{21} corresponds to the motion state at the beginning of inhalation. In both cases, a reduction of 50% in terms of the mean absolute error can be observed already after the fourth iteration.

the attenuation value of water (0 HU) and the window width equals 2000 HU. In difference images, the window center is set to zero.

One of the two extreme motion states (where the diaphragm is the lower or the highest) is selected as an asymptotic state of the iterative framework. The convergence depends on the choice of the positive or negative part of the difference projections. Indeed, when the diaphragm is low (or high), then the lungs are filled (or empty) and the total mass of the reconstructed image is minimized (or maximized). In figure 4.6, side-by-side comparisons of images obtained after convergence (after 20 iterations) illustrate the end results of the experiment with the two possible image correction scenarios. Image quality improvements can be assessed visually from the difference images in figure 4.7.

Quantitative Analyses

Figure 4.8 shows quantitative analyses of the reconstructed volumetric image. As the number of iterations increases, the algorithm converges to a particular motion state. The mean absolute error (MAE) with respect to frames close to this optimum motion state decreases with the number of iterations.

The plots in figure 4.9 demonstrate the early convergence of the method. After only four iterations, a significant improvement in mean absolute error above 50% can be appreciated. The analyses only consider voxels that belong to a region of interest (ROI) which is the collection of voxels that are significantly compensated after the first iteration. A voxel belongs to the ROI if its absolute value of correction exceeds 100 HU.

4.5 Conclusion

This chapter has presented a novel compensation algorithm for artifacts due to inconsistencies among projections in static tomographic image reconstruction. Per-

formances of the method are assessed for the correction of motion artifacts resulting from a simulated free-breathing acquisition with a slow circular trajectory.

In contrast to existing approaches, the projection data is left untouched and the time-dependent deformation is not explicitly modeled, nor estimated. Instead, the perceived motion is extracted in projection space from the difference between the acquired and the reference projections, sampled from the image reconstructed in a previous iteration step. Then, the artifacts are reconstructed in image space and subtracted from an initial reconstruction.

Data inconsistencies are assumed to be caused by organ motion and the reconstruction of artifacts is progressively refined by the iterative scheme. Since no periodicity of the motion is assumed, the technique could also be applied on breath-hold acquisitions to compensate for unstructured movements such as digestive contractions, breath-hold failures, or nervous shaking.

Since the technique is independent of the specific detector geometry and source trajectory, it can be applied on fan-beam geometry without any change. However, a parallel-beam setup has been preferred because a previous implementation was available and image reconstruction in this simpler geometry suffers less from typical aliasing artifacts that arise in divergent ray geometries.

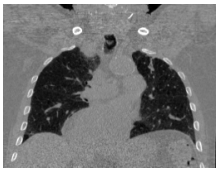

5

Global Motion Correction in 2D Parallel-Beam Geometry

Line integrals contain only a limited part of the information contained in the image that is reconstructed with computed tomography. As a consequence, if patient motion occurs during the acquisition of line integral projections, only a limited part of the motion information will be contained into the data. This observation illustrates *fundamental limitations* of motion perception. As a corollary, only a limited class of deformations which have motion components orthogonal to the direction of line integrals will introduce data inconsistencies and therefore reconstruction artifacts only occurs for movements belonging to this restricted class.

Based on theoretical limitations of motion perception, an alterative approach for motion correction is developed in this chapter. A novel *iterative workflow* is proposed to estimate a dynamic displacement field representing the time-varying position of image elements. An *elastic signal registration* algorithm computes the displacement in projection space from the difference between measured projections and reference projections, sampled from the image reconstructed in previous iterations.

This work has been first presented at the 5$^{\text{th}}$ IEEE International Symposium on Biomedical Imaging (ISBI) organized in Paris, France on the May 14–17 of 2008 (Schretter *et al.*, 2008). First results applying this technique on a realistic clinical dataset has been shown at the 8$^{\text{th}}$ IEEE EMBS International Summer School on Biomedical Imaging held in Berder, France on June 20–28 (Schretter, 2008).

5.1 Introduction

The method presented in this chapter aims at estimating non-periodic motion from tomographic projections for high-quality static low contrast imaging on C-arm systems. In the following, only breath-hold (hence, non-gated) acquisitions are considered, for reconstruction of one single static image in which residual *unstructured* motion is estimated and compensated. Because previous efforts assume periodicity of the motion, the development of a different technical approach was required.

The motion correction problem can be split into two complementary sub-problems: motion estimation and motion compensation. An analytical motion-compensated reconstruction algorithm has already been developed by Roux *et al.* (2004); Desbat

et al. (2006, 2007b). The reconstruction is exact for the class of deformations that preserves some properties of the projection geometry. A solution is proposed for the motion estimation problem in parallel-beam geometry and for a certain class of deformations, including shifting and some local expansions or compressions.

From a new estimate of the displacement field, a better image can be reconstructed by introducing motion compensation in the backprojection step of filtered-backprojection methods. The result of the first iteration is equivalent to a standard reconstruction without motion correction and further iterations progressively sharpen the image. Considering the sampled image as a motionless reference, the motion estimation is *exact* for a certain class of deformations, including shifting, expansion, and compression.

The remainder of this chapter is structured as follows. First, a new iterative motion correction framework is introduced in section 5.2. This solution is motivated by the fundamental limitations of motion perception that are briefly introduced. Their impact on the reconstruction of exact motion in image space is experimented as well. In section 5.3, an original algorithm is derived to compute deformations while assuming the availability of a static reference image. A generalization allows estimating more general motion with a simple elastic signal registration method. Finally, results are shown in section 5.4 for a randomly deformed Shepp-Logan phantom and conclusions are drawn in section 5.5.

5.2 Motion Correction

In 2D tomography, projections are 1D signals and the projection of the displacement of image elements can be described by a smooth strictly increasing bijective mapping function in projection space. The strict increasing property appears because crossing of two integration lines never occurs with *diffeomorphic* deformations (Ashburner, 2007).

Due to relative motion, the angular position of the focus position can vary freely over time, describing a so-called *virtual* source trajectory. In general, the position of the focus point is parameterized by a projection angle and a distance from the detector and all line integrals are measured between a displaced focus point and centers of detector pixels, smoothly displaced on the projection axis. The parallel-beam geometry considered here is a special case in which the focus point is at infinite distance from the projection plane. Therefore, only the projection angle can vary.

If the virtual source trajectory matches the ideal circular path, the exact motion compensation of Desbat *et al.* only involves two slight modifications in the backprojection step of classical filtered backprojection (FBP) algorithms.

First, the integration line joining the center of the current voxel to the focus point is displaced, according to the provided bijective mapping and the line integral value is fetched at the corresponding pixel in the projection image.

Second, the line integral is weighted by a scaling coefficient, preserving the total mass in cases of local expansion or compression movements. The scaling coefficients are proportional to the derivative of the scalar mapping function.

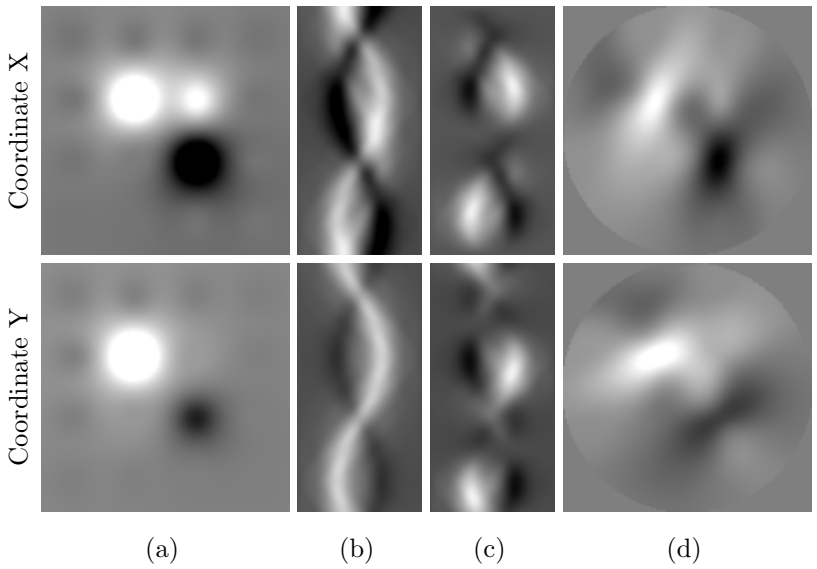

Figure 5.1: Experiment on the fundamental limitations of motion perception from tomographic projections. A 2D smooth vector field has been generated and reconstructed from a sinogram that has been corrupted by removing the vector component aligned with the direction of line integrals. Line integrals through the vector field (a) has been sampled for 256 different angles and the resulting stack of projections is shown in (b). Vector components along the projection direction has been removed from (b) to give the corrupted sinogram (c). The reconstruction from (c) yields the vector field (d) that only convey partial information about the true motion shown in (a). The upper and lower rows show respectively the x and y components of vectors.

5.2.1 Motion Perception

Motion perception involves a combination of the visual and cognitive process, in order to infer the velocity of elements of an observed scene Mather (2006). In the context of three-dimensional imaging with CT, the scene is composed from the collection of image elements (voxels) (Srámek and Kaufman, 1998, 1999) and visual occlusions prevent the external observations of inner structures. The great revolution brought by X-ray imaging is the ability to capture transparent images from opaque objects.

By means of X-ray transmission, it becomes possible to perceive motion inside the body from a sequence of planar X-ray projections. Some motion information is implicitly present in the image sequence but fundamental limitations to perception exist. In particular, the motion component in the direction of the projection can not be measured since line integrals are invariant to motion along their integration paths. This phenomenon is related to the insufficient motion cue for the inference of depth in monocular vision and the impact on tomographic image reconstruction is illustrated in figure 5.1.

The fundamental limitations of motion perception prevent external observers to define the exact trajectories of image elements and therefore discourage any hope to achieve exact reconstruction of the motion information. This fact motivated the choice to estimate only the motion information that can be captured in projection space. Fortunatelly, only a partial knowledge of the true motion is sufficient to

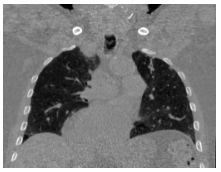

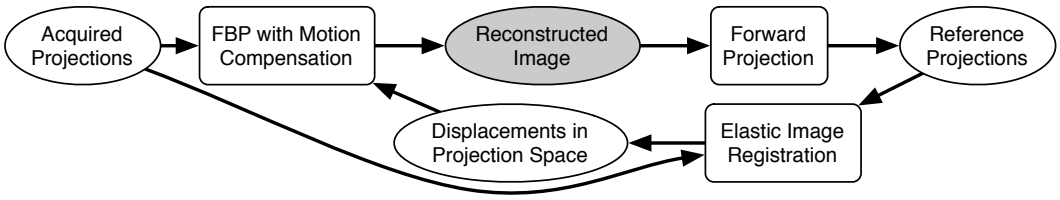

Figure 5.2: Iterative workflow for motion estimation and compensation. Box shapes represent algorithms, transforming input data to generate new outputs. Data are represented by oval shapes. The current reconstructed image shown in gray is considered as a reference static image. Then, the motion is estimated with elastic image registration. Finally, the image is reconstructed again with motion compensation.

acheive high-quality motion compensated image reconstruction in CT.

5.2.2 Framework

The iterative motion correction workflow, outlined in figure 5.2, proposes a solution to estimate the mapping function. Data is represented by ovals and boxes symbolize algorithms. For each iteration, an *attenuation image* is reconstructed from the *measured projections* using a *FBP reconstruction with compensation*. Then, *reference projections* are sampled by computing the forward projection through the attenuation image reconstructed so far. The measured projections are mapped on the reference projections by an *elastic registration* algorithm. The resulting warping is a new *estimate of displacement in projection space* that can be used by the motion-compensated FBP algorithm to produce a new corrected image.

The first reconstruction assumes no motion and the resulting image contains artifacts, but may nevertheless be considered as a motionless reference for the second iteration. Since these reference projections are sampled from a static image, they are consistent. Therefore, the registration algorithm will provide a displacement field in projection space that compensates for inconsistencies when reconstructing an image from measured projections.

The design of the method takes into account the fundamental limitations of motion perception. Due to the aperture problem, only one of the two components of motion can be perceived. Hence the motion estimation stage produces displacement vectors, orthogonal to the projection directions by registration of measured projections to reference projections. The motion estimation step works on independent pairs of corresponding projections. Therefore, the algorithm suits naturally for trivial parallelization.

5.3 Motion Estimation

Let's assume the availability of a motionless image from which reference projections can be sampled. The considered motion estimation problem is to extract the displacement of pixels in projection space from corresponding measured and reference projections. The motion is computed independently for each pair of projections.

A static 2D image is commonly represented by a Cartesian grid of point samples, located at centers of identical image elements: usually, non-overlapping square pixels.

It is easy to extend this image model to represent motion by associating, for each pixel, a description of its displacement over time from the initial grid position. In a similar way the space is discretized by the grid, the displacement of pixels can be sampled at several time frames. In this chapter, one time frame is associated with each projection.

5.3.1 Radon Transform

Let $f(x, y, t) \to \mathbb{R}$ be a dynamic 2D image where $(x, y) \in \mathbb{R}^2$ are spatial Cartesian coordinates and $t \in [0, 1)$ is the normalized temporal position. The function f is positive and compactly supported in a normalized circular field of view such that $f(x, y, t) = 0$ when $x^2 + y^2 > 1$. Moreover, the total mass M must be preserved:

$$M = \int_{-1}^{1} \int_{-1}^{1} f(x, y, t)\, dxdy, \quad \forall t. \tag{5.1}$$

A line integral $p(\phi, s, t) \to \mathbb{R}$ from f is parameterized by an angular coefficient $\phi \in [0, \pi)$ and a signed distance from the origin $s \in [-1, 1]$ and is defined by

$$p(\phi, s, t) = \int_{-l}^{l} f(s\cos\phi + u\sin\phi, s\sin\phi - u\cos\phi, t)\, du, \tag{5.2}$$

with $l = \sqrt{1 - s^2}$, the half-length of the intersection between the line and the field of view. The point of intersection between the line and the virtual detector is $(s\cos\phi, s\sin\phi)$ and the normalized direction vector of the integration line is $(\sin\phi, -\cos\phi)$.

The Radon transform of f is the collection of all time-varying line integrals intersecting the field of view. The Radon transform provides sufficient data to reconstruct exactly the dynamic image f at any position in space and time. However, most CT tomographs are only able to measure line integrals along one projection direction at a time. To model this limitation, the projection angle ϕ is assumed to be linearly dependent on the acquisition time t. Therefore, $\phi = \pi t$ such that one half circular rotation is achieved when $t = 1$. In the following, the Radon transform is defined as the measured projections

$$(Rf)(\phi, s) = p\left(\phi, s, \frac{\phi}{\pi}\right), \tag{5.3}$$

and this collection of line integrals may be inconsistent since each projection observes f at a potentially different deformation state.

5.3.2 Shifting Motion

The *translation invariance* property of the Radon transform states that translation in the image domain results in shifted projections. This important property and its relation to image motion have been studied further by Milanfar (1999). An image displaced by the translation vector (d_x, d_y) is noted

$$f_d(x, y, t) = f(x + d_x, y + d_y, t), \tag{5.4}$$

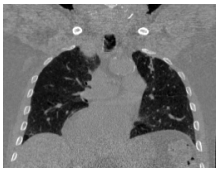

Frame 18/40

and its Radon transform is obtained by translating each projection:

$$(Rf_d)(\phi, s) = (Rf)(\phi, s + d_x \cos\phi + d_y \sin\phi). \tag{5.5}$$

Therefore, analytical estimation of shifting motion is straightforward by computing a feature point that depends on global translation in both the measured projection and the reference projection. For instance, the center of mass

$$\mu(f, \phi) = \frac{1}{M} \int_{-1}^{1} s\ (Rf)(\phi, s)\, ds \tag{5.6}$$

can be computed in projection space from the weighted mean of pixel positions on the virtual detector axis. The difference between center of masses in corresponding measured and reference projections yields a signed shifting displacement.

5.3.3 Scaling Motion

Given the *scaling invariance* and the *linearity* properties of the Radon transform, global expansion or compression in the image domain result on respectively broader or narrower spreads in projection space, while preserving the total mass. An image scaled non-uniformly along the horizontal and vertical axis by the respective factors $s_x > 0$ and $s_y > 0$, and preserving the total mass is noted

$$f_s(x, y, t) = \frac{1}{s_x s_y} f\left(\frac{x}{s_x}, \frac{y}{s_y}, t\right), \tag{5.7}$$

and its Radon transform is obtained by weighting each projection, translated toward or away from the origin:

$$(Rf_s)(\phi, s) = \frac{1}{\alpha} (Rf)(\phi, s\alpha), \tag{5.8}$$

where $\alpha = \sqrt{(s_x \cos\phi)^2 + (s_y \sin\phi)^2}$.

Therefore, analytical estimation of global expansion and compression deformations is also straightforward by computing a value that depends on the scale of corresponding projections. For instance, the standard deviation from the center of mass

$$\sigma(f, \phi) = \sqrt{\frac{1}{M} \int_{-1}^{1} (s - \mu(f, \phi))^2 (Rf)(\phi, s)\, ds} \tag{5.9}$$

can be computed for both measured and reference projections. The ratio of the former on the later yields the scaling factor.

5.3.4 Shifting and Scaling Motion

As explained above, analytical extraction of motion in projection space is trivial for cases such as shifting and global expansion or compression. The center of mass can be computed in projection space from the weighted mean of pixel positions, in both measured and reference projections. Their difference gives the projection of

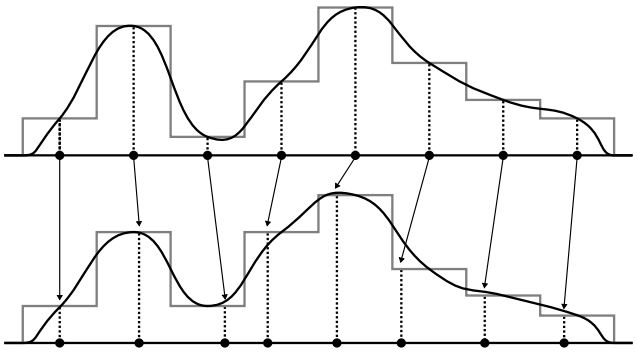

Figure 5.3: Elastic signal registration for the computation of a bijective mapping function that minimizes the difference between partial integrals. The center of each pixel is displaced by a simple numerical integration method. The solution has unambiguous closed form and therefore the registration algorithm is fast and straightforward to implement.

the shifting displacement and the ratio of standard deviations gives the object scale, as perceived from the projection.

Given the number of bins in a discretized projection N, the cumulative sum of bins is invariant in respect to the projection angle and is equal to M. Also, the point located at the center of mass splits the signal in two parts of equal partial integrals. Generalizing this observation, any particular point

$$p_i = \frac{2i - N - 1}{N}, \quad i \in [1 \dots N] \tag{5.10}$$

of a projection splits the signal in two regions determined by the values of their partial integrals. Systematic computation of the correspondence between centers of pixels defines a discrete bijective mapping function that provides a registration between two discrete signals.

5.3.5 Elastic Signal Registration

As shown in figure 5.3, the center of every pixels p_i of the source signal is mapped on sub-pixel accurate locations $q_i \in [-1, 1]$ on the target signal, such that partial integrals are preserved:

$$\int_{-1}^{p_i} (Rf)(\phi, s)\, ds = \int_{-1}^{q_i} (Rf_{ref})(\phi, s)\, ds, \tag{5.11}$$

where f_{ref} is the motionless reference image. One can remark that $q_i \leq q_j, \forall i < j$ is an invariant of the former relation, ensuring that the computed discrete function is a strictly increasing bijective mapping. Offsets between corresponding pixels are displacements in projection space.

This elastic signal registration procedure can be implemented by a simple numerical integration method that marches through sub-pixel locations in the target signal to find the correspondence with the centers of pixels from the source signal. Two corresponding points share identical value for their left and right partial integrals. Elastic image registration algorithms minimize, usually iteratively, an image

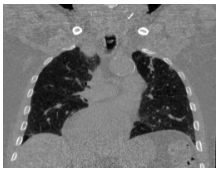

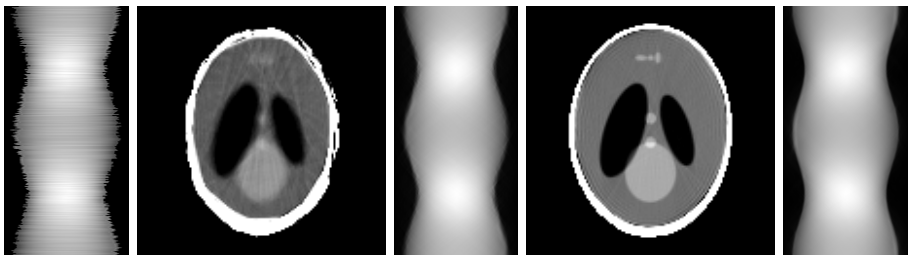

(a) (b) (c) (d) (e)

Figure 5.4: Reconstructions from measured projections (a) of a randomly shifted and compressed phantom are shown after the first (b) and second (d) iteration. The projections (a) are inconsistent and regular FBP reconstruction leads to a motion-corrupted image (b). Forward projections from (b) give the reference projections (c). A displacement field is estimated in projection space (result shown in figure 5.5) by elastic registration of measured projections (a) to reference projections (c). Using the displacement for a motion-compensated FBP reconstruction from original projections (a) yields the motion corrected image (d) from which more accurate reference projections (e) can be sampled.

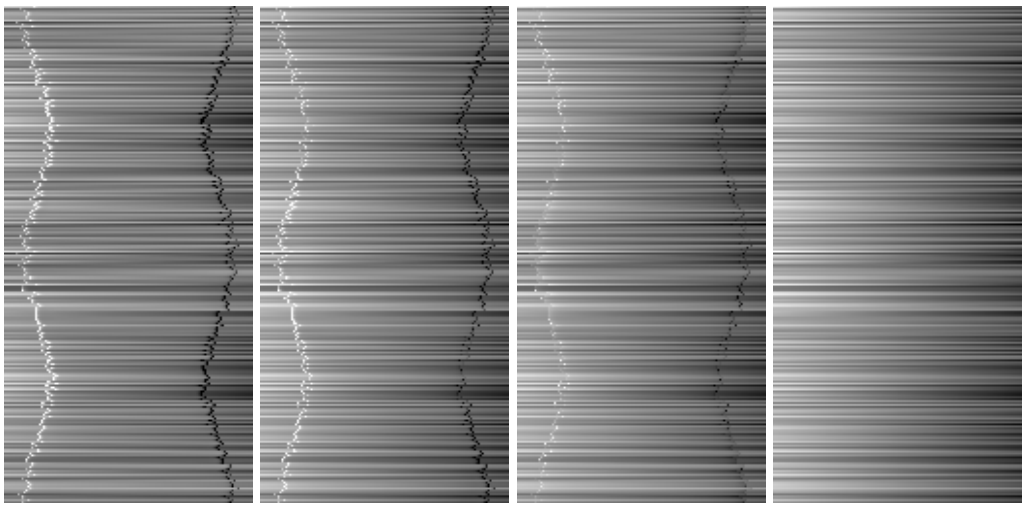

(a) (b) (c) (d)

Figure 5.5: Motion pattern images iteratively estimated by direct elastic signal registration. Images show the estimates of displacements in projection space after the first (a), second (b), and third (c) iteration. The last pattern (d) is the ground truth, shown for comparison purpose.

dissimilarity metric. In this case, the dissimilarity is the difference between partial integrals in the source and target signals and the solution is not iterative.

5.4 Results

Results from an experiment with the low-contrast Shepp-Logan phantom are shown in figure 5.4 and figure 5.5, for random shifting and non-uniform global compression motion. Measured data has been simulated for a full rotational acquisition in parallel-beam geometry.

Figure 5.4 shows the projections and reconstructed images for the first steps within the iterative motion correction technique explained in Fig 5.2. Images of 128×128 pixels are reconstructedf rom 256 projections of 128 pixels each. The images are shown with 2×2 magnification of pixels size. An efficient correction for the inconsistencies of input projections is already observed after the second iteration.

Figure 5.5 shows the estimated displacement of pixels in projection space for successive iterations. Bright and dark pixels correspond to positive and negative offsets, respectively. Residual errors decrease with increasing iteration number and are mainly located at the edge of the object, at the border between high and low attenuation regions. Each row is filled with a gradient: from bright to dark for compressions and from dark to bright for expansions. A constant negative or positive bias contains the global shifting information. There is no correlation between rows because the deformations are generated randomly over time. More complicated motion could yield complex non-linear variations along the horizontal axis.

5.5 Conclusion

This chapter introduces a general methodology for motion estimation and compensation in tomography. In particular, a solution is provided to estimate the motion information for the class of deformations that can be described by a strictly increasing bijective mapping function in projection space. Tackling these specific deformations is inspired by the complementary work of Desbat *et al.*, showing that exact reconstruction from inconsistent projections and a motion description, is still possible for this class of deformations.

The extraction of the motion information is based on numerical integration, without using any prior knowledge about the temporal or spatial smoothness of the underlying displacement field. This is a simple non-iterative elastic signal registration procedure that can be computed in a single pass over the input data. The proposed iterative motion correction framework can be seen as a generalization of a conventional FBP image reconstruction. Indeed, if no motion corrupts the projections, the process converges in one iteration and reduces to a standard image reconstruction.

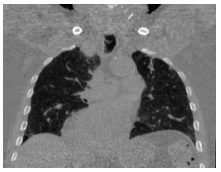

6

Local Motion Correction in 3D Parallel-Beam Geometry

This chapter extends the technique described previously and presents a new iterative motion correction technique composed of *motion estimation* in projection space, *motion segmentation* in image space and *motion compensation* within an analytical filtered-backprojection (FBP) image reconstruction algorithm. The motion is estimated by elastic registration of acquired projections on reference projections, sampled from the image reconstructed in a previous iteration step. To apply the motion compensation *locally*, the image regions significantly affected by motion are also segmented.

First the perceived motion is identified in projection space by computing the absolute difference between *acquired* line integrals and *reference* line integrals. Then, differences are reconstructed in image space and the image is regularized with a pipeline of standard image processing operators. The result of the segmentation is a normalized *motion map*, associating each image element with an estimate of the relative amplitude of the detected motion. The estimated displacement vectors in projection space and the reconstructed motion map in image space are then used by an adaptive motion-compensated FBP algorithm to reconstruct a sharper image.

This work has been presented at the SPIE Medical Imaging Conference organized at Lake Buena Vista, USA, on the February 7–12 of 2009 (Schretter *et al.*, 2009b).

6.1 Introduction

The estimation of organ motion from X-ray projections is an ill-posed problem by nature. Since the projections are two-dimensional while the image space is three-dimensional, the system is undetermined if one wants to extract the 4D information of motion along time given the 3D information of projections acquired from a dynamic object (Grangeat *et al.*, 2002; Bonnet *et al.*, 2003).

It is mandatory to augment the input information to solve the motion estimation problem. Often, the assumption is made that the organ motion is smooth and periodic. Under those hypotheses, gating the projection data with the respiratory signal allows independent reconstructions of each frame of a dynamic sequence of volumetric images (Sonke *et al.*, 2005; Yang *et al.*, 2008). Furthermore, the motion

can be estimated with fair accuracy, by image registration of successive reconstructed volumes Isola *et al.* (2008).

The approach of this work follows the proposal of Roux *et al.* (2004); Desbat *et al.* (2006, 2007b). Desbat assumes that for any given time, the displacement vectors are identical for all points on a same X-ray projection ray and that these vectors are orthogonal to that line. It is easy to see that displacement along projection lines does not modify the value of line integrals (Milanfar, 1999). Hence, the measured intensities are invariant to the orthogonal component of the displacement vectors. Those motion components can not be perceived in X-ray projections and therefore do not yield any data inconsistency (Yu *et al.*, 2006; Yu and Wang, 2007).

Constraining the displacements to be orthogonal to line integrals yields exact image reconstruction algorithms. Therefore, this assumption does not lead to any loss of generality since the reconstruction reduces to a standard filtered-backprojection (FBP) (Kak and Slaney, 1988; Turbell, 2001) if the displacement magnitudes are set to zero. However, it is likely that patient motion will not fulfill the conditions of the admissible class of deformations mentioned above. For instance, an incorrect motion estimate could corrupt the static parts of the image. By introducing the concept of *local motion compensation*, the admissible class of motion is extended in this work to capture also some deformations that bend integration lines into curves in image space.

The rationale of the method presented in this chapter is the combination of an iterative estimation of the perceived patient motion in projection space and a heuristic segmentation of the image region where organ motion is detected. The deformation estimate and the motion segmentation provide additional information that are used by a motion-compensated FBP algorithm to reconstruct a sharp static image from the acquired projection data. This technique has already demonstrated promising results for the estimation of affine motion from projections of a deforming Shepp-Logan phantom (Schretter *et al.*, 2008).

The remainder of this chapter is structured as follows. The extended iterative motion correction method is described in section 6.2 in the context of volumetric image reconstruction. The motion correction problem is split into three complementary sub-problems: motion estimation, motion segmentation and motion compensation. Results are shown qualitatively and quantitatively in section 6.3, for reconstructions from realistic projections simulated from clinical patient data. Since the method does not assume any periodicity of the motion model, it can correct artifacts due to unstructured patient motion, such as breath-hold failure, abdominal contractions, and nervous movements. Finally, conclusions are drawn in section 6.4.

6.2 Method

A novel iterative motion correction technique is proposed and is summarized by the diagram in figure 6.1. Rounded rectangles represent algorithms and oval shapes represent both input data and output results of the algorithms. The motion is estimated in projection space by registration of measured projections on reference projections, sampled from a static image reconstructed in a previous iteration. This step is identical to the method illustrated by figure 5.2 in the precedent chapter.

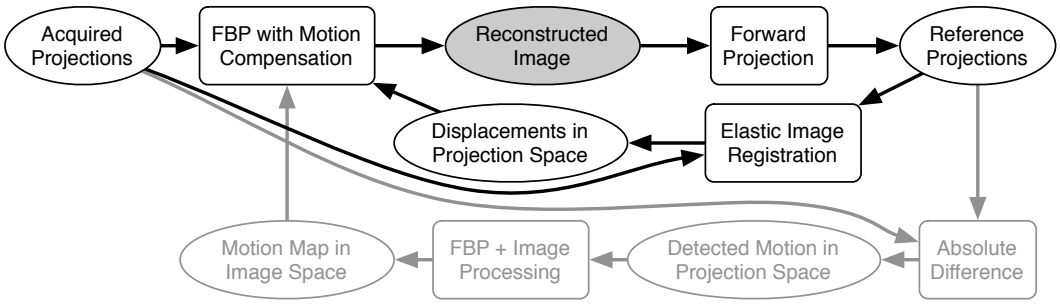

Figure 6.1: Workflow for iterative motion estimation, segmentation, and compensation. First, reference projections are forward-projected from the current reconstructed image. Displacement vectors are estimated in projection space by elastic image registration of acquired projections on reference projections. In parallel, the motion is segmented in image space by reconstructing absolute differences between acquired and reference projections. Finally, the image is reconstructed again with local motion compensation.

An original local motion-compensated image reconstruction scheme is proposed in this chapter by using a *motion map* that segments image regions where organ motion is detected. The motion estimation is shown by the black part of the diagram, while the computation of the motion map is shown by the gray part in figure 6.1. In parallel to the motion estimation steps, the method detects the image regions where patient motion occurred during the acquisition.

The original motion information in projection space is transferred to image space by backprojection and weighted by the result of the new motion segmentation procedure. To detect organ motion, the absolute differences between reference and acquired line integrals are reconstructed with FBP. This reconstructed image provides additional information about the patient motion in image space. The image is regularized and normalized to weight the estimated displacements in projection space, in order to further increase the accuracy of the motion-compensated reconstruction.

The next sections define the notations used through the chapter and present in more details the motion estimation and motion segmentation methods. Furthermore, a novel adaptive motion-compensated FBP reconstruction algorithm is defined. This algorithm is a generalization of FBP, but allows local image correction with the estimated patient motion.

Projection and Backprojection

In parallel-beam geometry, the orthogonal projection operator

$$P_\alpha(x, y, z) = (y\cos\alpha - x\sin\alpha, z) \tag{6.1}$$

maps a point $(x, y, z) \in \mathbb{R}^3$ defined in image space, to a point on the planar detector oriented at angle $\alpha \in [0, 2\pi)$. The adjoint of the orthogonal projection operator

$$P'_\alpha(u, v) = (-u\sin\alpha, u\cos\alpha, v) \tag{6.2}$$

maps a point $(u, v) \in \mathbb{R}^2$ defined in projection space to a point on a *virtual detector*.

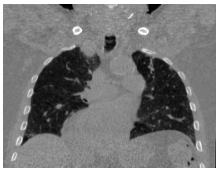

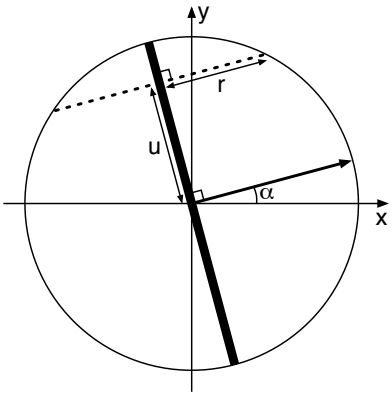

Figure 6.2: Parametrization of line integrals for the parallel-beam geometry. The figure shows geometrical relations in a transversal cross section of the cylindrical field of view bounded by the circle. The thick line segment depicts the cross section of a row of the virtual planar detector, oriented at angle α. The dotted line segment is a specific integration path.

The virtual detector shares the same orientation with the real one, but is centered on the origin of the cylindrical field of view (FOV). Note the invariant relation

$$P_\alpha \left(P'_\alpha \left(u, v \right) \right) = \left(u, v \right), \quad \forall \left(u, v \right) \in \mathbb{R}^2, \tag{6.3}$$

however (6.2) is not the inverse of (6.1) since $P'_\alpha \left(P_\alpha \left(x, y, z \right) \right) = \left(x, y, z \right)$ is true only for points that lie on the virtual detector, thus if $\left(x, y, z \right) \cdot \vec{d}_\alpha = 0$. The normalized vector $\vec{d}_\alpha = \left(\cos \alpha, \sin \alpha, 0 \right)$ is normal to the detector plane.

Radon Transform

Let $f_t \left(x, y, z \right) \rightarrow \mathbb{R}$ be a dynamic volumetric image where $\left(x, y, z \right) \in \mathbb{R}^3$ are Cartesian coordinates in image space and the subscript $t \in [0, 1)$ is a normalized time variable. The function f_t is compactly supported in a normalized cylindrical field of view such that $f_t \left(x, y, z \right) = 0$ when $x^2 + y^2 > 1$.

Let $g_t \left(u, v \right) \rightarrow \mathbb{R}$ be the line integrals of f_t where $\left(u, v \right) \in \mathbb{R}^2$ are Cartesian coordinates in projection space. In this chapter, projections are taken sequentially for a full circular trajectory with parallel-beam geometry. Hence, g_t is akin to the Radon transform and the values of line integrals are equal to

$$g_t \left(u, v \right) = \int_{-1}^{1} f_t \left(P'_\alpha \left(u, v \right) + s \, \vec{d}_\alpha \right) ds, \tag{6.4}$$

with $\alpha = 2\pi t$.

Every point of the integrated line are selected by varying the integration parameter $s \in \mathbb{R}$. In particular, a point is located on the line segment intersecting the field of view if $|s| \leq r = \sqrt{1 - u^2}$. A sketch of the relation between u and r is shown in figure 6.2.

The orientation of the planar detector is linearly dependent on the acquisition time t, therefore every projection observes f_t at a different angle and time and thus, a potentially different deformation state. Since the set of projections g_t is three-

dimensional (2D over time) and the observed dynamic image f_t is four-dimensional (3D over time), the information of g_t is always insufficient to reconstruct f_t, except in the special case where the values of line integrals do not vary with time.

6.2.1 Motion Model

The purpose of this work is to reconstruct one static image $f(x,y,z) \rightarrow \mathbb{R}$ from the corpus of line integrals g_t that was acquired from a moving object. Since the acquired data contain line integrals of a dynamic image, the reconstruction problem is ill-posed. Nevertheless, a strategy to reconstruct a static image f from g_t is proposed. The technique assumes that the dynamic image f_t is deformed by a mathematically tractable motion model.

If f_t is the time-varying image of a moving patient, then the deformations of the body should be invertible (Chun and Fessler, 2009b,a) and therefore, a bijective mapping function $\Gamma_t(x,y,z) \rightarrow \mathbb{R}^3$ exists between the object at any temporal position $t \in [0,1)$ and the object at a reference motion state $\hat{f}(x,y,z) \rightarrow \mathbb{R}$, such that $\hat{f}(x,y,z) = f_t(\Gamma_t(x,y,z))$ and $f_t(x,y,z) = \hat{f}\left(\Gamma_t^{-1}(x,y,z)\right)$.

Note that in general, the suitable invertible deformations Γ_t are not unique. Therefore, instead of considering the whole class of time-varying deformations, this work introduces an original constrained model of the patient motion that can be seen as an extension of the admissible class of motion suggested by Desbat *et al.* (2006, 2007b).

First, the degrees of freedom of the deformation model are constrained to preserve the geometry of lines in image space. Consequently, the deformation can be represented in projection space by a bijective mapping function $D_t(u,v) \rightarrow \mathbb{R}^2$. Second, the moving regions are detected in image space and segmented by a normalized scalar field $M(x,y,z) \in [0,1]$. In this chapter, M is also called motion map.

Definition

The displacement of image elements in image space is finally modeled by backprojecting the dynamic vector field D_t and multiplying vectors by the static scalar field M and is expressed by

$$\Delta_t(x,y,z) = P'_\alpha\left(D_t\left(P_\alpha(x,y,z)\right)\right) M(x,y,z), \tag{6.5}$$

with $\alpha = 2\pi t$. The trajectories of image elements along time is given by applying the displacement in (6.5) relatively to the initial position of image elements and is noted

$$\Gamma_t(x,y,z) = (x,y,z) + \Delta_t(x,y,z), \tag{6.6}$$

where the displacement vectors of Δ_t lies on the detector plane and are therefore always orthogonal to the direction of integration lines.

Note that if $M(x,y,z) = 1$, $\forall (x,y,z) \in \mathbb{R}^3$, then the displacement vectors D_t are uniformly backprojected and $\Delta_t(x,y,z) = P'_\alpha\left(D_t\left(P_\alpha(x,y,z)\right)\right)$, with $\alpha = 2\pi t$. This restrained displacement model yields the class of deformation called *global motion* in this chapter, in opposition to the more general class of deformation considered in (6.6) and called *local motion*. A systematic comparison of image reconstruction

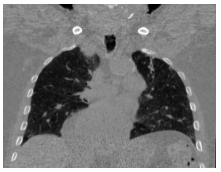

(a) Acquired projection (b) Reference projection (c) Deformation grid

Figure 6.3: Motion estimation by elastic image registration. The mapping of an acquired projection taken at the beginning of expiration (end of inspiration) to a corresponding reference projection taken at the beginning of inspiration (end of expiration) is shown by a deformation grid (c). Those two motion states are very different and thus, this specific pair of projections demonstrates a difficult registration case.

results, using global and local motion estimation and compensation, is conducted in section 6.3.

6.2.2 Motion Estimation in Projection Space

Motion estimation requires a reference static image $\hat{f}(x, y, z) \rightarrow \mathbb{R}$. The initial reference image $\hat{f}$ is reconstructed from acquired data, without any motion compensation. A set of reference projections $\hat{g}_\alpha(u, v)$ is being obtained by forward projection from $\hat{f}$ with one projection per acquisition angle $\alpha \in [0, \pi)$. Note that because of the symmetry of the parallel-beam geometry, it is required to compute reference projections only for half of a circular rotation.

The perceived deformation between each pair of acquired projections g_t and corresponding reference projections $\hat{g}_\alpha$ is represented in projection space by the bijective mapping function $D_t(u, v) \rightarrow \mathbb{R}^2$ that maps the projections $g_t(u, v)$ on the projections $\hat{g}_\alpha(u, v)$, with $\alpha = 2\pi t$:

$$\hat{g}_\alpha(u, v) = g_t((u, v) + D_t(u, v)), \quad \forall (u, v) \in \mathbb{R}^2. \tag{6.7}$$

Given the set of reference projections, displacements are estimated by registering independently all pairs of corresponding projections. The results shown in this chapter rely on a regularized elastic image registration algorithm, recently published by Chun and Fessler (2008, 2009b). The implementation is based on the B-spline model to represent both the images and the deformation field.

Regularization of the Deformation

The value of each parameter of the deformation vector field is iteratively optimized by a conjugate gradient descent method. The objective function maximizes the image similarity while a penalization term enforces that the deformation stays locally invertible. An example of registration for a pair of projections is shown in figure 6.3.

An additional modification of the penalization can capture some discontinuities that arise at the boundaries of organs like the sliding motion between ribs and the diaphragm that occurs during respiration (Chun and Fessler, 2009a). This modification has not been used in this work but could improve the robustness of

(a) Detected motion (b) Thresholding (c) Regularization

Figure 6.4: A specific coronal slice from motion segmentation in image space. The motion is first detected by reconstruction of absolute differences between acquired and reference projections (a). Then, a segmentation is obtained by thresholding (b). This binary map is regularized with a non-linear max filter and edges are smoothed by Gaussian filtering to produce the motion map (c).

the motion estimation. Moreover, alternative image registration techniques could be employed such as *optical flow* methods (Horn and Schunck, 1981; Barber and Hose, 2005) that proved to be computationally very efficient.

The reference projections are forward projected from a digital volumetric image, using a fast ray-tracing algorithm (Schretter, 2006). Since the projections are sampled from the current reconstructed image, they can be corrupted by motion artifacts and sampling inaccuracies. Therefore, the accuracy of the estimated deformation can be refined by iterating the estimation procedure, using an improved reference image, reconstructed with motion compensation.

6.2.3 Motion Segmentation in Image Space

The principle of motion segmentation from difference between line integrals was first proposed by Lin (1994) and studied further by Linney and Gregson (2001). These algorithms assume that each line integral is sampled at least twice during the acquisition. If corresponding line integrals are not equal, this indicates that some motion occurred along the line. The solution proposed here does not require redundant data but re-uses the pairs of corresponding acquired and reference projections g_t and $\hat{g}_\alpha$ that are computed for motion estimation.

For detecting motion in image space, data inconsistencies are first identified in projection space by computing the absolute differences $d_t = |\hat{g}_\alpha - g_t|$, $\alpha = 2\pi t$. The differences d_t are evaluated independently for each acquired projection and are reconstructed to detect the image elements strongly affected by motion. The reconstruction uses the regular FBP algorithm defined below in (6.8). Finally, the reconstructed image is thresholded and regularized to produce the motion map $M(x, y, z) \in [0, 1]$.

Regularization of the Motion Map

The motion map provides a rough binary partitioning of the image domain into two classes of image elements: static or moving. The regions that remain static during the whole acquisition yield consistent line integrals in projection space and the regular FBP reconstruction is very suitable for static image elements.

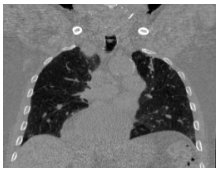

Only the moving parts of the anatomy are responsible for inconsistencies in projection data. Therefore, the motion compensation could be applied only on moving voxels during image reconstruction. The role of the motion map is to detect the static image elements in order to apply locally the motion-compensation.

Note that the differences d_t are computed independently for each line integral, therefore, the set of difference projections is not guaranteed to be consistent. Often, data inconsistencies yield large streak artifacts in reconstructions. In practice, the impact of those artifacts is not so severe for this application, since the expected result is only a rough localization of the moving regions.

In experiments the reconstruction of differences is post-processed with the following procedure. First, a binary mask is created by thresholding the image at 100 Hounsfield units (HU). Then, a non-linear max filter with a spherical structural element of radius 1 is applied to grow the segmented region. Finally, edges between moving and non-moving regions are smoothed by convolving the binary image with a volumetric Gaussian kernel. Note that the end result is exactly the same if the max filter is applied before thresholding. Other pipelines of image processing operators may equally fulfill this post-processing task.

Selection of the Threshold

The specific value of the threshold drives the sensitivity of motion detection and therefore, the threshold should be chosen as low as possible to guarantee that every moving voxel is properly detected. However, noise in the X-ray transmission measurements and the intrinsic numerical errors of the FBP reconstruction algorithm limit the maximum reachable sensitivity. If the threshold is chosen too high, then the sensitivity decreases up to the point that some moving regions are not properly detected.

The suggested value of 100 HU has been used in experiments to avoid corruption of the motion map by noise and reconstruction artifacts. Typical motion artifacts at the border of moving regions of the chest appear as a mixture of air and water. 100 HU corresponds to 10% of the difference between the attenuation value of air and water for retaining only the most significant differences between acquired and reference line integrals.

While thresholding is a very simple segmentation technique that know many refinements (Aach and Kaup, 1995), it demonstrated very sufficient performance for this simple binary segmentation problem. A visualization of the formation of the motion map is shown in figure 6.4.

6.2.4 Motion-Compensated Image Reconstruction

FBP is the method of choice for fast volumetric image reconstruction in X-ray transmission CT. An approximate FBP image reconstruction algorithm with motion compensation have already been developed by Ritchie *et al.* (1996). Several exact FBP algorithms have been derived in the works of Roux *et al.* (2004); Desbat *et al.* (2007b). The admissible motion models are various classes of mathematically tractable deformations, including affine transformations such as rigid-body transformations and non-uniform scaling. Recently, an exact reconstruction algorithm has been developed in the context of local tomography by Katsevich (2008).

Considering the local motion model in (6.6), the value of reconstructed voxels must match exactly the result of FBP in image regions where the motion compensation is not applied. Therefore, in contrast to exact reconstruction approaches, the proposed motion compensation technique does only modify the backprojection step of the reconstruction algorithm and is therefore exact only for rigid body transformations (Milanfar, 1999). Using standard uniform pre-weighting and ramp filtering of input projections enforces the important property that the reconstruction is a generalization of the regular FBP.

Reconstruction Algorithm

For full circular acquisitions in parallel-beam geometry, the regular FBP image reconstruction is implemented by first convolving, row by row, the input projections with the Ram-Lak ramp filter and dividing the filtered values by the number of projections. Then the filtered line integrals are backprojected from projection space to image space.

Let's consider that the pre-weighted and ramp filtered input projections g_t^* are available, the reconstruction of a static volumetric image $f(x,y,z) \rightarrow \mathbb{R}$ is computed by summing the backprojections of g_t^* as follows:

$$f(x,y,z) = \int_0^1 g_t^*\left(P_\alpha(x,y,z)\right) dt, \tag{6.8}$$

with $\alpha = 2\pi t$. For motion compensation, a modification is introduced within this procedure by displacing the projected position of voxels before fetching the pre-weighted filtered line integral. Therefore, the motion model in (6.6) is inserted in (6.8) and the result is an approximate motion-compensated FBP algorithm:

$$f(x,y,z) = \int_0^1 g_t^*\left(P_\alpha^\Gamma(x,y,z)\right) dt, \tag{6.9}$$

with $\alpha = 2\pi t$ and

$$\begin{aligned} P_\alpha^\Gamma(x,y,z) &= P_\alpha\left(\Gamma_t(x,y,z)\right) \\ &= P_\alpha\left((x,y,z) + P'_\alpha\left(D_t\left(P_\alpha(x,y,z)\right)M(x,y,z)\right)\right) \\ &= P_\alpha(x,y,z) + D_t\left(P_\alpha(x,y,z)\right)M(x,y,z). \end{aligned} \tag{6.10}$$

As shown by the last expression in (6.10) by using the invariant relation pointed in (6.3) the motion-compensated FBP algorithm in (6.9) can be implemented by displacing in projection space the backprojected position of the current image element.

Discussion

The motion estimation method assumes implicitly that all voxels along a given line integral are shifted by the same displacement vector. Unfortunately, this approximation can introduce certain artifacts into image regions not affected by any motion. To alleviate this issue, the dynamic displacements D_t will be weighted by scalar values of the static motion map M, produced by segmenting the motion in image space.

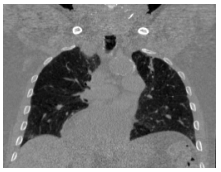

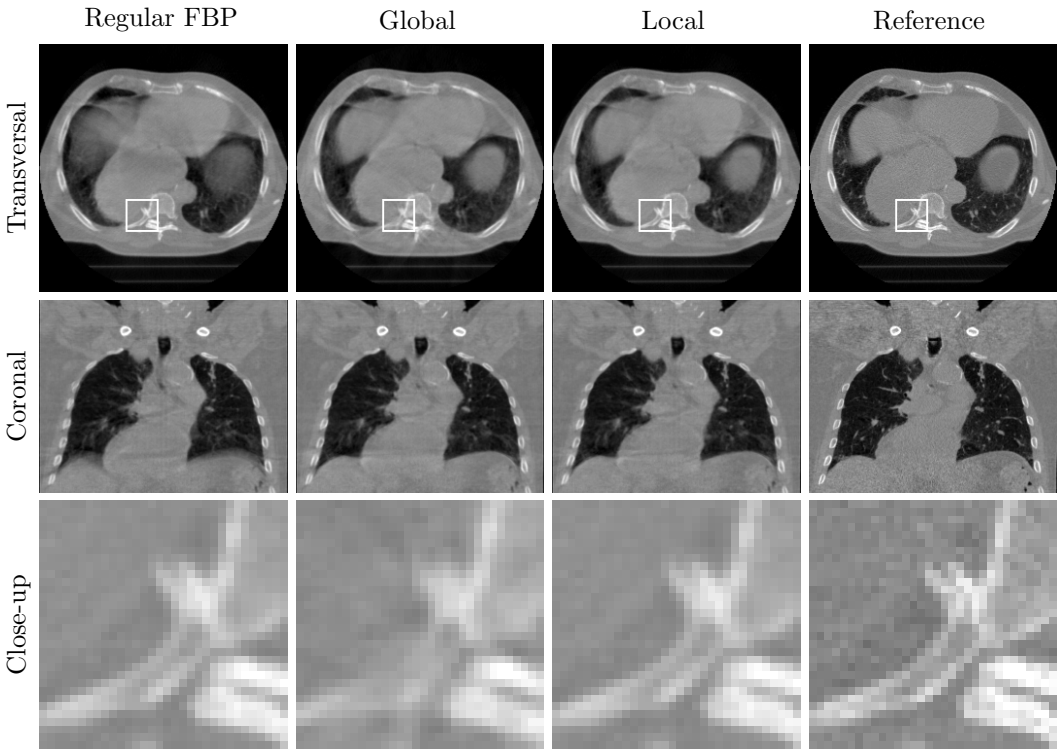

Figure 6.5: Results of ground truth experiment on motion correction with global and local motion compensation. The regular FBP reconstruction does not use any motion compensation and contains motion blur artifacts. When additional motion information is estimated and used during reconstruction, the compensated image looks very closely to the reference frame extracted from the dynamic phantom.

In the software implementation, a displacement vector is stored for each pixel of each acquired projection. The continuous time-varying two-dimensional vector field is obtained by bi-linear interpolation from the discrete samples. Furthermore, the motion-compensated reconstruction runs nearly as fast as the regular FBP since the pre-weighting and filtering input data need to be applied only once for producing all reconstructed images.

It is possible to further accelerate the local correction scheme by using the generalization property of the motion-compensated reconstruction algorithm. Indeed, if $M(x, y, z) = 0$, then the value of reconstructed voxel at position (x, y, z) will not change from the initial reconstructed image. Hence, it is sufficient to reconstruct with motion compensation, only the voxels where $M(x, y, z) \neq 0$. For the final image, the resulting local reconstruction can be composited with the initial image, using the values of M as blending factors. This procedure dramatically saves the computational cost by computing the correction only in the region of interest where strong motion artifacts are detected.

6.3 Results

In this section, all slices are extracted from volumetric images represented by a Cartesian grid of 256×256×198 isotropic 1.36 mm voxels. Transversal views show

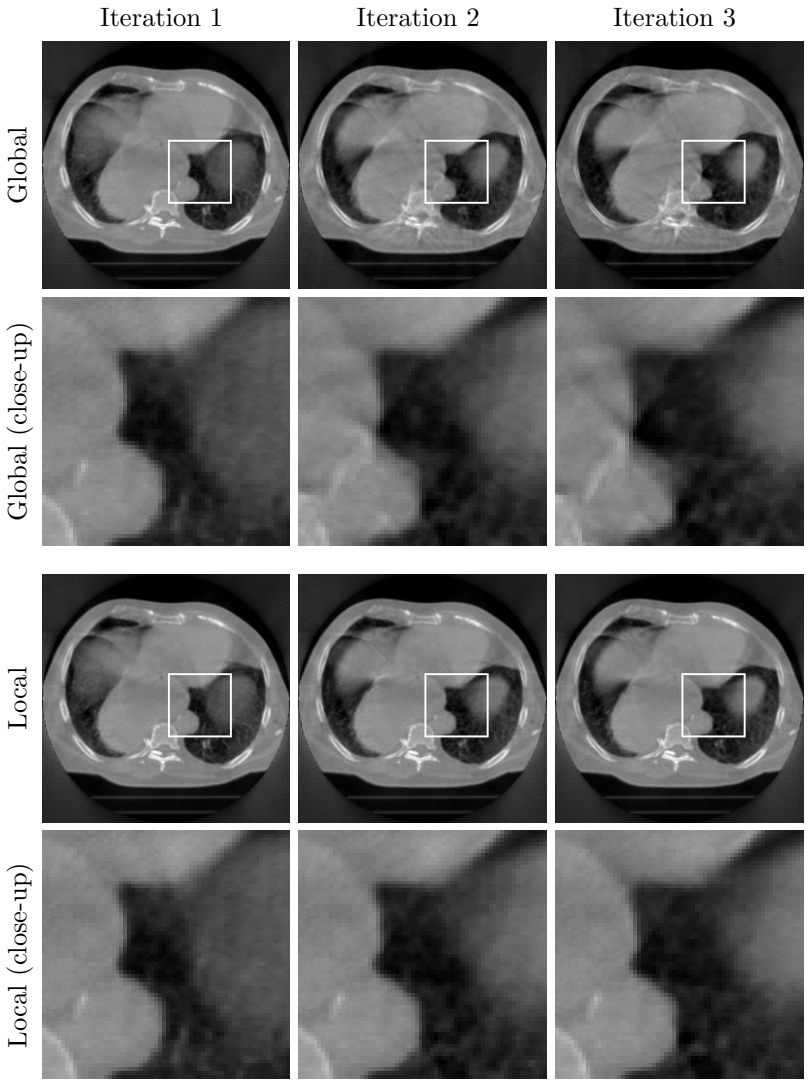

Figure 6.6: Transversal slices extracted from the results of iterative motion correction with global and local motion compensation. Static regions become deteriorated with global motion correction while their sharpness is preserved with local motion correction. The white squares show the boundaries of close-up views.

the slice number 40 and coronal views show the central slice. Those slices have been selected because they exhibit strong motion artifacts without correction. The window level and width are 0 and 2000 Hounsfield units (HU), respectively. Hence, gray corresponds to the attenuation value of water and black corresponds to air.

Experiments are conducted on synthesized projections, sampled from the clinical dataset shown in figure 4.4. This dynamic phantom is a sequence of 40 frames, reconstructed from a respiratory-gated helical CT acquisition. A set of 360 parallel-beam projections was forward-projected from this dynamic phantom for one full rotation with a circular trajectory. The simulated acquisition time was 12 seconds, approximating the typical speed of a rotating C-arm system, when used for soft tissue imaging.

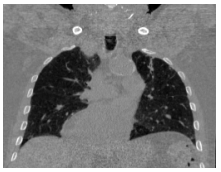

Frame 11/40

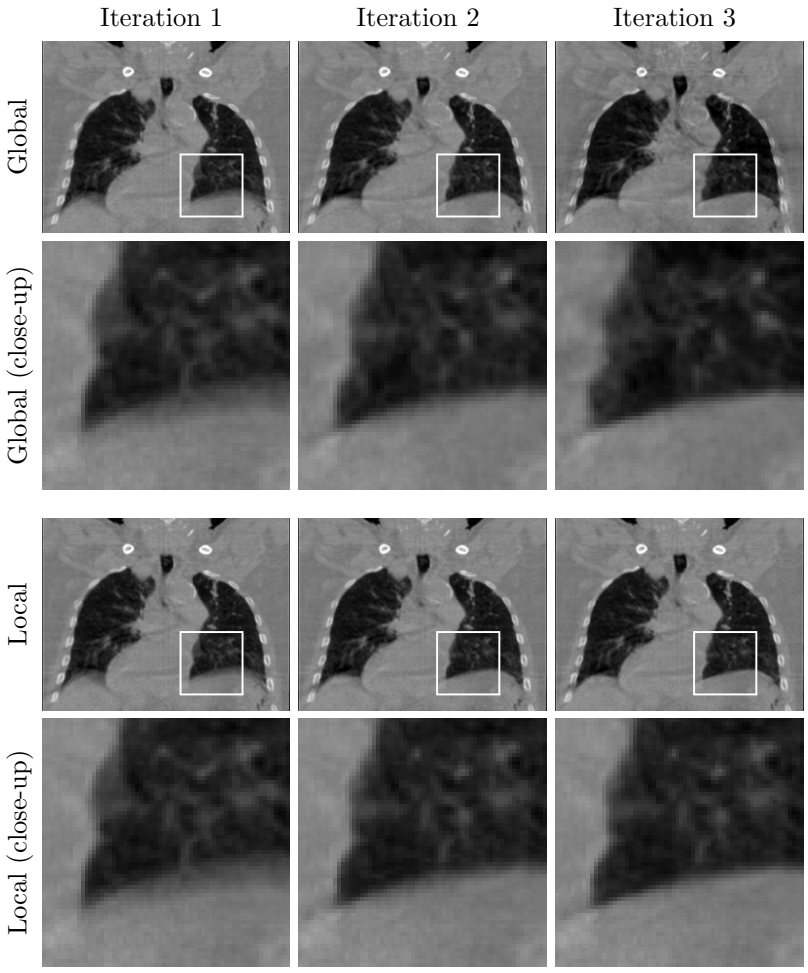

Figure 6.7: Coronal slices extracted from the results of iterative motion correction with global and local motion compensation. For both methods, the border of the diaphragm becomes sharper as seen in the coronal slice. The white squares show the boundaries of close-up views.

Figure 6.5 compares images reconstructed with local or global motion correction using a set of projections sampled from a static image for motion estimation and segmentation. For this experiment, the frame number 8 has been chosen from the dynamic phantom as a ground truth and consistent reference projections are forward projected from this image. The accuracy of the motion model and the modified reconstruction method can be assessed by comparing the output images with the ground truth reference.

Global and Local Motion Compensation

The less accurate global motion compensation yields local image corruption. This effect is especially prominent in transversal views, for the spinal bones that remain static during the whole acquisition. This experiment proves the capability of the local motion correction method to appropriately correct motion artifacts if a reference image is known.

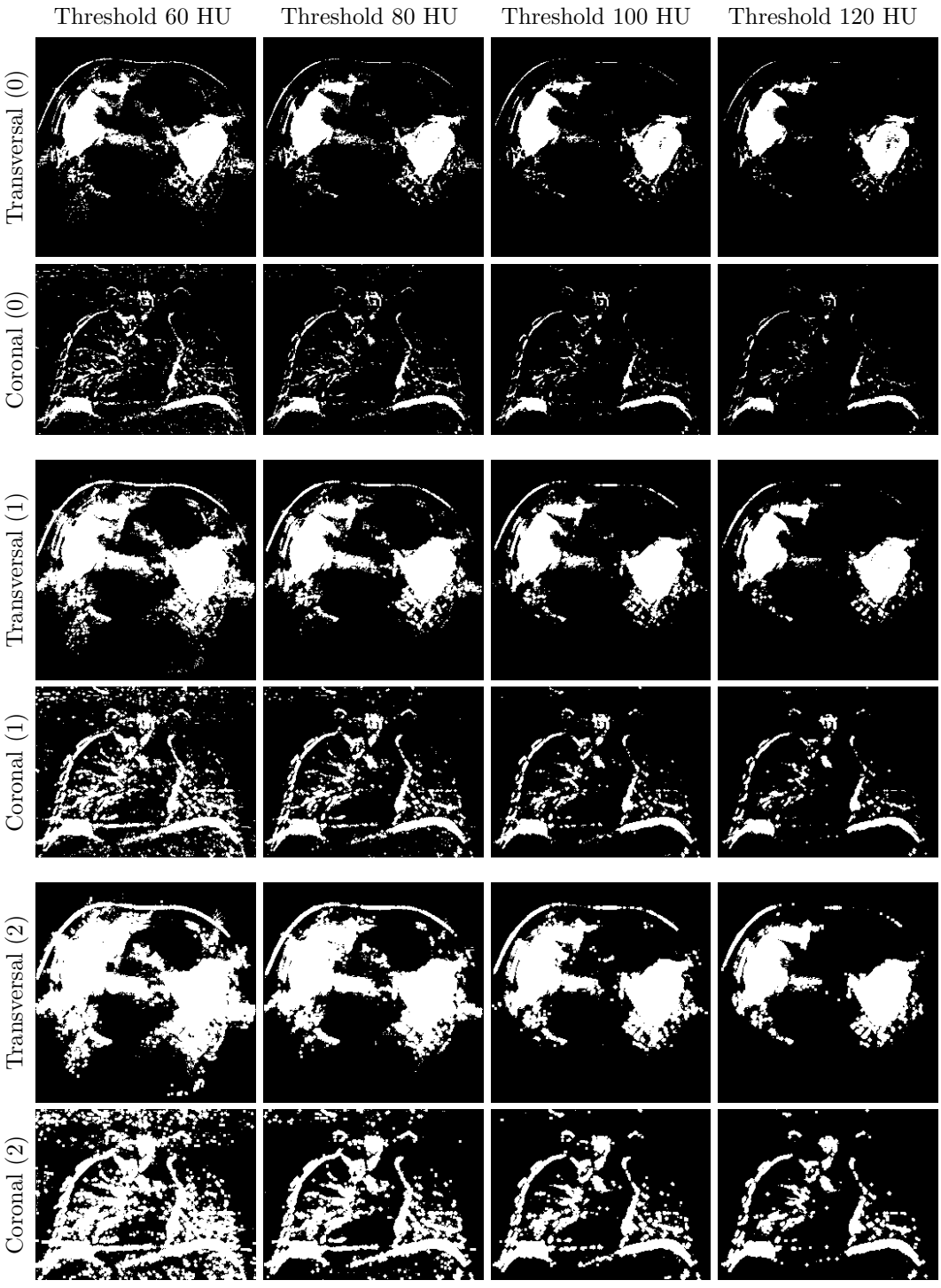

Figure 6.8: Exploration of the influence of various parameters for motion segmentation. Images are binary segmentations that are produced as intermediate step before edge smoothing. The influence of the thresholding parameter shown by column headlines is combined with various max filter operations. The radius of the spherical structural element used for the max filter is chosen between 0, 1, and 2 and is indicated between braces.

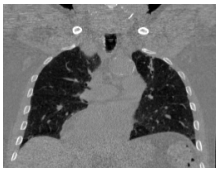

Frame 10/40

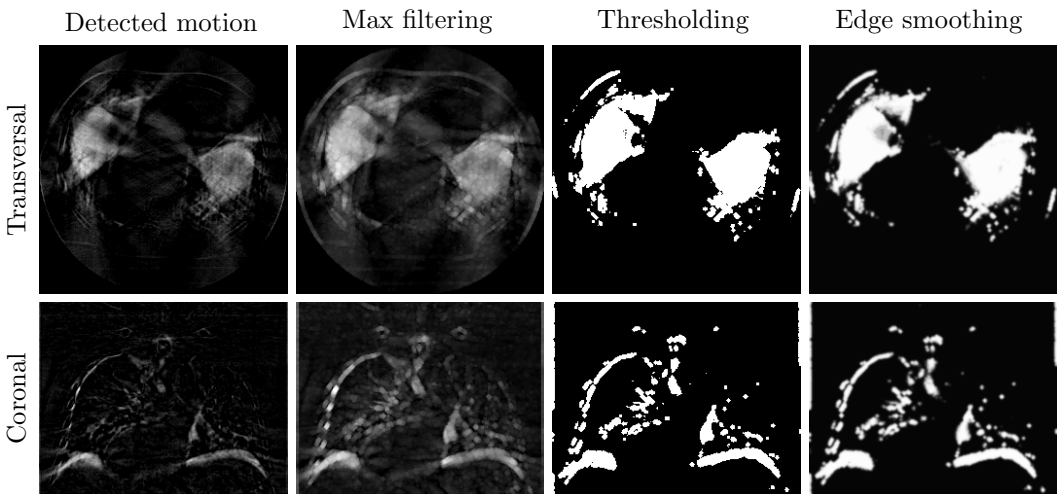

Figure 6.9: Image formation of the normalized motion map after the first iteration. The detected motion image is reconstructed from the absolute differences between acquired and sampled line integrals. Then, the image is regularized with the non-linear max filter and a threshold is applied to obtain a binary image. Finally, edges are smoothed by discrete convolution with a 5×5×5 volumetric Gaussian kernel.

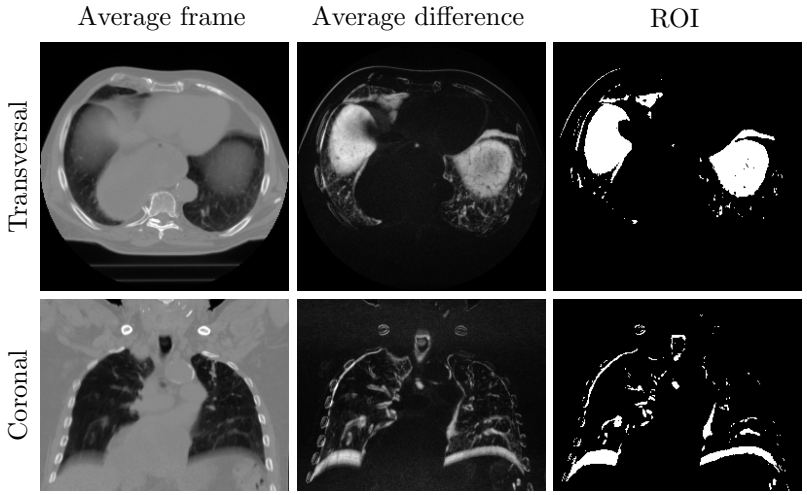

Figure 6.10: Image formation of the region of interest (ROI) for quantitative analyses, extracted from the dynamic phantom. The average of all 40 frames contains motion blur in regions where patient movements are observed. The average of the differences between the average frame and each frames of the phantom emphasizes the location of observed motion. Thresholding this image gives the binary ROI composed of voxels that are significantly affected by motion. Note the similarity to the motion map shown in figure 6.9.

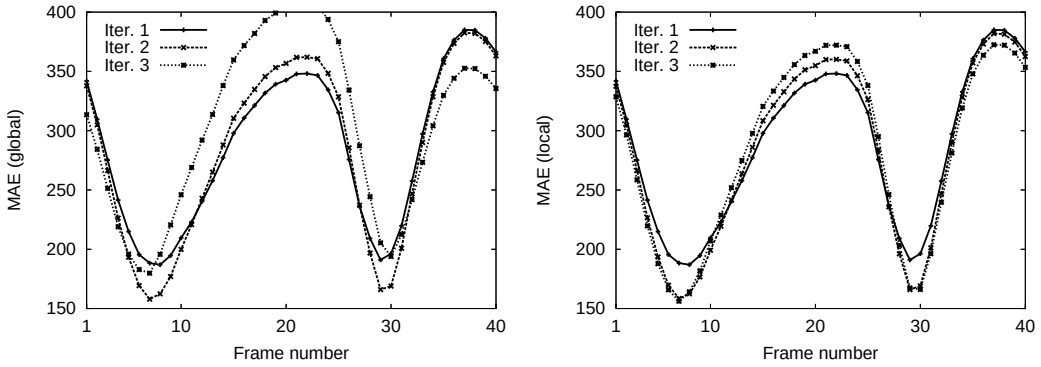

Figure 6.11: Quantitative analyses of reconstructed images after 1, 2, and 3 iterations when the correction is applied globally (left) or locally (right). The plots show the mean average error (MAE) between the reconstructed image and each of the 40 frames from the breathing phantom. Evaluation considers the region of interest (ROI) in figure 6.10. The minimum points of the curves correspond to frames number 8 and 29.

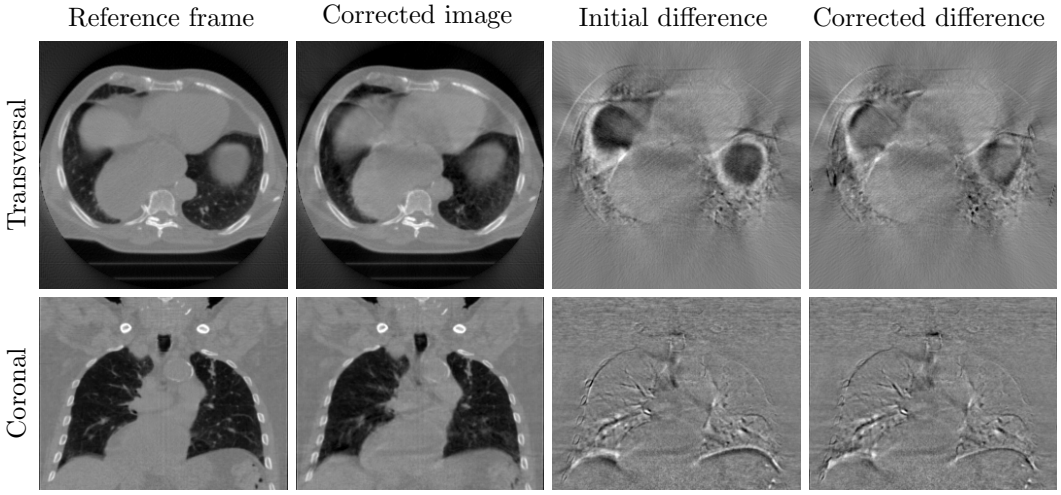

Figure 6.12: Side-by-side comparison between a reference frame and the image reconstruction after the first iteration with the local correction method. The reference frame is the average of frames 8 and 29 of the free breathing phantom. The difference image for the initial FBP reconstructions emphasizes motion artifacts. After the first iteration of local motion correction, the second difference image is already much more uniform. For the difference images, the window level and width are 0 and 1000 HU, respectively.

Results of image reconstructions with iterative motion corrections are shown in figure 6.6 and figure 6.7. The initial image does not use any compensation and is therefore identical for both global and local compensation results. This image is repeated to ease visual comparisons. The progressive improvement of image quality follows the number of iterations. The visual difference between results obtained with global and local motion correction is very clear in the smaller scale close-up views.

Two or three iterations are usually sufficient since the relative difference between subsequent motion-compensated images becomes small. Using a higher number of iterations should be avoided due to the fact that the FBP reconstruction does introduce certain inaccuracies in the image. Notably, sampling artifacts and the finite

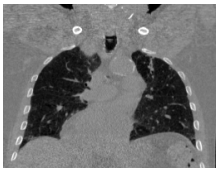

Frame 9/40

number of projections limit intrinsically the accuracy of analytical reconstructions.

Motion Estimation and Segmentation

For elastic image registration, the spacing between control knots of the B-spline grid is 8 pixels. The resulting deformation after 32 internal iterations of the registration algorithm is retained. It has been observed that the additional penalization term preserved the smoothness of the deformation. However, in practice, the chosen number of iterations and the resolution of the grid also play a prominent role to regularize the deformation estimate.

The local motion compensation requires the creation of a normalized motion map as explained by the gray-shaded part of the diagram in figure 6.1. Figure 6.8 compares results obtained with various values for the threshold constant and the radius of the max filter used for regularization. As expected, the extent of the segmented regions tends to increase with diminishing values for the threshold.

The max filter grows the boundaries of the segmented regions and ensures that every potentially moving voxel is detected while avoiding noisy segmentation that could result from a too sensitive threshold value. Figure 6.9 shows the intermediate steps of the motion map creation for the first iteration, with the parameter set chosen for the experiment (threshold of 1000 HU and max filter of radius 1). The black regions in the final image segment voxels where no compensation is applied at all.

The progressive improvement in image quality has been assessed quantitatively in a region of interest (ROI) extracted from the frames of the phantom, as shown in figure 6.10. First, the average frame has been computed from the 4D dataset. This image contains motion blur in regions where patient motion occurred, while static regions remain sharp. Moreover, the noise variance has been reduced significantly by the averaging process.

Second, the average difference from the average frame has been computed. This image emphasizes regions where motion can be observed and is therefore also the ground truth of the motion map used for local motion compensation. Finally, the average difference image is thresholded at 100 HU to select voxels of the ROI.

Interpretation

Curves resulting from quantitative analyses are shown in figure 6.11. The mean absolute error (MAE) between the static reconstructed images and each frame of the dynamic phantom is plotted. If both images contain N image elements selected by the subscript $i \in [1, N]$, the MAE measure of the error between a reconstructed image I and one specific frame F in the ROI is

$$\mathrm{MAE}\,(I, F) = \frac{1}{\sum_{i=1}^{N} \mathrm{ROI}_i} \sum_{i=1}^{N} |I_i - F_i| \cdot \mathrm{ROI}_i, \tag{6.11}$$

where ROI is the binary image shown in figure 6.10, indicating for each voxel $I_i, \in [1, N]$ if it belongs or not to the region of interest where measurements are meaningful.

The error curves follow the breathing signal and their amplitude increases with iterations. However, the curves are shifted up by increasing offsets with global mo-

tion compensation. In fact, if any displacement is applied in static regions of the image, then the method introduces motion corruption instead of motion compensation and the image quality is locally deteriorated. This offset is much smaller with local motion correction.

The points of minimum error in figure 6.11 indicate that the motion corrected images tend to converge toward gates 8 and 29 of the phantom. Those gates correspond to motion states at half-way between the beginning (or the end) of exhalation and inhalation. Those two motion states are by nature very similar since the respiratory motion is a roughly periodic back and forth movement. A significant error reduction is observed for those gates. The progressive convergence towards frames 8 and 29 is shown by the difference images in figure 6.12.

Convergence towards the intermediate motion states can be explained as follows. As can be observed in the plots of figure 6.11, without any motion correction, the blurred reconstructed image is close to the motion states of frames 8 and 29. Since this intermediate image is considered as a static reference for motion estimation, in the next iteration, the motion-compensated image tends to further improve this proximity by sharpening the blurred structures observed in the initial reconstruction.

6.4 Conclusion

In this chapter, an iterative motion correction method for static image reconstruction in computed tomography has been presented. The motion correction problem is split into three sub-problems: motion estimation, motion segmentation and motion compensation. For motion estimation, an elastic image registration algorithm estimates a displacement vector field that warps acquired projections on corresponding reference projections.

For motion segmentation, the absolute difference between acquired and reference line integrals are reconstructed first. Then, an image processing pipeline regularizes the image and provides a normalized scalar image, called motion map. Finally, motion compensation is applied locally within an analytical FBP image reconstruction algorithm by displacing image elements before backprojection.

The motion segmentation method produces a normalized motion map, associating each image voxel with an estimate of the motion magnitude present there. The motion map is combined with the motion correction scheme in order to locally apply a compensation for motion during image reconstruction. However, the motion map can also be used in different ways. For example, the motion information could be displayed in overlay to highlight the voxels that are potentially corrupted by reconstruction artifacts due to patient motion.

The main originality of the proposed solution is that the underlying motion model is not assumed to be periodic and the motion compensation is applied only locally during image reconstruction. Therefore, the technique can also be applied on X-ray projections acquired during breath-hold acquisitions to compensate for unstructured residual patient motion. In this work, a novel approach for local motion estimation and compensation was evaluated in parallel-beam geometry. While the same methodological framework is in principle also applicable to cone-beam geometry, certain adaptations and extensions are required for the latter case.

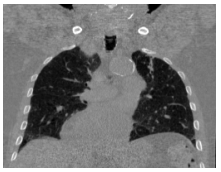

7

Local Motion Correction in Cone-Beam Geometry

Divergent ray geometries are widespread today for X-ray transmission computed tomography (CT) because classical X-ray generators emit high-energy photons from a single point source. Cone-beam geometry refers to the class of divergent rays geometries when radiations are detected by a multi-row planar or curved detector. In order to adapt to practical constraints, this work proposes a method to detect and to estimate *arbitrary* patient motion in cone-beam geometry. In contrast to the parallel-beam geometry studied in the previous chapter, the technique also takes into account image *truncations* associated to divergent ray geometries.

This work extends the method described in the two preceding chapters to the cone-beam geometry and validates it on physiologically plausible motion. The motion information is computed from truncated data and then used within a motion-compensated variant of the FDK algorithm to improve the image quality. Because of truncation issues, the method can not be applied iteratively anymore in order to improve the estimate of the motion information.

This work has been presented at the 10^{th} International Meeting on Fully Three-Dimensional Image Reconstruction in Radiology and Nuclear Medicine (Fully3D) organized on the September 6–12 of 2009 in Beijing, China (Schretter *et al.*, 2009d).

7.1 Introduction

Our motion estimation and compensation approach has been first developed in the context of parallel-beam tomography. In the precedent chapter, the experiments have been conducted using the exact reconstruction algorithm of Roux *et al.* (2004) for a parallel-beam acquisition geometry. However, in principle the technique does not depend on the acquisition geometry and the source trajectory, since the motion is estimated independently for each acquired projection.

It should be noted that for divergent rays geometries with circular trajectory, the image reconstruction can not be exact for arbitrary objects (Tuy, 1983; Finch, 1985). Therefore, so-called cone-beam artifacts can corrupt the reconstructed image when using the popular FDK algorithm (Feldkamp *et al.*, 1984). The possible

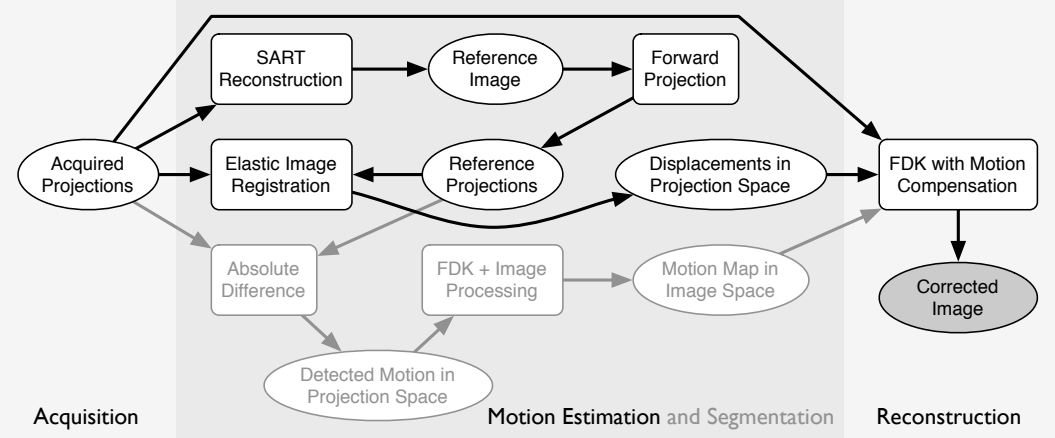

Figure 7.1: Workflow for motion estimation, segmentation, and compensation. First, reference projections are forward-projected from a scout image reconstructed with SART. Displacement vectors are estimated in projection space by elastic image registration of acquired projections on reference projections. In parallel, the motion is segmented in image space by reconstructing absolute differences between acquired and reference projections. Finally, the image is reconstructed again with local motion compensation.

shading artifacts could be corrected (Hu, 1996; Zhu *et al.*, 2007) before sampling reference projections or an alternative trajectory could be used, as proposed for instance by Schomberg *et al.* (2009).

The motion-compensated reconstruction relies on the heuristic algorithm of Schäfer *et al.* (2006). Taguchi and Kudo analyzed the properties of this algorithm (Taguchi and Kudo, 2008b) and concluded that "the fan-beam and cone-beam versions of Schäfer's method are a very good approximation of the exact method." This statement is confirmed by our experiments. Indeed, the motion-compensated FDK reconstruction from a simulated free breathing acquisition shows very good agreement with the objective image.

The remainder of this chapter is structured as follows. Notations and an outline of the motion estimation and segmentation methods are given in section 7.2. Experimental results conducted on simulated data from a realistic respiratory phantom are discussed in section 7.3. Two related experiments have been analysed. First, the motion is estimated in projection space by optical flow-based elastic image registration, using reference projections of a known static image. Second, the motion is estimated from approximate reference projections that are computed by the SART method, using solely the acquired data. Finally, conclusions are drawn in section 7.4.

7.2 Method

The motion estimation method is split into three sequential steps which are solved by standard algorithms from the image reconstruction and image processing communities. The three steps of this workflow are summarized by the diagram in figure 7.1.

First, a sequence of reference projections is synthesized from the acquired projections. Those reference projections are sampled from a voxelized image and therefore

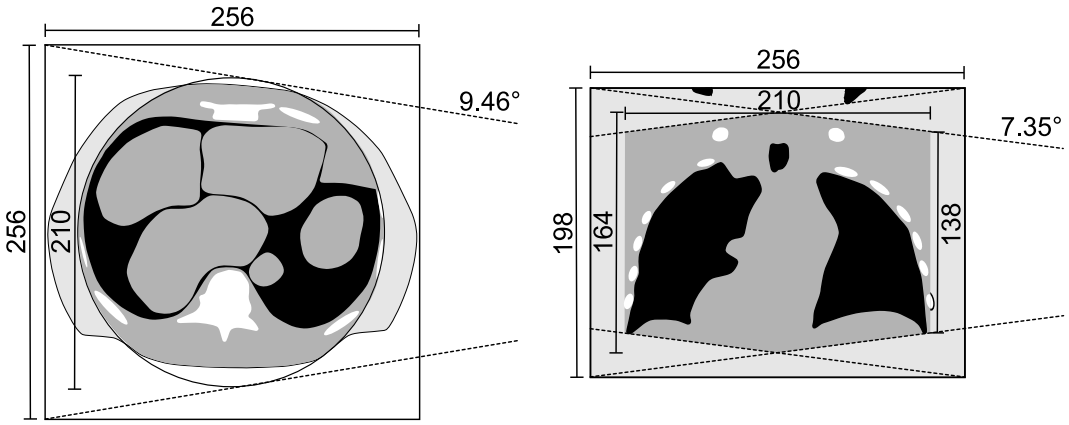

Figure 7.2: Illustration of the reconstructed region of interest (ROI) observed by all projections, in cone-beam geometry. The ROI is a truncated cylinder caped by two *Chinese hats* and is smaller than the whole field of view (FOV). The fan angle is 18.9°. The maximum cone angle is 14.7°. The definition of reconstructed images is $256 \times 256 \times 198$ voxels.

a scout image is required. This intermediate image is reconstructed with the SART method to aleviate artifacts from data truncation.

Second, a 2D displacement vector field that maps every acquired projection on its corresponding reference projection is computed using optical flow-based elastic image registration. Third, a binary segmentation is obtained from the reconstruction of absolute difference between acquired and reference projections. The motion segmentation can be executed in parallel with motion estimation.

Finally, a static image is reconstructed with the modified FDK algorithm in (7.12) that uses both the motion estimate and the segmentation to apply locally a compensation during the back-projection step. In fact, only a limited region of the field of view (FOV) can be reconstructed, and the reconstruction is exact only in the central slice. In addition, since the size of the detector is limited, projections are truncated as well. Nevertheless very encouraging results are obtained, by using only a single iteration for motion estimation. The three steps of the method will be described in more details in the following sections.

Projection and Backprojection

With circular trajectory and cone-beam geometry, divergent X-rays are emitted from a point source and attenuated intensities are measured by a planar detector. The point source is located at distance R from the rotation axis and the detector is positioned at distance $R + D$ from the point source such that the radius of the cylindrical field of view (FOV) is equal to D. The region of interest (ROI) that should be reconstructed is composed of image voxels that are observed in every projection. The geometry of a realistic C-arm system illustrated in figure 7.2 is simulated by choosing $R = 5D$.

Let $f_t(x, y, z) \to \mathbb{R}$ be a dynamic volumetric image where $(x, y, z) \in \mathbb{R}^3$ are Cartesian coordinates in image space and the subscript $t \in [0, 1)$ is a normalized time variable. The function f_t is compactly supported in the cylindrical FOV such that $f_t(x, y, z) = 0$ when $\sqrt{x^2 + y^2} > D$.

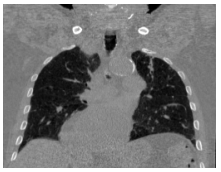

When the arm is oriented at angle $\alpha \in [0, 2\pi)$, the perspective projection operator

$$P_\alpha(x, y, z) = (y\cos\alpha - x\sin\alpha, z)\,\frac{(R+D)}{U} \tag{7.1}$$

maps a point $(x, y, z) \in \mathbb{R}^3$ defined in object space to a point $(u, v) \in \mathbb{R}^2$ defined in projection space. The denominator in (7.1) is the *perspective factor*

$$U = U_\alpha(x, y) = R + x\cos\alpha + y\sin\alpha \tag{7.2}$$

which is equal to the distance between the source and the orthogonal projection of the voxel position on the central plane. The central plane contains the source point and is orthogonal to the rotation axis.

The adjoint of the perspective projection operator

$$P'_\alpha(u, v) = (-u\sin\alpha, u\cos\alpha, v)\,\frac{R}{(R+D)} \tag{7.3}$$

maps a point $(u, v) \in \mathbb{R}^2$ defined in projection space to a point on a *virtual detector* defined in object space. The constant ratio $R/(R+D)$ is called the *magnification factor*. The virtual detector shares the same orientation with the real one, but is smaller, proportionally to the magnification factor and centered on the origin of the FOV. Note the relation

$$P_\alpha\left(P'_\alpha(u, v)\right) = (u, v), \quad \forall\,(u, v) \in \mathbb{R}^2, \tag{7.4}$$

however (7.3) is not the inverse of (7.1) since $P'_\alpha(P_\alpha(x, y, z)) = (x, y, z)$ is true only for points that lie on the virtual detector, when $U = R$ and thus, when $x\cos\alpha + y\sin\alpha = 0$.

Radon Transform

Let $g_t(u, v) \to \mathbb{R}$ be the line integrals of f_t where $(u, v) \in \mathbb{R}^2$ are Cartesian coordinates in projection space. When the arm is oriented at angle $\alpha \in [0, 2\pi)$, the position of the point source is $R\,d_\alpha$ where the vector $\vec{d}_\alpha = (\cos\alpha, \sin\alpha, 0)$ is normal to the detector plane. Therefore, the values of acquired line integrals are equal to

$$g_t(u, v) = \int_{-1}^{1} f_t\left((1-s)\,P'_\alpha(u, v) + s\,R\,\vec{d}_\alpha\right) ds, \tag{7.5}$$

with $\alpha = 2\pi t$. Points of the integrated line segment connecting the X-ray source to a pixel of the detector are selected by varying the integration parameter $s > 0$.

7.2.1 Motion Model

The motion model is similar to the one derived for the parallel beam geometry in the last chapter, however, in perspective geometry, the geometrical definition of the modeled class of motion is obviously different. The model can be seen as an extension of the admissible class of motion suggested for fan-beam geometry by Roux *et al.* (2004) and extended to cone-beam geometry by Desbat *et al.* (2007b).

The perceived motion is represented by a dynamic displacement vector field in projection space $D_t(u,v) \rightarrow \mathbb{R}^2$ and a normalized scalar field in image space $M(x,y,z) \in [0,1]$. The associated image M indicates for each voxel if some motion occurred during the acquisition. This segmentation information is a key for successful local motion compensation. The displacement of image elements in object space is modeled by backprojecting the displacement field D_t and weighting vectors with the scalar field M.

Definition

Displacements are formally expressed for the perspective geometry by the equation

$$\Delta_t(x,y,z) = P'_\alpha\left(D_t\left(P_\alpha(x,y,z)\right)\right) M(x,y,z), \tag{7.6}$$

with $\alpha = 2\pi t$. The trajectories of image elements along time are given by applying the displacement in (7.6) relatively to the initial position of image elements. Trajectories are expressed by

$$\Gamma_t(x,y,z) = (x,y,z) + \Delta_t(x,y,z), \tag{7.7}$$

where the displacement vectors of Δ_t lie on the detector plane and thus represent only the component orthogonal to the projection ray.

A particularity of the model is that neither periodicity nor spatial or temporal smoothness of the underlying motion is assumed. Therefore it could capture unwanted sudden patient motion such as hiccups, breath-hold failures, or bowel movements, for example. Although the model is approximate, our experiments demonstrate that it has the potential to capture local motion very well. The success of motion compensation mainly depends on the accuracy of motion estimation.

7.2.2 Motion Estimation in Projection Space

Motion estimation requires a reference static image $\hat{f}(x,y,z) \rightarrow \mathbb{R}$ from which a set of reference projections $\hat{g}_\alpha(u,v)$ is forward projected, with one projection per acquisition angle $\alpha \in [0,2\pi)$. The simultaneous algebraic reconstruction technique (SART) proposed by (Andersen and Kak, 1984) is used to reconstruct a pilot image from the available acquired projections.

By principle, iterative image reconstruction techniques try to estimate an image such that the error between forward projection and input projections is minimized. A corollary is that the forward projection of the image will be more robust to possible projection truncations that often arise in cone-beam geometry, see figure 7.2.

It is known that, if data are consistent, the reference projections will match the acquired projections in the weighted least square sense when using SART. However, if acquired data are corrupted by unwanted patient motion, the iterative reconstruction will never converge and the image will contain motion blur artifacts. This pilot image is nevertheless valuable for sampling approximate reference projections.

Experiments demonstrate that even if the resolution of those approximate reference projections is limited by motion blurring, their quality is sufficient for motion estimation in projection space. The SART method is used because of its fast convergence rate but another reconstruction algorithm could have been used as well.

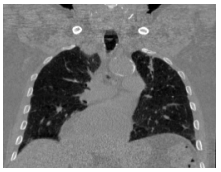

Optical Flow Tracking

The perceived deformation between each pair of acquired projections g_t and corresponding reference projections $\hat{g}_\alpha$ is represented in projection space by the bijective mapping function $D_t(u,v) \rightarrow \mathbb{R}^2$ that map $g_t(u,v)$ on $\hat{g}_\alpha(u,v)$, with $\alpha = 2\pi t$:

$$\hat{g}_\alpha(u,v) = g_t\left((u,v) + D_t(u,v)\right), \quad \forall (u,v) \in \mathbb{R}^2. \tag{7.8}$$

In this chapter, the displacement vectors D_t are computed using the optical flow principle introduced by the seminal paper of Horn and Schunck (1981). Optical flow has been applied with success for motion estimation in SPECT imaging by Gilland *et al.* (2002, 2008) and will be the object of a through study in the next chapter.

In optical-flow-based methods, the brightness of a particular point of the projection g_t is assumed to remain constant over time, so that

$$\frac{\partial g_t}{\partial t} = -D_t \cdot \left(\frac{\partial g_t}{\partial u}, \frac{\partial g_t}{\partial v}\right). \tag{7.9}$$

Provided that the displacement vectors in (7.9) are small, the chain rule for differentiation gives

$$\hat{g}_\alpha - g_t = D_t \cdot G_t, \tag{7.10}$$

where G_t contains gradient vectors that capture the direction and the amplitude of the intensity change between the two images $\hat{g}_\alpha$ and g_t. Partial derivatives are approximated by finite differences.

For robustness, the components of gradient vectors are computed for both the source and target images and then averaged such that

$$G_t = \frac{1}{2}\left(\frac{\partial \hat{g}_\alpha}{\partial u} + \frac{\partial g_t}{\partial u}, \frac{\partial \hat{g}_\alpha}{\partial v} + \frac{\partial g_t}{\partial v}\right). \tag{7.11}$$

In the implementation, vectors of (7.11) are averaged at a coarse grid of control points and then interpolated back for every pixel. This procedure improves the numerical stability but also reduces the resolution of the deformation vector field.

The present work relies on the optical flow-based elastic image registration algorithm proposed by Barber and Hose (2005); Barber *et al.* (2007). His algorithm provides an automatic regularization of the deformation grid and is both fast and robust[1]. The optimal deformation D_t is iteratively estimated by the conjugate gradient descent method.

The objective function minimizes the sum of squared differences between $\hat{g}_\alpha$ and g_t while a regularization term penalizes the updates of D_t to avoid irregularities in the final deformation. The penalization is proportional to the Laplacian of the deformation vector field computed in the previous iteration. For the first iteration, the initial deformation is a zero vector field and no regularization term is used.

[1]For cross-validation, the same experiments has been executed with the B-spline-based MATLAB implementation of Chun and Fessler (2009b) as well and very similar results are obtained. However, the implementation in the C language from Barber *et al.* (2007) has been retained for its advantageous performance benefits over MATLAB.

7.2.3 Motion Segmentation in Image Space

For detecting motion in image space, data inconsistencies are first identified in projection space by computing the absolute differences $d_t = |\hat{g}_\alpha - g_t|$, $\alpha = 2\pi t$. The differences d_t are evaluated independently for each acquired projection and are reconstructed to detect the voxels strongly affected by motion. In contrast to the method described in the previous chapter, the reconstruction relies on the regular FDK algorithm and not FBP. Finally, a threshold is applied to yield a binary image that is regularized to give the final motion map.

In experiments the reconstruction of differences is post-processed with the following procedure. First, a binary mask is created by thresholding the image at 100 Hounsfield units (HU). Then, a non-linear max filter with a spherical structural element of radius 2 is applied to grow the segmented region. Finally, edges between moving and non-moving regions are smoothed by convolving the binary image with a volumetric Gaussian kernel. Note that the end result is the same if the threshold is applied after the max filter. Alternative post-processing pipelines may equally fulfill the regularization task.

7.2.4 Motion-Compensated Image Reconstruction

For motion compensation, a modification is introduced within the FDK algorithm by displacing the projected position of voxels before fetching the pre-weighted filtered line integrals, denoted here by g_t^*.

The motion model defined in (7.7) is inserted in the backprojection of FDK and the reconstruction of a static volumetric image $f(x,y,z) \rightarrow \mathbb{R}$ is computed as follows:

$$f(x,y,z) = \int_0^1 \frac{R^2}{U^2} g_t^* \left(P_\alpha^\Gamma(x,y,z)\right) dt, \tag{7.12}$$

with $\alpha = 2\pi t$ and the displaced backprojection operator derived in the previous chapter:

$$P_\alpha^\Gamma(x,y,z) = P_\alpha(x,y,z) + D_t\left(P_\alpha(x,y,z)\right) M(x,y,z). \tag{7.13}$$

7.3 Results

Experiments have been conducted using an identical setup as described earlier for the parallel-beam case. The importance of using an iterative method for generating the scout image was evaluated first in the next sub-section. The first results with motion compensation for a realistic divergent rays geometry and truncated data are then presented. The experiments validate the method on a challenging scenario, when the patient is breathing freely.

The dynamic phantom is a sequence of 40 frames reconstructed from a respiratory-gated helical CT acquisition shown in the first chapter. The simulated acquisition time was 12 seconds, matching the typical rotation speed of a C-arm system when used for soft tissue imaging. The experiments validate the method on a challenging scenario, when the patient is breathing freely. The following sub-sections specify the experimental setup and discuss results.

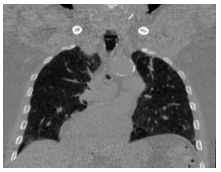

Frame 5/40

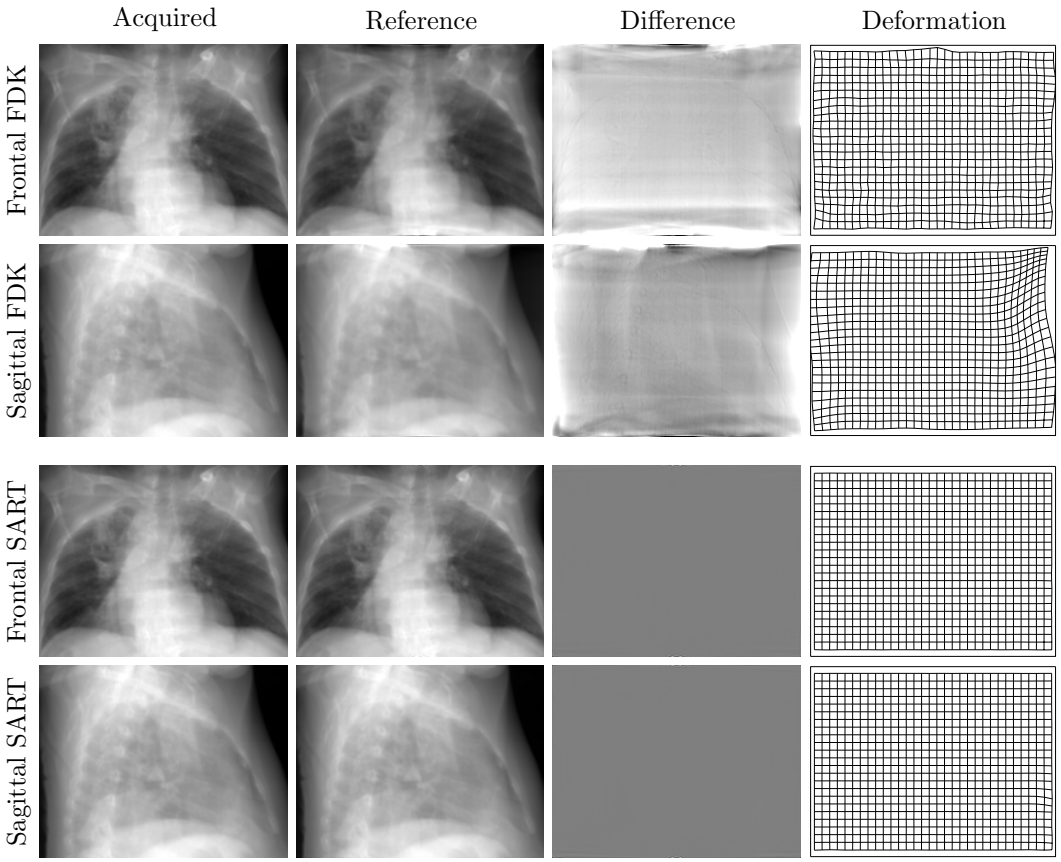

Figure 7.3: Registration of two pairs of projections when the reference projection has been forward projected from a volume reconstructed with the FDK or the SART method. The difference between the original acquired projection and the synthetic projection projected from the FDK reconstruction reveals innacuracies. Therefore, some spurious motion information is visible nearby image borders. However, reference projections computed with SART match perfectly the acquired data.

For visualizing results of volumetric image reconstruction, all slices are extracted from volumetric images represented by a Cartesian grid of 256×256×198 isotropic voxels of size equal to 1.36 mm. Gray is set to the attenuation of water and the window width equals 1000 HU such that black corresponds to the attenuation of air. To simulate a motion-corrupted acquisition, a set of 360 projections for one full circular rotation was forward-projected from the dynamic free-breathing phantom shown in figure 4.4.

Generation of Reference Projections

For effective motion compensation, the patient's motion has to be detected accurately in projection space. It is also important that eventual reconstruction artifacts present in the reference projections are not recognized as motion. In cone-beam geometry, volumes can be reconstructed only approximately and therefore an experiment has been conducted in order to evaluate the robustness against inaccuracies induced by specific reconstruction algorithms. One set of projections was recon-

structed using both the FDK and the SART method and then the volume was projected to generate reference projections.

For this experiment, it is expected that the estimated deformation field is composed of null vectors, since no motion occurred during the simulated acquisition. The registration was executed independently on pairs of projections and typical frontal and sagittal projections can be seen in figure 7.3. Since FDK does not preserve oblique line integrals and does not reconstruct the whole field of view, unacceptable spurious motion arises after the image registration step.

In constrast to FDK, the iterative methods such as SART do not suffer from data truncations and provides therefore ideal reference projections. As expected, the deformation grid is stationary because no motion was detected. From its core principle, the SART method guarantees that the forward projections match the input views as good as possible. Neither cone-beam artifacts nor truncation-induced distortions are recognizable in the forward projected views or the difference to the ideal projections.

Image Reconstruction

For the first experiment, reference projections have been computed by the SART method while for the second experiment, reference projections have been simulated from a chosen reference frame of the dynamic volumetric image. Using a ground truth static reference image, it is possible to assess the accuracy of the motion estimation and compensation method by measuring the similarity of the reconstructed image with the reference image. Quantitative analyses consider only voxels where motion compensation is applied. The mean absolute error (MAE) equals 151 HU without motion compensation and 61 HU with reference motion estimation.

Results of image reconstructions are shown in selected transversal and coronal slices in figure 7.4. The images emphasis the region of the myocardium in a transversal slice and the region of the respiratory diaphragm in a coronal slice. The second column (approximate estimation) shows that the image gets sharper with motion estimation and segmentation using approximate reference projections. The third column (reference estimation) contains slices of the reconstructed image when using reference projections from a known static image for motion estimation. The motion-compensated image is very close to the reference image shown in the last column.

Without compensation, the border of the myocardium and vessels appears blurred in transversal views and the border of the diaphragm is very fuzzy in the coronal view as well. The border of the myocardium and the vascular structures in the lungs get sharper with motion compensation. The contours of ribs become also sharper. However, motion estimation from approximate reference projections did not succeed to suppress the blurring observed at the border of the diaphragm.

7.4 Conclusion

In practical application of CT, there are complications due to axial truncations of the image region that can be reconstructed in divergent ray geometries with circular source trajectories. Therefore, this work proposes a practical technique to improve

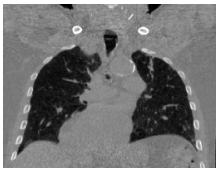

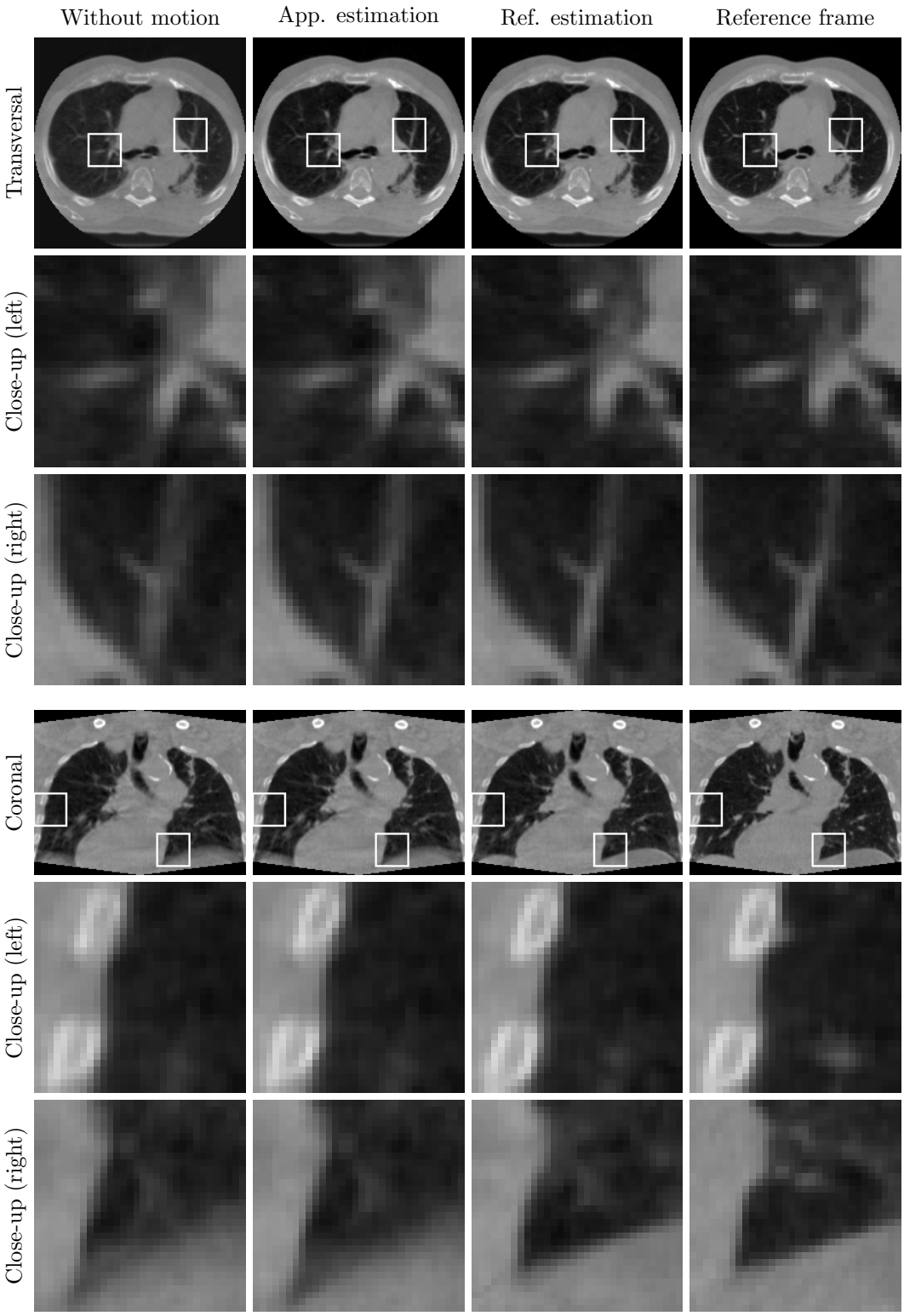

Figure 7.4: Results of image reconstructions for two motion estimation experiments, compared to a static reference frame. Partial motion compensation is acheived when using approximate (App.) reference projections. A very sharp image can be obtained when ideal reference (Ref.) projections are available. The white frames mark the boundaries of the close-up views.

image quality when acquired data are corrupted by arbitrary patient motion. First an iterative reconstruction is performed to produce a set of reference projections. Then, the perceived motion is estimated in projection space by elastic image registration and segmented in image space by reconstructing the absolute differences between acquired and reference projections. Finally, a motion-compensated image is reconstructed by a slightly modified FDK implementation. Motion blur artifacts are locally reduced with motion compensation.

With the proposed technique, motion compensation can be applied in a smaller cylindrical region enclosed in the field of view and it is even possible to estimate organ motion near the border of the image. Unfortunately, the diaphragm of the respiratory-gated image used in experiments crosses the border of this region of interest and therefore data are missing for continuous motion estimation of organs leaving in and out the FOV. In addition, with flat detectors of limited size the possible lateral truncations of projections have been addressed.

The method has been validated on experiments using a dynamic image reconstructed from clinical patient data. Results demonstrate a great potential to estimate and compensate breathing motion. Since the underlying motion model does not assume periodicity, the described technique may capture arbitrary residual patient motion that corrupts the data in breath-hold acquisitions.

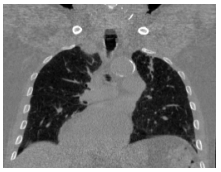

8

Elastic Image Registration for Motion Estimation

Elastic image registration is a fundamental technique for the estimation of non-rigid motion from image sequences. A successful image registration procedure provides a displacement *vector field*, mapping the center of every pixel of a source image to the corresponding location in a target image. The source and target images should be roughly similar to yield a well-posed problem.

Image registration techniques can be classified into *rigid*, *affine*, and *elastic*. Rigid registration describes all rigid-body deformations such as rotation and translations. Affine registration extends this class of allowed deformations by also capturing additional deformations such as uniform and non-uniform scaling. On the other hand, elastic registration deals with local deformations and has the potential to capture organs moving individually during breathing, heart beating, or other source of movement. The algorithms used for this purpose are often more complex.

The central and most sensitive part of the motion correction workflows presented in the three previous chapters is undoubtely the motion estimation stage. This chapter is dedicated to the comparison and assessment of two alternative techniques solving the important motion estimation problem from a sequence of X-ray projections. In this work, only non-rigid elastic registration techniques are considered. An iterative algorithm based on the *optical-flow* theory and a direct method based on *block-matching* are described and compared.

8.1 Introduction

One very common approach to elastic image registration (Hill *et al.*, 2001; Maintz and Viergever, 1998) are so called *free-form deformations* (FFD) where a grid of control points is defined and then manipulated (Rueckert *et al.*, 1999). These control points can either be placed on features extracted from the images or be placed on a regular or irregular grid. The deformation itself is then modeled using splines such as the triangular kernel, thin plate splines (TPS), but mostly cubic B-splines (Unser, 1999, 2000) are popular because of their advantageous trade-off between accuracy and computational efficiency.

Having the grid and the deformation model, a cost function is designed which consists primarily of a similarity metric evaluating the difference between the source and the target images. The registration is then performed by minimizing the cost function, which corresponds to minimizing the image dissimilarity between the deformed source image and the reference target image. For this purpose, different optimization algorithms can be used (Klein *et al.*, 2007) such as the Gauss-Newton method (Bartoli and Zisserman, 2004), the Levenberg-Marquardt algorithm (Kabus *et al.*, 2004), or the method of conjugated gradients (CG) (Chun and Fessler, 2008; Barber and Hose, 2005). During iterative optimization, the parameters of the model function are altered until the relative improvement becomes negligible.

Since in many cases the deformation is constrained, a regularization term is added to the cost function, weighted by a factor that counteracts the deformation. Usually the regularization terms are designed such that the value of this term increases with the amplitude of the computed displacement. In the work of Chun and Fessler (2008, 2009b), a regularization method is presented based on a novel and very attractive penalization to ensure local invertibility. Alternatively, a rigidity penalty term can be used (Staring *et al.*, 2007; Chun and Fessler, 2009a). With regularization, the deformation is encouraged to be diffeomorphic and invertible (Ashburner, 2007).

A zoo of other registration approaches are existing. Template propagation for estimating respiratory motion (Rösch *et al.*, 2002). The popular SIFT image features have been used to select control points (Franz *et al.*, 2006). The Radon transform was also used for scale and rotation invariant image matching (Jiangsheng *et al.*, 1998). The method of demons is also popular to track borders (Thirion, 1998). In this work, only two alternative implementations based on the optical flow principles have been considered.

Optical flow-based methods track the movement of image elements, assuming that each pixel is conserving its brightness value (Horn and Schunck, 1981; Kumar *et al.*, 1996; Brox *et al.*, 2004). An alternative technique based on the popular block-matching scheme has also been implemented (Jain and Jain, 1981; Malsch *et al.*, 2006; Chen, 2009). Block matching procedures are known to be fast and experiments with this specific implementation demonstrated very surprising accuracy.

The remainder of this chapter is structured as follows. A state of the art free-form deformation based registration technique is presented in section 8.2. This algorithm has been used for motion estimation in the experiments from the previous chapter. For comparison a direct registration method based on block matching is described in section 8.3. Section 8.4 presents a comparative analysis of results obtained by the two techniques. An extensive discussion of parameters is provided. Further research and experiments are suggested in section 8.5.

8.2 Optical Flow

A popular approach to compute a dynamic motion vector field from an image sequence is the method of optical flow, originally introduced by Horn and Schunck (1981). Optical flow theory assumes that the brightness of each pixel remains constant over time. If the brightness has changed at one location, a deformation is estimated using image gradients in horizontal and vertical directions.

The basis assumption of optical flow methods states that the brightness E of one picture element does not change over time, hence

$$\frac{dE}{dt} = 0. \tag{8.1}$$

Applying the chain rule for derivatives gives the following relation between infinitesimal spatial displacements and the change over time of E:

$$\frac{\partial E_x}{\partial x}u + \frac{\partial E_y}{\partial y}v + \frac{\partial E_t}{\partial t} = 0, \tag{8.2}$$

with $u = \frac{dx}{dt}$ and $v = \frac{dy}{dt}$ being the coordinates of the optical flow velocity vectors for the image element positioned in (x, y). Thus if the pixel intensity E does not remain constant over time, optical flow velocities can be computed according to the gradients in horizontal and vertical directions. Often image gradients are approximated by finite difference.

Based on the seminal paper of Horn and Schunk, various image registration methods were developed. One of these methods is the Sheffield image registration toolkit (ShIRT) from Barber and Hose (2005); Barber *et al.* (2007) on which a closer look was taken due to high expectations regarding its speed and robustness. The following description of the registration method used in ShIRT borrows notations from the original user manual. The implementation of the method is available on request to the author and has been developed since a decade.

The algorithm aims at minimizing a cost function Q proportional to the dissimilarity between the images f and $m = \Gamma(g)$, the source image g, deformed by the motion field Γ. The objective function can be written as

$$Q = \sum (f - m)^2 . \tag{8.3}$$

For each given pixel, it is assumed that any difference of intensities between f and m is due to an infinitesimal displacement of the pixel's position. According to this fundamental principle of optical flow, a linear relashionship between the image difference and the horizontal and vertical displacements Δx and Δy can then be written as

$$f - m = \frac{\Delta x}{2}\left(\frac{\partial f}{\partial x} + \frac{\partial m}{\partial x}\right) + \frac{\Delta y}{2}\left(\frac{\partial f}{\partial y} + \frac{\partial m}{\partial y}\right). \tag{8.4}$$

The sum of squared differences used in Q is a simple and appropriate metric for capturing dissimilarity between binary images but tends to emphasize small relative differences between bright pixels. To overcome this problem, both source and target image are converted to binary images f_b and m_b, respectively, prior to registration.

The conversion to binary images is done by introducing a supplemental dimension for the intensity, effectively casting a 2D registration problem between a pair of planar images to a registration of volumetric 3D binary images:

$$f_b - m_b = \frac{\Delta x}{2}\left(\frac{\partial f_b}{\partial x} + \frac{\partial m_b}{\partial x}\right) + \frac{\Delta y}{2}\left(\frac{\partial f_b}{\partial y} + \frac{\partial m_b}{\partial y}\right) + \frac{\Delta s}{2}\left(\frac{\partial f_b}{\partial s} + \frac{\partial m_b}{\partial s}\right). \tag{8.5}$$

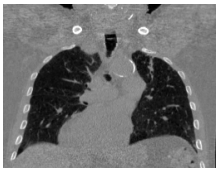

The new dimension for the intensity channel is denoted by s. Since the intensity channel depends on the specific range of pixel's values, it is appreciable to make this dimension independent from the spatial channels x and y. Therefore the difference between intensity channels is modelled as $\Delta s = s\Delta\alpha + \Delta\beta$.

The difference for continuous intensity images can now be expressed by integrating over s the difference between binary images, giving

$$f - m = \frac{\Delta x}{2}\left(\frac{\partial f}{\partial x} + \frac{\partial m}{\partial x}\right) + \frac{\Delta y}{2}\left(\frac{\partial f}{\partial y} + \frac{\partial m}{\partial y}\right) - \frac{\Delta\alpha}{2}(f + m) - \Delta\beta. \tag{8.6}$$

The objective is now to estimate smooth functions to represent the displacements Δx, Δy, $\Delta\alpha$, and $\Delta\beta$. Thus the registration of planar 2D images boils down to the estimation of a smooth 4D function. To represent the deformation, a sparse grid of control points is introduced. For each control point located at the grid vertex (x_i, y_i), the bilinear kernel

$$\phi_i(x, y) = \max\left(0, 1 - \left|\frac{x - x_i}{d}\right|\right) \times \max\left(0, 1 - \left|\frac{y - y_i}{d}\right|\right). \tag{8.7}$$

is used to sample image elements at any given position (x, y).

The radius of the kernel depends on the spacing of control knots. The triangular basis function corresponds to the second order B-spline, many authors do prefer relying on cubic B-spline basis functions for their attractive smoothness and continuity properties. However, to the author's knowledge, the practical relative advantage of cubic over linear B-splines has not yet been evaluated for image registration purpose.

Using such a grid for representing the deformation, the relation between image differences and the displacements of control points can be expressed by

$$\begin{aligned} f - m &= \sum_i a_{xi}\phi_i\left(\frac{\partial f}{\partial x} + \frac{\partial m}{\partial x}\right) \\ &+ \sum_i a_{yi}\phi_i\left(\frac{\partial f}{\partial y} + \frac{\partial m}{\partial y}\right) \\ &- \sum_i a_{\alpha i}\phi_i(f - m) - 2\sum_i a_{\alpha\beta i}\phi_i, \end{aligned} \tag{8.8}$$

where the four scalar parameters a_{xi}, a_{yi}, $a_{\alpha i}$, and $a_{\beta i}$ must be estimated for every control point i.

It is obvious that the number of control points influences the speed of the algorithm as well as the local accuracy of the displacements. If the number of control points is low, there are less computations to be executed. If on the other hand the spacing of these points is small, the displacements estimates becomes more accurate and even very slight motion can be captured.

Using vector and matrix notations, the relation can be written in shorten form:

$$f - m = a^T T, \tag{8.9}$$

where a^T represents the transposed vector of parameters to estimate and the matrix T represents the multiplication of basis functions ϕ_i with sums of partial derivatives.

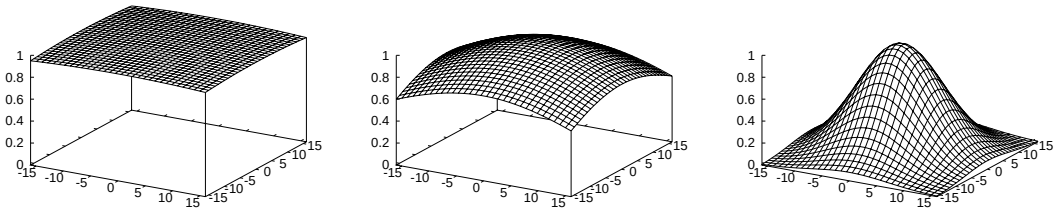

(a) *falloff* $= 10^{-4}$ (b) *falloff* $= 10^{-3}$ (c) *falloff* $= 10^{-2}$

Figure 8.1: Various weightings of the image area surrounding the search block. A larger falloff factors of an exponential distribution allows selecting between uniform constant weighting where every pixel are equally important and point weighting where only the center pixel contributes to the evaluation of local image dissimilarity.

To enforce smoothness, hence, regularity of the deformation, a weighted regularization term is added which includes the square of the Laplacians. This regularization scheme was already proposed in the seminal paper of Horn and Schunk.

The regularized cost function can be expressed by

$$Q = \sum (f - m)^2 + \lambda a^T L^T L a, \tag{8.10}$$

where L stands for a discretized Laplacian operator and λ is a user-defined parameter driving the strength of the regularization term.

In the implementation of ShIRT, the registration problem is iteratively solved by a conjugate gradient (CG) method. The current estimate for the parameters a at iteration $t \geq 1$ is noted by a^t. The accuracy of the estimate is iteratively updated as $a^{t+1} = a^t + \Delta a^t$ with

$$\Delta a^t = \left[T^T T + \lambda L^T L\right]^{-1} \left(T^T (f - m^t) - \lambda L^T L a^t\right). \tag{8.11}$$

8.3 Block Matching

Block matching is a rather simple technique often used for medical image registration besides its application in many video compression schemes and in computer vision (Forsyth and Ponce, 2002). As the name suggests, this technique computes a deformation by matching blocks from a source image g to corresponding blocks in a target image f.

The matching is computed only for several seclected pixels from the source image. Those control points could correspond to specific image features; however, in our implementation, the set of control points are pixels corresponding to vertices of a coarse regular Cartesian grid.

Around each vertex, a block is created with a predefined size and the best matching for this block is searched in the target image in a certain neighborhood. The candidate target blocks are usually only translated to overlap the source block, while in principle, rotations and non-uniform scaling should also be considered to capture arbitrary elastic deformations.

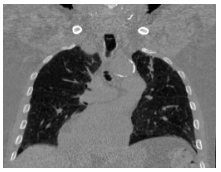

For the present work, the block is round-shaped and the coordinates of the pixels B_i, $\forall i \leq |B|$ belonging to a compact circular support is noted by

$$B \equiv \left\{ (x,y)_i : \|(x,y)_i\| \geq \left\|(x,y)_j\right\|, \quad \forall i > j \right\}, \tag{8.12}$$

where $|B|$ is the number of pixels included in the set B. In a similar way, the search region in the target image is limited to a round neighborhood around the center of the block. This set of displacement vectors N_j, $\forall j \leq |N|$ is also ordered according to magnitudes such that

$$N \equiv \left\{ (u,v)_i : \|(u,v)_i\| \geq \left\|(u,v)_j\right\|, \quad \forall i > j \right\}, \tag{8.13}$$

where $|N|$ is the number of pixels inside the search region N.

If displacements are small, it can be assumed that the larger the magnitude of the displacement is, the less probable a block of better similarity will be found further away from the best match found so far. Therefore, a weighting is introduced within the image dissimilarity metric to control the influence of pixels far away from the block center.

The weights are associated to each pixel of the block B and are precomputed in a look-up table (LUT) using the formula

$$w_i = \exp\left[-\mathit{falloff} \cdot \|B_i\|^2 \right], \quad \forall i \leq |B|\,. \tag{8.14}$$

Furthermore, weights are normalized such that the integral over every pixel of the block equals to one. Thus, normalized weights are finally assigned with the following normalization procedure:

$$w_i \leftarrow \frac{w_i}{\sum_{k \leq |B|} w_k}, \quad \forall i \leq |B|\,. \tag{8.15}$$

The weights follow an exponential function dependent on the squared Euclidean distance from the search center and a constant falloff factor. The spatial distribution of function for different values of *falloff* in a square of 33×33 pixels can be visualized in figure 8.1. It can be seen that the number of pixels with a significant weight decreases with increasing falloff factors, while the shape of the weighting function is almost flat for a small constant.

For computing the dissimilarity between a block extracted from position (x, y) inside the target image f and another block from the source image g, the algorithm tests first if the search block covers image elements which are outside the image borders. Then, the dissimilarity integrated over pixels that belong to the image support is normalized according to the sum of the weightings of the pixels inside the image.

A simple computation of the image distance is used in this work, while multimodal registration requires appropriate image similarity metrics such as the popular mutual information (Pluim *et al.*, 2000, 2003) or the cross correlation (Andronache *et al.*, 2008). The sum of absolute differences (SAD) is used for measur-

ing the dissimilarity such as

$$Q = \frac{1}{W} \sum_{i \leq |B|} w_i \left| f\left((x,y) + B_i\right) - g\left(N_j + (x,y) + B_i\right) \right|, \tag{8.16}$$

where every difference has been weighted. The normalization term is given by

$$W = \sum_{i \leq |B|} w_i. \tag{8.17}$$

Note that if the block is completely inside the image, then $W = 1$ and the evaluation of the normalization term can be ignored.

Additionally, in order to favor small displacements, a shift-variant penalty term dependent on the squared length of displacement vectors is added to the dissimilarity metric. The penalization is weighted by the factor $\lambda \geq 0$ such that

$$Q = \frac{1}{W} \sum_{i \leq |B|} w_i \left| f\left((x,y) + B_i\right) - g\left(N_j + (x,y) + B_i\right) \right| + \lambda \left\| N_j \right\|^2. \tag{8.18}$$

The displacement vector $N_j \in N$ that minimizes the cost function Q is selected by an exhaustive search strategy for every control point located in (x, y). The rationale is that, since the number of candidate displacement vectors $|N|$ is small, an exhaustive search can outperform more complex optimization strategies.

In comparison to the clasical and popular sum of squared differences (SSD) metric, the SAD metric emphasizes much less small relative differences between bright pixels. Many alternative criteria have been proposed for computing image dissimilarities, such as the relative entropy (Kullback-Liebler divergence) that is based on elements of information theory. Future work could evaluate the robustness of the proposed block matching scheme when using different metrics.

In the current implementation, the displacement vectors are estimated on a coarser grid. Using a smaller displacement field decreases the number of computations that is needed and therefore speeds up the registration (Plishker *et al.*, 2007). Additionally, the displacement field is scaled up to the full size using cubic interpolation and a smooth displacement vector field is obtained. Since the motion is computed at a coarser resolution, small local deformations can not be captured (Robinson and Milanfar, 2004).

Computing resources are especially needed for computing the dissimilarity between blocks for each possible displacement vector candidate. The number of blocks to be processed can be reduced further by previously thresholding the image and determining which pixels are close to object borders (Malsch *et al.*, 2006). Another possibility to increase the speed of the algorithm is to alter the search strategy (Zhu and Ma, 2000).

A full search algorithm is used in standard block matching, that means that in a predefined search area every possible displacement candidate is evaluated. In addition, multiresolution image representation (Adelson *et al.*, 1984) can both speed-up the registration process and regularize the results (Bajcsy and Kovacic, 1989; Kostelec *et al.*, 1998).

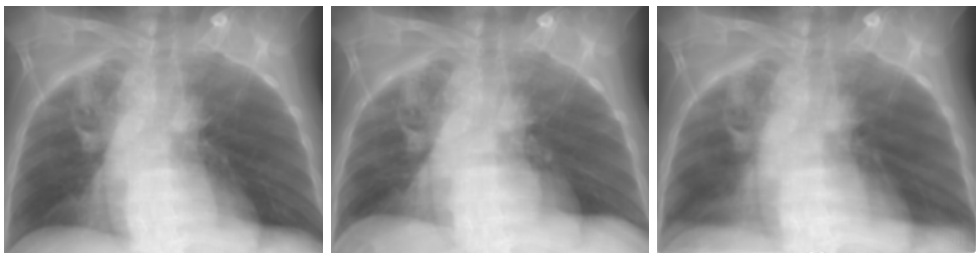

(a) Acquired projection (b) Selected reference (c) Approx. reference

Figure 8.2: Two series of pairs of projections are used for experiments but only the frontal projection is shown as illustration. The sharp acquired projection (a) is registered on either a sharp projection (b) from a selected reference motion state or a more blurry approximate reference projection (c), projected from a scout reconstruction. The approximate projection contains motion blur artifacts that are well visible at the border of the diaphragm.

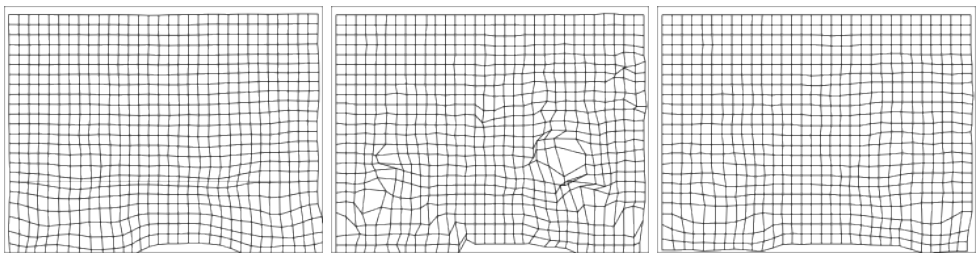

(a) ShIRT (b) Block matching $\lambda = 0$ (c) Block matching $\lambda = 100$

Figure 8.3: Effect of the penalization parameter λ on the regularity of the grid produced by block matching. In comparison to the grid produced by ShIRT (a), the non-penalized block matching scheme produces irregular deformations (b). However, irregularities are largely prevented by using a slight penalization (c) within the image dissimilarity metric.

8.4 Results

Experiments have been conducted to evaluate the impact of various registration algorithms on the quality of motion-compensated image reconstruction. The influence of user-controlable parameters of the registration methods has also been experimented. For instance, the definition of deformation grids and the strength of the penalty term for regularization.

Two set of reference projections have been used for motion estimation: a collection of sharp X-ray images sampled from a selected motion state and a collection of blurry projections sampled from an approximate scout reconstruction without any motion correction. Figure 8.2 shows projections for a specific acquisition angle and figure 8.3 shows typical deformation grids estimated using ShIRT and the block matching method.

In experiments, it has been observed that the deformations estimated using ShIRT are fairly regular and no spurious motion corrupts the results. This comes from the fact that ShIRT is using a multi resolution image pyramid for registration and implicitly ensures smoothness with the additional penalty term that depends on the Laplacian of the deformation grid.

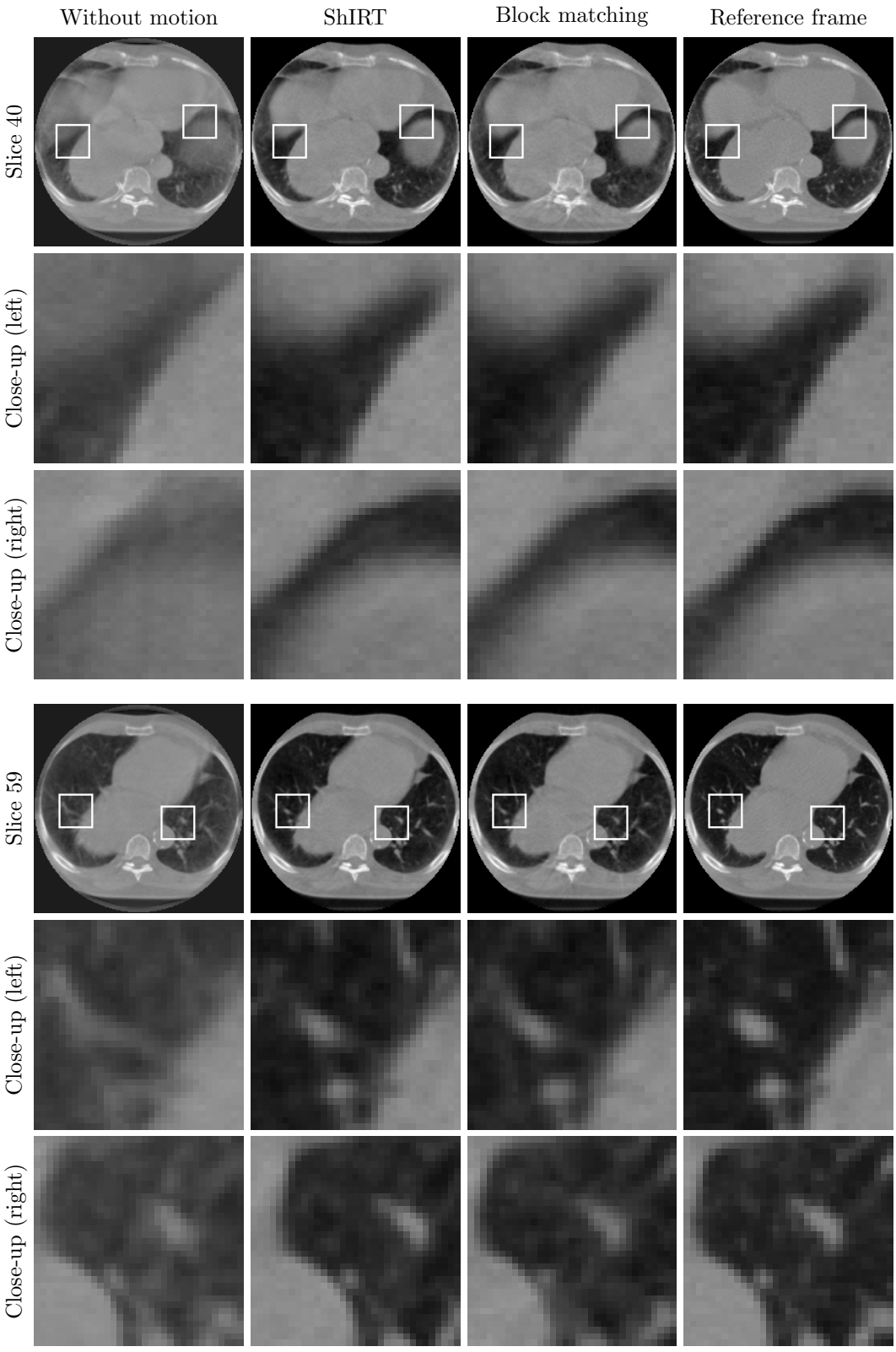

Figure 8.4: Side-by-side comparisons for two selected transversal slices through motion-compensated reconstructions. The deformation is estimated using sharp selected reference projections.

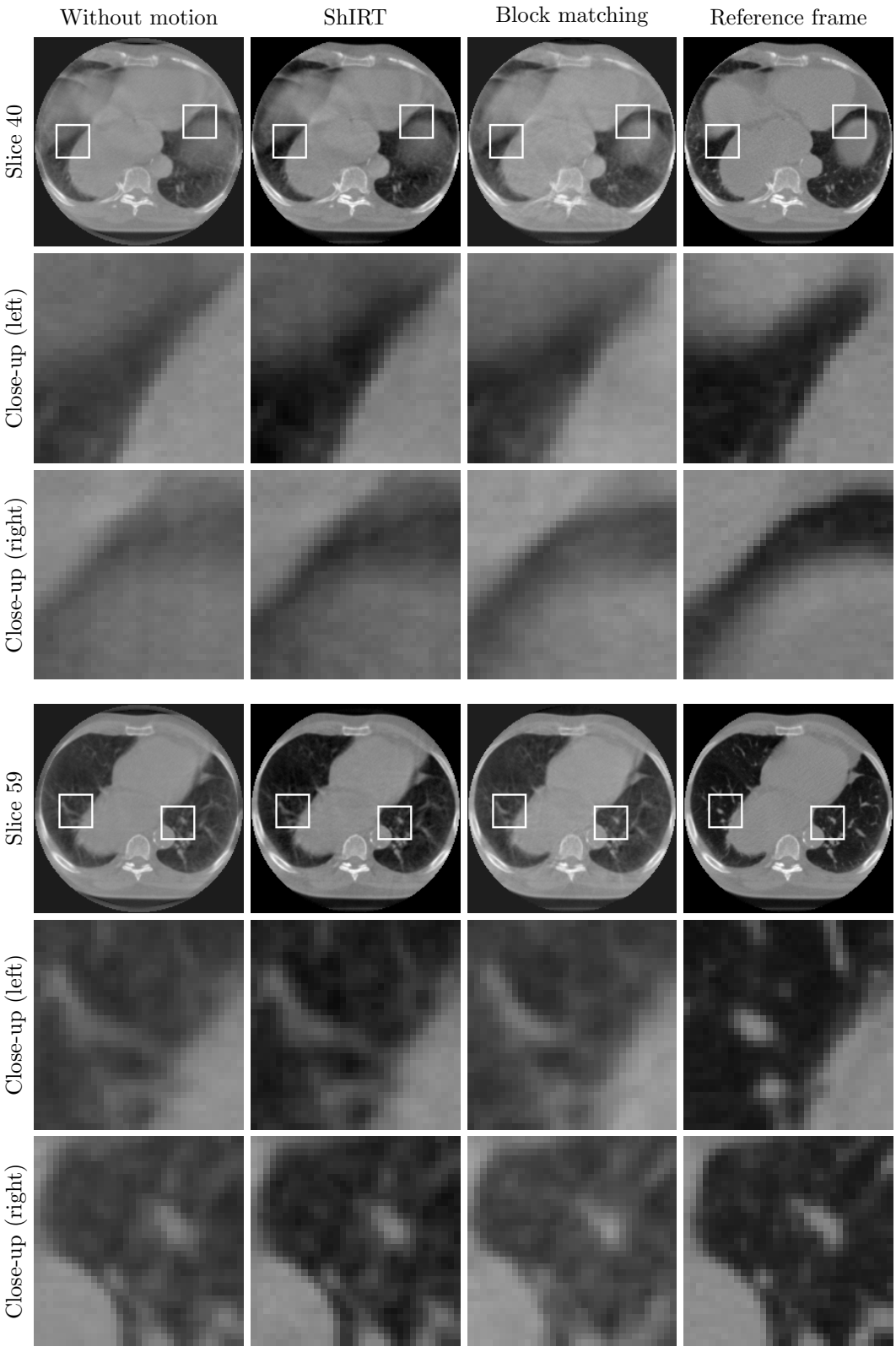

Figure 8.5: Side-by-side comparisons for two selected transversal slices through motion-compensated reconstructions. The deformation is estimated using blurry approximate reference projections.

In contrast, without penalization ($\lambda = 0$), the block matching scheme produces very irregular deformation grids. However, a sligh penalization ($\lambda = 100$) allows the recovering of a grid that visually match the result produced by the more complex registration algorithm implemented in ShIRT.

Figure 8.4 shows the slices 40 and 59, extracted from the volumetric images reconstructed without and with motion compensation when the motion is estimated using the ShIRT optical-flow implementation or the block-matching technique. The similarity with the reference image is striking when using motion compensation. Only slight remaining dissimilarities can be observed in the two selected close-up views. Both ShIRT and block matching result in relatively similar images that compare well with the selected reference frame.

The second experiment considered the more realistic scenario where reference projections are projected from a scout reconstruction corrupted by motion blur artifacts. The corresponding images slices are shown in figure 8.5. In this case, the image improvement is clear, but only partial. In particular, the contrast improvement can especially be appreciated with the ShIRT method while almost any improvement can be seen with the block matching implementation.

The result of this second experiment points out that ultimately, the quality of a motion compensated reconstruction depends on the accuracy of reference projections used for motion estimation (Christensen and Johnson, 2001). For the particular case of blurry reference projections, ShIRT showed its benefits for this more chalenging instance of image registration.

For separation of concerns, no motion segmentation is used and therefore the global motion compensation reconstruction is used, where every voxel is displaced according to its corresponding motion vector estimated in projection space. Very similar results are expected when the compensation is applied only locally, according to the detected motion in image space. Motion detection is a simpler problem than motion estimation.

8.5 Conclusion

In this study, an existing implementation of an optical flow-based approach (ShIRT) and an original implementation of a block matching scheme were presented and evaluated for the purpose of motion estimation in CT. For the experiments, simulated projections of a dynamic phantom obtained from clinical patient data were used. Both algorithms were evaluated in two scenarios.

In the first case, breathing motion was estimated assuming the prior knowledge of sharp reference projections. In the second case, there was no such reference available and the motion was detected by registration of acquired projections with forward projections of an initial, blurred reconstruction.

It was observed that the optical flow algorithm was capable of detecting the motion accurately and produced smooth displacement vector fields if a sharp reference was used. Motion blur artifacts were almost completely retarget from the reconstructed images. However, this algorithm was not well suited for the application on blurred reference projections. The blur in the reconstructed volumes was only slightly reduced, mainly because the amplitude of the detected displacement vectors was systematically too small.

In the case of the known reference, the block matching approach provided also favorable results which were however slightly inferior to the results obtained with ShIRT. To fulfill the requirement of smooth deformations, the block matching approach relies on regularization which was implemented by penalizing large deformations and taking the neighboring displacement vectors into account.

Without known reference, it was observed that the block matching method estimated the motion with more accuracy than the ShIRT tool. It was possible to reduce the blurring perceptibly. The performance of the block matching approach could be improved by optimizing the code such as replacing the exhaustive search scheme by approximations, using parallel implementations and/or GPU acceleration.

Summary and Future Work

A new trend in minimally invasive medical interventions is tomographic soft tissue imaging for tightly coupled diagnosis, therapy planning, and outcome control. The interventional room is typically equipped with a versatile digital radiography system mounted on a robotic C-arm. By programming a circular trajectory for the C-arm, X-ray transmission projections can be acquired at regular angular intervals around the patient. Using computed tomography (CT), a volumetric image can be reconstructed from the set of projections, unveiling the depth of anatomical structures.

During a treatment session, the patient may follow several acquisitions for which he is asked to retain a still position while holding his breath. An acquisition lasts for 10 to 20 seconds for an angular range of about 240 degrees. Unfortunately, uncontrolled patient movements yield inconsistent projections which result in strong image artifacts when using analytical reconstruction methods. For example, such residual motion frequently occurs due to breath-hold failures, intestinal contractions, or nervous shaking.

If breathing occurs during the acquisition, the diaphragm contracts and pulls down the organs to enlarge the thoracic volume. The organ motion is space-variant, only approximately periodic, and mainly axial. In particular, organs can move inside and outside the field of view (FOV) during the acquisition. Therefore, the measured line integrals can be strongly biased and the input projections are *inconsistent*. The correction of non-periodic motion is a challenging problem because neither periodicity nor smoothness in time of the patient motion can be assumed. Therefore, new techniques for the correction of arbitrary motion have been developed in this thesis.

Two main methods have been experimented for improving the quality of static volumetric imaging in CT when motion occurs. The first approach is an iterative image refinement technique based on a pipeline of standard image processing algorithms. This method starts with a regular image reconstruction and therefore, the result is a generalization of the existing image reconstruction solution. Surprising results were obtained but a great number of iterations is required to converge to an acceptable image quality.

A second approach has been less straightforward to develop and was incrementally explored and refined over the four last chapters of this work. First, an initial image is reconstructed from acquired data without any motion correction. This image is likely to contain motion blur artifacts but is nevertheless considered as a

motionless static image of a representative mean motion state. Then, the reconstruction is inverted by computing the forward projection from this reconstructed image. The result is a stack of reference projections, matching the geometry of the input acquired projections.

Once the reference projections are available, a field of displacement vectors is evaluated by elastic image registration for each independent pair of corresponding acquired and reference projections. The output result is a continuous representation of a bijective (invertible) mapping function from acquired projections to reference projections. The computed deformation provides rough information of the patient motion that can be used in addition to the original acquired projections to reconstruct a motion-compensated image.

Early results for two-dimensional imaging and parallel-beam geometry have been obtained from experiments with the mathematical Shepp-Logan phantom. It was found that the method can provide exceptionally accurate images. Therefore, subsequent work has been made to experiment the method on realistic respiratory motion with a moving three-dimensional image derived from a clinical acquisition. Furthermore, this method has been coupled with a motion detection scheme in order to apply the motion correction locally.

Since the motion is perceived and estimated in the two-dimensional space of X-ray projections, an exact recovery of the entire motion information is impossible. The new concept of local motion compensation proposed in this work has proven to be beneficial for avoiding motion corruption that would result from a uniform compensation for each voxel in image space. Furthermore, local motion compensation can potentially save computational resources by skipping the repeated reconstruction of static image regions.

A last step in the development of the second approach has been to challenge the technique on perspective projections from a simulated circular acquisition on a realistic C-arm cone-beam system. New important constraints had to be overcome for enabling a practical motion correction in cone-beam geometry. The main limitation is due to the fact that exact image reconstruction is impossible outside of the central plane. Additionally, the relative small size of digital X-ray detectors induces both axial and lateral data truncations.

To solve issues with data truncation, the SART iterative reconstruction method has been used first to generate a (motion-blurred) volumetric image and its coresponding collection of reference projections. A key property of iterative reconstruction methods is that an artifact-free reconstruction is possible in the region of interest that is observed by every projection. Even with severe data truncations, the obtained reference projections always match exactly the data when no motion is present.

In addition, an experiment comparing various image interpolation models during the backprojection of a FBP reconstruction algorithm is presented in chapter 3. This investigation has emphasized the impact of the less accurate standard bilinear interpolations on image quality. A simple pre-filtering technique has been proposed to improve image sharpness at the cost of only a small performance overhead.

In conclusion, this work proposed several original methods for motion correction in computed tomography. For the first time, the general problem of unstructured (non-periodic) patient's motion is addressed in details. Experiments have been designed to simulate as closely as possible the realistic conditions of an acquisition on

a divergent ray C-arm device, including data truncations and limited frame rate. The new concept of local motion compensation is certainly the major contribution and very encouraging results have been obtained when following this approach.

Future Work

The present thesis reports on results that have been gathered during a three years long research programme. The emphasis of this work was the exploration and the comparison of new original techniques for general motion correction in computed tomography. The most promising solution has been identified as a two-stages scheme based on a prior motion estimation and motion segmentation step, followed by a motion-compensated image reconstruction.

This promising technical approach has been incrementally developed in the four last chapters of the thesis. This work is however still in an intermediary stage on the long way towards a complete solution for the problem. Although promising early results have been demonstrated, important tracks for future work ought to be mentioned.

Validation Using Multiple Datasets

All presented methods have been experimented using either the conventional mathematical Shepp-Logan or a realistic dynamic dataset of the breathing motion acquired for one single patient. It should be stressed that this clinical dynamic image is of exceptional quality and has made possible the experimentation of a close-to-reality scenario. In future, more experiments should be conducted for other sources of patient's motion.

For instance, it would be interesting to evaluate the potential for correction of general abdominal motion such as hiccups or digestive contractions. Validation for various motion scenarios and other anatomical regions would be an interesting future investigation. However only one dataset focusing on the chest motion was available for experiments and modeling the free-breathing motion was a natural choice in this case.

Reconstruction Using Acquired Data

Up to now, the projection data has been sampled from mathematical phantom or a clinical image. Therefore, projection data are already partially corrupted by noise, helical reconstruction artifacts, and remaining motion blur. It would be more convincing to evaluate some of the proposed methods on acquired projection data. It is natural to expect superior results when using directly the acquired projections since the mentioned source of inaccuracies will not be present with real data.

For a fair comparison with the current standard, a motion-compensated reconstruction from acquired data requires to modify the existing image reconstruction software. Unfortunately, this implementation was not available and this evaluation was not initially planned, due to the very exploratory nature of the research project. However, the methods developed in this work have solicited enough interest and a new project started in January 2010 at Philips Research for achieving this goal.

Refining the Motion Segmentation Step

Little time was spent on the development of the image processing chain for motion detection and segmentation. In fact, very satisfactory results have been obtained when using the very simple, even naive, approach of segmentation using a single threshold function. Image segmentation is an important topic in medical imaging and a wealth of publications and alternative methods have been proposed.

In future work, it would be interesting to further refine the quality of the motion segmentation stage. For instance spurious labeling of voxels can arise with independent thresholding of each image element. Another track for improving both accuracy and performances would be performing the segmentation at a lower image definition, since the detection of moving regions do not require a high image definition such as for image reconstruction.

Refining the Motion Estimation Step

When using blurry reference projections for motion estimation, the amplitude of the displacement vectors has the tendency to be underestimated and no significant motion compensation is observed in some part of the image, especially for image elements located far from the central slice. To improve the robustness of motion estimation, one could study the possibility to pre-process images prior to motion estimation by elastic image registration. In the same way, the estimated deformation vector field can be improved by the application of non-linear enhancement filters as a post-processing after elastic image registration.

Note that, if no motion occurred during the acquisition, then the difference between acquired projections and reference projections should be zero. Therefore, the displacements in projection space will also be estimated as zero vectors, resulting in no motion correction when reconstructing again the acquired projections. In this case, the process will converge in only one iteration and reduces to a simple FBP reconstruction. This property ensures that the motion correction workflow is a generalization of the standard reconstruction pipeline.

Profiling and Improving Performances

Since the specific implementations of algorithms were not designed for speed, the evaluation of computational performances has not been tackled in this work. However, it is easy to roughly predict the potential speed of the proposed algorithms. Most of the time spent in a reconstruction method is due to the backprojection and forward projection steps. A scout image must be reconstructed for generating reference projections. The reconstruction is then inverted and the image is reconstructed again for motion detection and for the final motion compensated image.

The minimum computational cost can be roughly evaluated as the cost of three reconstructions and one forward projection, plus the cost of the image registration for motion estimation. Hence, a motion-compensated image reconstruction is approximately four times slower than an existing method, ignoring the cost of image registration. Those expected performances are in fact very encouraging. A modern trend in tomographic image reconstruction is the use of Graphical Processing Units (GPU) for the computation of backprojections and forward projections. Those specialized stream computers demonstrated impressive performances. Furthermore, the

registration of two dimensional images can be realized in a very fast step, in parallel for each pair of projections.

As mentioned above, run-time performance could be improved further by reconstructing a lower resolution scout image for the sole purpose of motion estimation and motion detection. The final reconstruction will then use a lower resolution motion estimate for reconstructing the full-resolution motion-compensated image.

Adaptations to Different Imaging Modalities

While the compensation of patient's motion in slow cone-beam systems was the main motivation for this work, other imaging modalities could benefit from the proposed motion correction methodology. For instance, the "heart creeping" is a common problem in SPECT imaging. During the acquisition of planar views, the myocardial muscle slowly slides up and emission data become inconsistent in this case. The proposed method could track the movement of the myocardium.

Another possible application is the correction of residual motion for helical CT acquisition. Diagnostic CT scanners benefit from a very fast continuous rotation of the slipping ring gantry. On such system it is possible to reconstruct the whole respiratory sequence when data are gated using the respiratory signal. Similarly, cardiac-gated reconstruction is possible when recording the electrocardiogram signal.

Unfortunately, the finite size of gating windows gives a chance for the corruption of projection data from residual motion. Therefore, the principle of motion estimation, detection, and compensation could be applied for the independent reconstruction of each frame of a dynamic image sequence.

Joint Motion Estimation and Image Reconstruction

Image reconstruction using analytical methods was a firm requirement for this work. However, all the proposed methods are in a way iterative. After the motion estimation and motion segmentation steps, a motion-compensated image is reconstructed. From this new static reference image, the estimate of displacement vectors in projection space can be refined further by iterating the whole motion correction procedure.

Future work could investigate the potential of iteratively updating the reference projections during reconstruction and therefore updating accordingly both the estimated motion and the motion segmentation. In this joint motion estimation and segmentation framework, the motion estimation and compensation process would be embedded in a unified motion-compensated iterative reconstruction algorithm.

Bibliography

Aach, T. and Kaup, A., Bayesian algorithms for change detection in image sequences using Markov random fields. *Signal Processing: Image Communication*, volume 7(2), pages 147–160, 1995. Cited on page 68.

Adelson, E. H., Anderson, C. H., Bergen, J. R., Burt, P. J., and Ogden, J. M., Pyramid methods in image processing. *RCA Engineer*, volume 29(6), pages 33–41, 1984. Cited on page 97.

Ahn, S., Fessler, J. A., Blatt, D., and Hero, A. O., Convergent incremental optimization transfer algorithms: Application to tomography. *IEEE Transactions on Medical Imaging*, volume 25(3), pages 283–296, 2006. Cited on page 26.

Andersen, A. H., Algebraic reconstruction in CT from limited views. *IEEE Transactions on Medical Imaging*, volume 8(1), pages 50–55, 1989. Cited on page 23.

Andersen, A. H. and Kak, A. C., Simultaneous algebraic reconstruction technique (SART): A superior implementation of the ART algorithm. *Ultrasonic Imaging*, volume 6(1), pages 81–94, 1984. Cited on pages 23 and 83.

Andronache, A., von Siebenthal, M., Székely, G., and Cattin, P., Non-rigid registration of multi-modal images using both mutual information and cross-correlation. *Medical Image Analysis*, volume 12(1), pages 3–15, 2008. Cited on page 96.

Ashburner, J., A fast diffeomorphic image registration algorithm. *Neuroimage*, volume 38(1), pages 95–113, 2007. Cited on pages 52 and 92.

Bajcsy, R. and Kovacic, S., Multiresolution elastic matching. *Computer Vision, Graphics, and Image Processing*, volume 46(1), pages 1–21, 1989. Cited on page 97.

Barber, D. C. and Hose, D. R., Automatic segmentation of medical images using image registration: Diagnostic and simulation applications. *Journal of Medical Engineering & Technology*, volume 29(2), pages 53–63, 2005. Cited on pages 67, 84, 92, and 93.

Barber, D. C., Oubel, E., Frangi, A. F., and Hose, D. R., Efficient computational fluid dynamics mesh generation by image registration. *Medical Image Analysis*, volume 11(6), pages 648–662, 2007. Cited on pages 84 and 93.

Bartoli, A. and Zisserman, A., Direct estimation of non-rigid registrations. in *British Machine Vision Conference*, volume 2, pages 899–908, 2004. Cited on page 92.

Blinn, J. F., Return of the jaggy. *IEEE Computer Graphics and Applications*, volume 9(2), pages 82–89, 1989a. Cited on pages 28 and 34.

———, What we need around here is more aliasing. *IEEE Computer Graphics and Applications*, volume 9(1), pages 75–79, 1989b. Cited on page 28.

———, What is a pixel? *IEEE Computer Graphics and Applications*, volume 25(5), pages 82–87, 2005. Cited on page 28.

Blu, T., Thévenaz, P., and Unser, M., Linear interpolation revitalized. *IEEE Transactions on Image Processing*, volume 13(5), pages 710–719, 2004. Cited on page 33.

Blume, M., Rafecas, M., Ziegler, S., and Navab, N., Combined motion compensation and reconstruction for PET. in *IEEE Nuclear Science Symposium Conference Record*, pages 5485–5487, 2008. Cited on page 6.

Bonnet, S., Koenig, A., Roux, S., Hugonnard, P., Guillemaud, R., and Grangeat, P., Dynamic X-ray computed tomography. *Proceedings of the IEEE*, volume 91(10), pages 1574–1587, 2003. Cited on page 61.

Brandt, S. S. and Kolehmainen, V., Structure-from-motion without correspondence from tomographic projections by bayesian inversion theory. *IEEE Transactions on Medical Imaging*, volume 26(2), pages 238–248, 2007. Cited on page 8.

Bresenham, J. E., Algorithm for computer control of a digital plotter. *IBM Journal of Research and Development*, volume 4(1), pages 25–30, 1965. Cited on page 28.

Brinks, R., Schretter, C., and Meyer, C., Comparison of maximum-likelihood list-mode reconstruction algorithms in PET. in *IEEE Nuclear Science Symposium and Medical Imaging Conference Record*, volume 5, pages 2801–2803, 2006. Cited on page 28.

Browne, J. and De Pierro, A. B., A row-action alternative to the EM algorithm for maximizing likelihoods in emission tomography. *IEEE Transactions on Medical Imaging*, volume 15(5), pages 687–699, 1996. Cited on page 26.

Brox, T., Bruhn, A., Papenberg, N., and Weickert, J., High accuracy optical flow estimation based on a theory for warping. in *Lecture Notes in Computer Science*, pages 25–36, Springer, 2004. Cited on page 92.

Bruder, H., Maguet, E., Stierstorfer, K., and Flohr, T., Cardiac spiral imaging in computed tomography without ECG using complementary projections for motion detection. in *SPIE Medical Imaging*, volume 5032, pages 1798–1809, 2003. Cited on page 7.

Buck, A. K., Nekolla, S., Ziegler, S., *et al.*, SPECT/CT. *Journal of Nuclear Medicine*, volume 49(8), pages 1305–1319, 2008. Cited on page 2.

Chen, G. H. and Leng, S., A new data consistency condition for fan-beam projection data. *Medical Physics*, volume 32(4), pages 961–967, 2005. Cited on page 7.

Chen, G. H., Tang, J., and Leng, S., Prior image constrained compressed sensing (PICCS): A method to accurately reconstruct dynamic CT images from highly undersampled projection data sets. *Medical Physics*, volume 35(2), pages 660–663, 2008. Cited on page 8.

Chen, G. T. Y., Kung, J. H., and Beaudette, K. P., Artifacts in computed tomography scanning of moving objects. in *Seminars in Radiation Oncology*, volume 14, pages 19–26, 2004. Cited on page 3.

Chen, Z., Efficient block matching algorithm for motion estimation. *International Journal of Signal Processing*, volume 5(2), pages 133–137, 2009. Cited on page 92.

Chiu, Y. H. and Yau, S. F., Tomographic reconstruction of time-varying object from linear time-sequential sampled projections. in *IEEE International Conference on Acoustics, Speech, and Signal Processing*, volume 5, pages 309–312, 1994. Cited on page 7.

Cho, P. S., Johnson, R. H., and Griffin, T. W., Cone-beam CT for radiotherapy applications. *Physics in Medicine and Biology*, volume 40(11), pages 1863–1883, 1995. Cited on page 2.

Christensen, G. E. and Johnson, H. J., Consistent image registration. *IEEE Transactions on Medical Imaging*, volume 20(7), pages 568–582, 2001. Cited on page 101.

Christiaens, M., Sutter, B. D., Bosschere, K. D., Campenhout, J. V., and Lemahieu, I., A fast, cache-aware algorithm for the calculation of radiological paths exploiting subword parallelism. *Journal of Systems Architecture, Special Issue on Parallel Image Processing*, volume 10(45), pages 781–790, 1999. Cited on page 28.

Chun, S. Y. and Fessler, J. A., Regularized methods for topology-preserving smooth nonrigid image registration using B-spline basis. in *IEEE International Symposium on Biomedical Imaging: From Nano to Macro*, pages 1099–1102, 2008. Cited on pages 66 and 92.

———, A simple penalty that encourages local invertibility and considers sliding effects for respiratory motion. in *SPIE Medical Imaging*, volume 7259, pages 72592U–9, 2009a. Cited on pages 65, 66, and 92.

———, A simple regularizer for B-spline nonrigid image registration that encourages local invertibility. *IEEE Journal of Selected Topics in Signal Processing*, volume 3(1), pages 159–169, 2009b. Cited on pages 65, 66, 84, and 92.

Condat, L., Blu, T., and Unser, M., Beyond interpolation: Optimal reconstruction by quasi-interpolation. in *IEEE International Conference on Image Processing*, volume 1, pages 33–36, 2005. Cited on pages 33 and 34.

Cook, R. L., Stochastic sampling in computer graphics. *ACM Transactions on Graphics*, volume 5(1), pages 51–72, 1986. Cited on page 29.

Cover, T. M. and Thomas, J. A., *Elements of information theory*. Wiley-Interscience, 1991. Cited on page 34.

Dalai, M., Leonardi, R., and Migliorati, P., Efficient digital pre-filtering for least-squares linear approximation. in *International Workshop on Visual Content Processing and Representation*, pages 161–169, 2005. Cited on pages 33 and 34.

De Man, B. and Basu, S., Distance-driven projection and backprojection. in *IEEE Nuclear Science Symposium Conference Record*, volume 3, pages 1477–1480, 2002. Cited on page 28.

———, Distance-driven projection and backprojection in three dimensions. *Physics in Medicine and Biology*, volume 49(11), pages 2463–2475, 2004. Cited on page 28.

Defrise, M. and Clack, R., A cone-beam reconstruction algorithm using shift-variant filtering and cone-beam backprojection. *IEEE Transactions on Medical Imaging*, volume 13(1), pages 186–195, 1994. Cited on page 3.

Dempster, A. P., Laird, N. M., and Rubin, D. B., Maximum likelihood from incomplete data via the EM algorithm. *Journal of the Royal Statistical Society. Series B (Methodological)*, volume 39(1), pages 1–38, 1977. Cited on page 24.

Desbat, L., Rit, S., Clackdoyle, R., Mennessier, C., Promayon, E., and Ntalampeki, S., Algebraic and analytic reconstruction methods for dynamic tomography. in *IEEE Engineering in Medicine and Biology Conference*, pages 726–730, 2007a. Cited on page 8.

Desbat, L., Roux, S., and Grangeat, P., Compensation de déformations en tomographie dynamique 3D conique. *Traitement du Signal*, volume 23(5-6), pages 461–472, 2006. Cited on pages 51, 62, and 65.

———, Compensation of some time dependent deformations in tomography. *IEEE Transactions on Medical Imaging*, volume 26(2), pages 261–269, 2007b. Cited on pages 8, 52, 62, 65, 68, and 82.

Dietrich, L., Jetter, S., Tücking, T., Nill, S., and Oelfke, U., Linac-integrated 4D cone beam CT. *Physics in Medicine and Biology*, volume 51(11), pages 2939–2952, 2006. Cited on page 2.

Dold, C., Zaitsev, M., Speck, O., Firle, E., Hennig, J., and Sakas, G., Advantages and limitations of prospective head motion compensation for MRI using an optical motion tracking device. *Academic radiology*, volume 13(9), pages 1093–1103, 2006. Cited on page 6.

Donoho, D. L., Compressed sensing. *IEEE Transactions on Information Theory*, volume 52(4), pages 1289–1306, 2006. Cited on page 8.

Feldkamp, L. A., Davis, L. C., and Kress, J. W., Practical cone-beam algorithm. *Journal of the Optical Society of America*, volume 1(6), pages 612–619, 1984. Cited on pages 18, 41, and 79.

Finch, D. V., Cone-beam reconstruction with sources on a curve. *SIAM Journal on Applied Mathematics*, volume 45(4), pages 665–673, 1985. Cited on page 79.

Forsyth, D. A. and Ponce, J., *Computer vision: A modern approach*. Prentice Hall Professional Technical Reference, 2002. Cited on page 95.

Franz, A., Carlson, I. C., and Renisch, S., An adaptive irregular grid approach using SIFT features for elastic medical image registration. in *Bildverarbeitung für die Medizin*, pages 201–205, 2006. Cited on page 92.

Fulton, R. R., Hutton, B. F., Braun, M., Ardekani, B., and Larkin, R., Use of 3D reconstruction to correct for patient motion in SPECT. *Physics in Medicine and Biology*, volume 39(3), pages 563–574, 1994. Cited on page 6.

Fung, G. S. K., Segars, W. P., Geschwind, J. F. H., Tsui, B. M. W., and Taguchi, K., Effect of respiratory motion on abdominal C-arm CT angiography using the 4D NCAT phantom. in *IEEE Nuclear Science Symposium Conference Record*, volume 6, pages 4536–4538, 2007. Cited on page 4.

Gilland, D. R., Mair, B. A., Bowsher, J. E., and Jaszczak, R. J., Simultaneous reconstruction and motion estimation for gated cardiac ECT. *IEEE Transactions on Nuclear Science*, volume 49(5), pages 2344–2349, 2002. Cited on page 84.

Gilland, D. R., Mair, B. A., and Parker, J. G., Motion estimation for cardiac emission tomography by optical flow methods. *Physics in Medicine and Biology*, volume 53(11), pages 2991–3006, 2008. Cited on pages 6 and 84.

Gordon, R., Bender, R., and Herman, G. T., Algebraic reconstruction techniques (ART) for three-dimensional electron microscopy and X-ray photography. *Journal of Theoretical Biology*, volume 29(3), pages 471–481, 1970. Cited on page 21.

Grangeat, P., Mathematical framework of cone beam 3D reconstruction via the first derivative of the Radon transform. in *Lecture Notes in Mathematics*, volume 1497, pages 66–97, Springer, 1991. Cited on page 2.

Grangeat, P., Koenig, A., Rodet, T., and Bonnet, S., Theoretical framework for a dynamic cone-beam reconstruction algorithm based on a dynamic particle model. *Physics in Medicine and Biology*, volume 47(15), pages 2611–2625, 2002. Cited on page 61.

Hansis, E., Schäfer, D., Dössel, O., and Grass, M., Evaluation of iterative sparse object reconstruction from few projections for 3-D rotational coronary angiography. *IEEE Transactions on Medical Imaging*, volume 27(11), pages 1548–1555, 2008a. Cited on page 7.

———, Projection-based motion compensation for gated coronary artery reconstruction from rotational X-ray angiograms. *Physics in Medicine and Biology*, volume 53(14), pages 3807–3820, 2008b. Cited on page 7.

Herman, G. T. and Meyer, L. B., Algebraic reconstruction techniques can be made computationally efficient. *IEEE Transactions on Medical Imaging*, volume 12(3), pages 600–609, 1993. Cited on page 24.

Hill, D. L. G., Batchelor, P. G., Holden, M., and Hawkes, D. J., Medical image registration. *Physics in Medicine and Biology*, volume 46(3), pages 1–45, 2001. Cited on pages 8 and 91.

Horbelt, S., Liebling, M., and Unser, M., Filter design for filtered back-projection guided by the interpolation model. in *SPIE Medical Imaging*, volume 4684, pages 806–813, 2002. Cited on page 31.

Horn, B. K. P. and Schunck, B. G., Determining optical flow. *Artificial Intelligence*, volume 17(1), pages 185–203, 1981. Cited on pages 67, 84, and 92.

Hounsfield, G. N., Computerized transverse axial scanning (tomography): Part 1. description of system. *British Journal of Radiology*, volume 46(552), pages 1016–1022, 1973. Cited on page 3.

Hsiao, I.-T., Rangarajan, A., Khurd, P., and Gindi, G., An accelerated convergent ordered subsets algorithm for emission tomography. *Physics in Medicine and Biology*, volume 49(11), pages 2145–2156, 2004. Cited on page 26.

Hsieh, J., Adaptive motion artifact suppression in CT. in *SPIE Medical Imaging*, volume 2847, pages 429–427, 1996. Cited on page 39.

———, Two-pass algorithm for cone beam reconstruction. in *SPIE Medical Imaging*, volume 3979, pages 533–540, 2000. Cited on pages 21, 39, and 41.

———, *Computed tomography – principles, design, artifacts, and recent advances*. SPIE Press, Bellingham, Washington, 2003. Cited on page 21.

Hsieh, J., Molthen, R. C., Dawson, C. A., and Johnson, R. H., An iterative approach to the beam hardening correction in cone beam CT. *Medical Physics*, volume 27(1), pages 23–29, 2000. Cited on page 13.

Hu, H., An improved cone-beam reconstruction algorithm for the circular orbit. *Scanning*, volume 18(8), pages 572–581, 1996. Cited on pages 21 and 80.

Hudson, H. M. and Larkin, R. S., Accelerated image reconstruction using ordered subsets of projection data. *IEEE Transactions on Medical Imaging*, volume 13(4), pages 601–609, 1994. Cited on page 26.

Isola, A. A., Ziegler, A., Köhler, T., Niessen, W. J., and Grass, M., Motion-compensated iterative cone-beam CT image reconstruction with adapted blobs as basis functions. *Physics in Medicine and Biology*, volume 53(23), pages 6777–6797, 2008. Cited on page 62.

Jacobs, F., Sundermann, E., De Sutter, B., Christiaens, M., and Lemahieu, I., A fast algorithm to calculate the exact radiological path through a pixel or voxel space. *Journal of Computing and Information Technology*, volume 6(1), pages 89–94, 1998. Cited on page 28.

Jaffray, D. A. and Siewerdsen, J. H., Cone-beam computed tomography with a flat-panel imager: Initial performance characterization. *Medical Physics*, volume 27(6), pages 1311–1323, 2000. Cited on pages 1 and 13.

Jaffray, D. A., Siewerdsen, J. H., Wong, J. W., and Martinez, A. A., Flat-panel cone-beam computed tomography for image-guided radiation therapy. *International Journal of Radiation Oncology Biology Physics*, volume 53(5), pages 1337–1349, 2002. Cited on pages 2 and 40.

Jain, J. R. and Jain, A. K., Displacement measurement and its application in interframe image coding. *IEEE Transactions on Communications*, volume 29(12), pages 1799–1808, 1981. Cited on page 92.

Jiang, M. and Wang, G., Convergence of the simultaneous algebraic reconstruction technique (SART). *IEEE Transactions on Image Processing*, volume 12(8), pages 957–961, 2003. Cited on page 23.

Jiangsheng, Y., Weiguo, L., Jian, L., Gene, G., and Zhengrong, L., Image matching for translation, rotation and uniform scaling by the Radon transform. in *IEEE International Conference on Image Processing*, volume 1, pages 847–851, 1998. Cited on page 92.

Joseph, P. M., An improved algorithm for reprojecting rays through pixel images. *IEEE Transactions on Medical Imaging*, volume 1(3), pages 192–197, 1982. Cited on page 27.

Kabus, S., Netsch, T., Fischer, B., and Modersitzki, J., B-spline registration of 3D images with Levenberg-Marquardt optimization. in *SPIE Medical Imaging*, volume 5370, pages 304–313, 2004. Cited on page 92.

Kaczmarz, S., Angenäherte auflösung von systemen linearer gleichungen. *Bulletin International de l'Academie Polonaise des Sciences et des Lettres, series A*, volume 35, pages 335–357, 1937. Cited on page 21.

Kak, A. C. and Slaney, M., *Principles of computerized tomographic imaging*. IEEE Press, New York, 1988. Cited on pages 7, 41, and 62.

Kalender, W. A., X-ray computed tomography. *Physics in Medicine and Biology*, volume 51(13), pages 29–43, 2006. Cited on page 1.

Kamphuis, C. and Beekman, F. J., Accelerated iterative transmission CT reconstruction using an ordered subsets convex algorithm. *IEEE Transactions on Medical Imaging*, volume 17(6), pages 1101–1105, 1998. Cited on page 26.

Katsevich, A., A general scheme for constructing inversion algorithms for cone beam CT. *International Journal of Mathematics and Mathematical Sciences*, volume 21, pages 1305–1321, 2003. Cited on page 3.

———, Motion compensated local tomography. *Inverse Problems*, volume 24(4), pages 5012–21, 2008. Cited on pages 8 and 68.

Klein, S., Staring, M., and Pluim, J. P. W., Evaluation of optimization methods for nonrigid medical image registration using mutual information and B-splines. *IEEE Transactions on Image Processing*, volume 16(12), pages 2879–2890, 2007. Cited on page 92.

Köhler, T., A projection access scheme for iterative reconstruction based on the golden section. in *IEEE Nuclear Science Symposium Conference Record*, volume 6, pages 3961–3965, 2004. Cited on page 24.

Köhler, T., Turbell, H., and Grass, M., Efficient forward projection through discrete data sets using tri-linear interpolation. in *IEEE Nuclear Science Symposium Conference Record*, volume 2, pages 113–115, 2000. Cited on page 28.

Kostelec, P. J., Weaver, J. B., and Healy, Jr, D. M., Multiresolution elastic image registration. *Medical Physics*, volume 25(9), pages 1593–1604, 1998. Cited on page 97.

Kumar, A., Tannenbaum, A. R., and Balas, G. J., Optical flow: A curve evolution approach. *IEEE Transactions on Image Processing*, volume 5(4), pages 598–610, 1996. Cited on page 92.

Lange, K. and Carson, R., EM reconstruction algorithms for emission and transmission tomography. *Journal of Computer Assisted Tomography*, volume 8(2), pages 306–316, 1984. Cited on page 24.

Lange, K. and Fessler, J. A., Globally convergent algorithms for maximum a posteriori transmission tomography. *IEEE Transactions on Image Processing*, volume 4(10), pages 1430–1438, 1995. Cited on page 26.

Lauritsch, G., Boese, J., Wigstrom, L., Kemeth, H., and Fahrig, R., Towards cardiac C-arm computed tomography. *IEEE Transactions on Medical Imaging*, volume 25(7), pages 922–934, 2006. Cited on page 7.

Lehmann, T. M., Gonner, C., and Spitzer, K., Survey: Interpolation methods in medical image processing. *IEEE Transactions on Medical Imaging*, volume 18(11), pages 1049–1075, 1999. Cited on page 32.

Leng, S., Nett, B., Speidel, M., and Chen, G. H., Motion artifact reduction in fan-beam and cone-beam computed tomography via the fan-beam data consistency condition (FDCC). in *SPIE Medical Imaging*, volume 6510, pages 65101W–13, 2007. Cited on page 7.

Leng, S., Zambelli, J., Tolakanahalli, R., Nett, B., Munro, P., Star-Lack, J., Paliwal, B., and Chen, G. H., Streaking artifacts reduction in four-dimensional cone-beam computed tomography. *Medical Physics*, volume 35(10), pages 4649–59, 2008. Cited on page 7.

Lewitt, R. M., Alternatives to voxels for image representation in iterative reconstruction algorithms. *Physics in Medicine and Biology*, volume 37(3), pages 705–716, 1992. Cited on page 28.

Li, T., Schreibmann, E., Yang, Y., and Xing, L., Motion correction for improved target localization with on-board cone-beam computed tomography. *Physics in Medicine and Biology*, volume 51(2), pages 253–267, 2006a. Cited on page 8.

Li, T., Xing, L., Munro, P., McGuinness, C., Chao, M., Yang, Y., Loo, B., and Koong, A., Four-dimensional cone-beam computed tomography using an on-board imager. *Medical Physics*, volume 33(10), pages 3825–33, 2006b. Cited on page 8.

Lin, W. T., A motion compensation algorithm for arbitrary translation of CT objects. in *SPIE Image Processing*, volume 2167, pages 743–754, 1994. Cited on pages 7, 39, and 67.

Linney, N. C. and Gregson, P. H., Organ motion detection in CT images using opposite rays in fan-beam projection systems. *IEEE Transactions on Medical Imaging*, volume 20(11), pages 1109–1122, 2001. Cited on pages 7, 39, and 67.

Livieratos, L., Stegger, L., Bloomfield, P. M., Schafers, K., Bailey, D. L., and Camici, P. G., Rigid-body transformation of list-mode projection data for respiratory motion correction in cardiac PET. *Physics in Medicine and Biology*, volume 50(14), pages 3313–3322, 2005. Cited on page 6.

Long, Y., Fessler, J. A., and Balter, J. M., A 3D forward and back-projection method for X-ray CT using separable footprint. in *International Meeting on Fully Three-Dimensional Image Reconstruction in Radiology and Nuclear Medicine*, pages 146–149, 2009. Cited on page 28.

Lu, W. and Mackie, T. R., Tomographic motion detection and correction directly in sinogram space. *Physics in Medicine and Biology*, volume 47(8), pages 1267–1284, 2002. Cited on page 7.

Maintz, J. and Viergever, M., A survey of medical image registration. *Medical Image Analysis*, volume 2(1), pages 1–36, 1998. Cited on pages 8 and 91.

Malsch, U., Thieke, C., Huber, P. E., and Bendl, R., An enhanced block matching algorithm for fast elastic registration in adaptive radiotherapy. *Physics in Medicine and Biology*, volume 51(19), pages 4789–4806, 2006. Cited on pages 92 and 97.

Malvar, H. S. and Staelin, D. H., Optimal FIR pre- and postfilters for decimation and interpolation of random signals. *IEEE Transactions on Communications*, volume 36(1), pages 67–74, 1988. Cited on page 32.

Manduca, A., Lake, D. S., Khaylova, N., and Ehman, R. L., Image-space automatic motion correction for MRI images. in *SPIE Medical Imaging*, volume 5370, pages 390–397, 2004. Cited on page 6.

Matej, S. and Lewitt, R. M., Efficient 3D grids for image reconstruction using spherically-symmetric volume elements. *IEEE Transactions on Nuclear Science*, volume 42(4), pages 1361–1370, 1995. Cited on page 28.

Mather, G., *Foundations of perception*. Psychology Press, 2006. Cited on page 53.

Milanfar, P., A model of the effect of image motion in the Radon transform domain. *IEEE Transactions on Image Processing*, volume 8(9), pages 1276–1281, 1999. Cited on pages 55, 62, and 69.

MITCHELL, D. P. AND NETRAVALI, A. N., Reconstruction filters in computer-graphics. *ACM SIGGRAPH Computer Graphics*, volume 22(4), pages 221–228, 1988. Cited on page 34.

NING, R., TANG, X., AND CONOVER, D., X-ray scatter correction algorithm for cone beam CT imaging. *Medical Physics*, volume 31(5), pages 1195–1202, 2004. Cited on page 13.

PACK, J. D. AND NOO, F., Dynamic computed tomography with known motion field. in *SPIE Medical Imaging*, volume 5370, pages 2097–2104, 2004. Cited on page 7.

PAN, X., SIDKY, E. Y., AND VANNIER, M., Why do commercial CT scanners still employ traditional filtered back-projection for image reconstruction? *Inverse Problems*, volume 25(12), pages 1–36, 2009. Cited on page 21.

PLISHKER, W., DANDEKAR, O., BHATTACHARYYA, S., AND SHEKHAR, R., A taxonomy for medical image registration acceleration techniques. in *IEEE/NIH Life Science Systems and Applications Workshop*, pages 160–163, 2007. Cited on page 97.

PLUIM, J. P. W., ANTOINE MAINTZ, J. B., AND VIERGEVER, M. A., Interpolation artefacts in mutual information-based image registration. *Computer Vision and Image Understanding*, volume 77(2), pages 211–232, 2000. Cited on page 96.

PLUIM, J. P. W., MAINTZ, J. B. A., AND VIERGEVER, M. A., Mutual information based registration of medical images: A survey. *IEEE Transactions on Medical Imaging*, volume 22(8), pages 986–1004, 2003. Cited on page 96.

PRICE, J. R. AND HAYES, III, M. H., Optimal prefiltering for improved image interpolation. in *Asilomar Conference on Signals, Systems & Computers*, volume 2, pages 959–963, 1998. Cited on page 33.

QIAO, F., PAN, T., CLARK, J. W., AND MAWLAWI, O. R., Region of interest motion compensation for PET image reconstruction. *Physics in Medicine and Biology*, volume 52(10), pages 2675–2689, 2007. Cited on page 6.

RADON, J., On the determination of functions from their integral values along certain manifolds. *IEEE Transactions on Medical Imaging*, volume 5(4), pages 170–176, 1986. Cited on page 13.

RINKEL, J., GERFAULT, L., ESTEVE, F., AND DINTEN, J. M., A new method for X-ray scatter correction. *Physics in Medicine and Biology*, volume 52(15), pages 4633–4652, 2007. Cited on page 13.

RIT, S., SARRUT, D., AND DESBAT, L., Comparison of analytic and algebraic methods for motion-compensated cone-beam CT reconstruction of the thorax. *IEEE Transactions on Medical Imaging*, volume 28(10), pages 1513–1525, 2009. Cited on page 8.

RITCHIE, C. J., CRAWFORD, C. R., GODWIN, J. D., AND KING, K. F., Correction of computed tomography motion artifacts using pixel-specific back-projection. *IEEE Transactions on Medical Imaging*, volume 15(3), pages 333–342, 1996. Cited on page 68.

RITCHIE, C. J., GOODWIN, D., CRAWFORD, C. R., STANFORD, W., ANNO, H., AND KIM, Y., Minimum scan speeds for suppression of motion artifacts in CT. *Radiology*, volume 185(1), pages 37–42, 1992. Cited on page 7.

RITCHIE, C. J., HSIEH, J., GARD, M. F., GODWIN, J. D., KIM, Y., AND CRAWFORD, C. R., Predictive respiratory gating: A new method to reduce motion artifacts on CT scans. *Radiology*, volume 190(3), pages 847–852, 1994. Cited on page 7.

Robertson, D. D., Weiss, P. J., Fishman, E. K., Magid, D., and Walker, P. S., Evaluation of CT techniques for reducing artifacts in the presence of metallic orthopedic implants. *Journal of computer assisted tomography*, volume 12(2), pages 236–241, 1988. Cited on page 13.

Robinson, D. and Milanfar, P., Fundamental performance limits in image registration. *IEEE Transactions on Image Processing*, volume 13(9), pages 1185–1199, 2004. Cited on page 97.

Rohkohl, C., Lauritsch, G., Prümmer, M., Boese, J., and Hornegger, J., Towards 4-D cardiac reconstruction without ECG and motion periodicity using C-arm CT. in *International Meeting on Fully Three-Dimensional Image Reconstruction in Radiology and Nuclear Medicine*, pages 323–326, 2009a. Cited on page 7.

Rohkohl, C., Lauritsch, G., Prümmer, M., and Hornegger, J., Interventional 4-D motion estimation and reconstruction of cardiac vasculature without motion periodicity assumption. in *Medical Image Computing and Computer-Assisted Intervention*, volume 5761, pages 132–139, 2009b. Cited on page 7.

Rösch, P., Netsch, T., Quist, M., and Weese, J., 3D respiratory motion compensation by template propagation. in *Medical Image Computing and Computer-Assisted Intervention*, volume 2, pages 639–646, 2002. Cited on page 92.

Rose, G., Wiegert, J., Schäfer, D., Fiedler, K., Conrads, N., Timmer, J., Rasche, V., Noordhoek, N., Klotz, E., and Koppe, R., Image quality of flat-panel cone beam CT. in *SPIE Medical Imaging*, volume 5030, pages 677–683, 2003. Cited on pages 1 and 40.

Roux, S., Desbat, L., Koenig, A., and Grangeat, P., Exact reconstruction in 2D dynamic CT: Compensation of time-dependent affine deformations. *Physics in Medicine and Biology*, volume 49(11), pages 2169–2182, 2004. Cited on pages 8, 51, 62, 68, 79, and 82.

Rueckert, D., Sonoda, L. I., Hayes, C., Hill, D. L. G., Leach, M. O., and Hawkes, D. J., Nonrigid registration using free-form deformations: Application to breast MR images. *IEEE Transactions on Medical Imaging*, volume 18(8), pages 712–721, 1999. Cited on page 91.

Schäfer, D., Borgert, J., Rasche, V., and Grass, M., Motion-compensated and gated cone beam filtered back-projection for 3-D rotational X-ray angiography. *IEEE Transactions on Medical Imaging*, volume 25(7), pages 898–906, 2006. Cited on page 80.

Schomberg, H., van de Haar, P., and Baaten, W., Cone-beam CT using a C-arm system as front end and a spherical spiral as source trajectory. in *SPIE Medical Imaging*, volume 7258, pages 72580F–12, 2009. Cited on pages 18 and 80.

Schretter, C., A fast tube of response ray-tracer. *Medical Physics*, volume 33(12), pages 4744–4748, 2006. Cited on pages 28, 47, and 67.

———, Improving image quality in computed tomography by motion estimation and compensation. in *IEEE EMBS International Summer School on Biomedical Imaging, Berder, France, June 20–28*, 2008. Cited on page 51.

Schretter, C., Neukirchen, C., Bertram, M., and Rose, G., Correction of some time-dependent deformations in parallel-beam computed tomography. in *IEEE International Symposium on Biomedical Imaging: From Nano to Macro*, pages 764–767, 2008. Cited on pages 51 and 62.

Schretter, C., Neukirchen, C., Rose, G., and Bertram, M., Image-based iterative compensation of motion artifacts in computed tomography. in *SPIE Medical Imaging*, volume 7258, pages 72581W–8, 2009a. Cited on page 39.

———, Local correction of non-periodic motion in computed tomography. in *SPIE Medical Imaging*, volume 7258, pages 72582M–12, 2009b. Cited on page 61.

———, Optimal pre-filtering for linear interpolation in computed tomography. in *Second Workshop on High Performance Image Reconstruction (HPIR)*, pages 29–32, 2009c. Cited on page 31.

Schretter, C., Pilatus, F., Rose, G., Aach, T., and Bertram, M., Optical flow motion estimation for approximate motion compensation in cone-beam CT. in *International Meeting on Fully Three-Dimensional Image Reconstruction in Radiology and Nuclear Medicine*, pages 327–330, 2009d. Cited on page 79.

Schretter, C., Rose, G., and Bertram, M., Image-based iterative compensation of motion artifacts in computed tomography. *Medical Physics*, volume 36(11), pages 5323–5330, 2009e. Cited on page 39.

Shannon, C. E., Communication in the presense of noise. *Proceedings of the Institute of Radio Engineers*, volume 37(1), pages 10–21, 1949. Cited on page 34.

Shepp, L. A. and Logan, B. F., The Fourier reconstruction of a head section. *IEEE Transactions on Nuclear Sciences*, volume 21(3), pages 21–43, 1974. Cited on page 17.

Shepp, L. A. and Vardi, Y., Maximum likelihood reconstruction for emission tomography. *IEEE Transactions on Medical Imaging*, volume 1(2), pages 113–122, 1982. Cited on pages 24 and 26.

Siddon, R., Fast calculation of the exact radiological path length for a three-dimensional CT array. *Medical Physics*, volume 12(2), pages 252–257, 1985. Cited on page 27.

Smith, B. D., Image reconstruction from cone-beam projections: Necessary and sufficient conditions and reconstruction methods. *IEEE Transactions on Medical Imaging*, volume 4(1), pages 14–25, 1985. Cited on page 18.

Sonke, J. J., Zijp, L., Remeijer, P., and van Herk, M., Respiratory correlated cone beam CT. *Medical Physics*, volume 32(4), pages 1176–86, 2005. Cited on pages 7 and 61.

Speck, O., Hennig, J., and Zaitsev, M., Prospective real-time slice-by-slice motion correction for fMRI in freely moving subjects. *Magnetic Resonance Materials in Physics, Biology and Medicine*, volume 19(2), pages 55–61, 2006. Cited on page 6.

Srámek, M. and Kaufman, A. E., Object voxelization by filtering. in *IEEE Symposium on Volume Visualization*, pages 111–118, 1998. Cited on page 53.

———, Alias-free voxelization of geometric objects. *IEEE Transactions on Visualization and Computer Graphics*, volume 5(3), pages 251–267, 1999. Cited on page 53.

Srinivas, C. and Costa, M. H. M., Motion-compensated CT image reconstruction. in *IEEE International Conference on Image Processing*, volume 2, pages 849–853, 1994. Cited on page 7.

Staring, M., Klein, S., and Pluim, J. P. W., A rigidity penalty term for nonrigid registration. *Medical Physics*, volume 34(11), pages 4098–4108, 2007. Cited on page 92.

Strohmer, T. and Vershynin, R., A randomized Kaczmarz algorithm with exponential convergence. *Journal of Fourier Analysis and Applications*, volume 15(2), pages 262–278, 2009. Cited on page 24.

Sunnegardh, J. and Danielsson, P. E., A new anti-aliased projection operator for iterative CT reconstruction. in *International Meeting on Fully Three-Dimensional Image Reconstruction in Radiology and Nuclear Medicine*, pages 124–127, 2007. Cited on page 28.

Taguchi, K. and Kudo, H., Motion compensated fan-beam reconstruction for nonrigid transformation. *IEEE Transactions on Medical Imaging*, volume 27(7), pages 907–917, 2008a. Cited on page 8.

———, A simple motion tracking backprojection for a class of affine transformation. in *SPIE Medical Imaging*, volume 6913, pages 69131V–8, 2008b. Cited on page 80.

Thévenaz, P., Blu, T., and Unser, M., Interpolation revisited. *IEEE Transactions on Medical Imaging*, volume 19(7), pages 739–758, 2000. Cited on pages 33 and 42.

Thibault, J. B., Sauer, K. D., Bouman, C. A., and Hsieh, J., A three-dimensional statistical approach to improved image quality for multislice helical CT. *Medical Physics*, volume 34(11), pages 4526–4544, 2007. Cited on page 28.

Thirion, J. P., Image matching as a diffusion process: An analogy with Maxwell's demons. *Medical Image Analysis*, volume 2(3), pages 243–260, 1998. Cited on page 92.

Trummer, M. R., A note on the ART of relaxation. *Computing*, volume 33(3), pages 349–352, 1984. Cited on page 24.

Turbell, H., *Cone-beam reconstruction using filtered backprojection*. Ph.D. thesis, Linköping University, Sweden, SE-581 83 Linköping, Sweden, 2001, dissertation No. 672, ISBN 91-7219-919-9. Cited on pages 41 and 62.

Tuy, H. K., An inversion formula for cone-beam reconstruction. *SIAM Journal on Applied Mathematics*, volume 43(3), pages 546–552, 1983. Cited on pages 18 and 79.

Unser, M., Splines: A perfect fit for signal and image processing. *IEEE Signal Processing Magazine*, volume 16(6), pages 22–38, 1999. Cited on pages 33, 42, and 91.

———, Sampling – 50 years after Shannon. *Proceedings of the IEEE*, volume 88(4), pages 569–587, 2000. Cited on pages 33, 34, 42, and 91.

Vedam, S. S., Keall, P. J., Kini, V. R., Mostafavi, H., Shukla, H. P., and Mohan, R., Acquiring a four-dimensional computed tomography dataset using an external respiratory signal. *Physics in Medicine and Biology*, volume 48(1), pages 45–62, 2003. Cited on page 7.

Weiskopf, N., Sitaram, R., Josephs, O., Veit, R., Scharnowski, F., Goebel, R., Birbaumer, N., Deichmann, R., and Mathiak, K., Real-time functional magnetic resonance imaging: methods and applications. *Magnetic resonance imaging*, volume 25(6), pages 989–1003, 2007. Cited on page 6.

Willis, P. N. and Bresler, Y., Optimal scan for time-varying tomography – i. theoretical analysis and fundamental limitations. *IEEE Transactions on Medical Imaging*, volume 4(5), pages 642–653, 1995a. Cited on page 7.

———, Optimal scan for time-varying tomography – ii. efficient design and experimental validation. *IEEE Transactions on Medical Imaging*, volume 4(5), pages 654–666, 1995b. Cited on page 7.

Wu, X., An efficient antialiasing technique. in *Conference on Computer Graphics and Interactive Techniques*, pages 143–152, 1991. Cited on page 28.

Xu, F. and Mueller, K., A comparative study of popular interpolation and integration methods for use in computed tomography. in *IEEE International Symposium on Biomedical Imaging: From Nano to Macro*, pages 1252–1255, 2006. Cited on pages 27, 32, and 42.

Yang, D., Lu, W., Low, D. A., Deasy, J. O., Hope, A. J., and El Naqa, I., 4D-CT motion estimation using deformable image registration and 5D respiratory motion modeling. *Medical Physics*, volume 35(10), pages 4577–90, 2008. Cited on page 61.

Yu, H. and Wang, G., Data consistency based rigid motion artifact reduction in fan-beam CT. *IEEE Transactions on Medical Imaging*, volume 26(2), pages 249–260, 2007. Cited on pages 7 and 62.

Yu, H., Wei, Y., Hsieh, J., and Wang, G., Data consistency based translational motion artifact reduction in fan-beam CT. *IEEE Transactions on Medical Imaging*, volume 25(6), pages 792–803, 2006. Cited on pages 7 and 62.

Zbijewski, W. and Beekman, F. J., Characterization and suppression of edge artefacts. *Physics in Medicine and Biology*, volume 49(1), pages 145–157, 2004. Cited on page 28.

———, Comparison of methods for suppressing edge artefacts. *Physics in Medicine and Biology*, volume 51(7), pages 1877–1889, 2006. Cited on page 28.

Zeng, G. L. and Gullberg, G. T., Unmatched projector/backprojector pairs in an iterative reconstruction algorithm. *IEEE Transactions on Medical Imaging*, volume 19(5), pages 548–555, 2000. Cited on page 32.

Zeng, R., Fessler, J. A., and Balter, J. M., Estimating 3-D respiratory motion from orbiting views by tomographic image registration. *IEEE Transactions on Medical Imaging*, volume 26(2), pages 153–163, 2007. Cited on page 8.

Zhao, H. and Reader, A. J., A fast ray-tracing technique to calculate line integral paths in voxel arrays. in *IEEE Nuclear Science Symposium Conference Record*, volume 4, pages 2808–2812, 2003. Cited on page 28.

Zhu, L., Starman, J., and Fahrig, R., An efficient method for reducing the axial intensity drop in circular cone-beam CT. in *International Meeting on Fully Three-Dimensional Image Reconstruction in Radiology and Nuclear Medicine*, pages 264–268, 2007. Cited on pages 21 and 80.

Zhu, S. and Ma, K. K., A new diamond search algorithm for fast block-matching motion estimation. *IEEE Transactions on Image Processing*, volume 9(2), pages 287–290, 2000. Cited on page 97.

Ziegler, A., Köhler, T., Nielsen, T., and Proksa, R., Efficient projection and backprojection scheme for spherically symmetric basis functions in divergent beam geometry. *Medical Physics*, volume 33(12), pages 4653–4663, 2006. Cited on page 28.

Vita

Colas Schretter graduated with *Great Honours* in computer science from the Université Libre de Bruxelles (ULB), Belgium, in 2003. He joined the Unit of Evolutionary Genetics (UEG) at the Institute of Molecular Biology and Medicine (IBMM) of the ULB to develop heuristic algorithms and bioinformatics tools. Afterward, he got several part-time teaching assistant positions for various introductory programming courses taught at ULB and obtained in 2006 a Master of advanced studies (DEA) in sciences from the same university.

Currently, he is attached to the X-ray Imaging Systems (XIS) group of Philips Research Europe in Aachen, Germany while working on image reconstruction and general motion estimation for computed tomography (CT). This position is funded by the Marie Curie Early Stage Training (EST) program of the European Commission under contract MEST-CT-2005-020424. The present thesis has been submitted for obtaining his Ph.D. degree from the Otto-von-Guericke University, Magdeburg, Germany.

His main research interests include theoretical aspects of computer science, geometric algorithms and data structures, image processing, real-time computer graphics and computer vision, physically-based modeling and Monte-Carlo simulations, density estimation problems and expectation-maximization methods, image reconstruction in emission and transmission tomography.